2017

Analysis of critically refracted longitudinal and Lamb waves for stress characterization

Ning Pei
Iowa State University

Analysis of critically refracted longitudinal and Lamb waves for stress characterization

by

Ning Pei

A dissertation submitted to the graduate faculty
in partial fulfillment of the requirements for the degree of
DOCTOR OF PHILOSOPHY

Major: Engineering Mechanics

Program of Study Committee:
Leonard J.Bond, Major Professor
Ronald Roberts
Paul Schafbuch
Timothy Bigelow
Stephen Holland

Iowa State University
Ames, Iowa
2017

DEDICATION

I would like to dedicate this thesis to my parents who always support me.

TABLE OF CONTENTS

LIST OF TABLES

LIST OF FIGURES

ACKNOWLEDGEMENTS

I would like to take this opportunity to say thank you to those who have helped me and supported me in finishing my thesis. My major professor, Leonard J. Bond, is the first name that comes to my mind. He always said to us during our group meeting: ”if you want to be an expert in a research field, at least ten thousand hours are needed.” Every other week’s meeting with him assured me that my research was going in the right direction. I received many of his emails before seven o’clock in the morning and on the weekend. He gave me at least five revisions for my first peer reviewed paper. ”Writing is always painful, but you can get it,” he encouraged me when I was writing this thesis. He deserves the highest praise with dramatic language but instead I choose to record the small moments that can benefit me all my life. I also want to thank Jan Bond, for her kindness. I’ve been to their home for parties many times. Jan is so nice that I have an ”at-home” feeling even though my home is on the other side of the earth.

Other members on my committee all offered a lot of help to push my thesis forward. Prof. Roberts is a theoretical expert and he gave me a lot guidance for numerical calculation. Don Barnard is an research expert in CNDE and people always say the experiment technique is in his genes. I want to thank him for the experimental design. I also want to thank Dr. Chakrapani for many meaningful discussions about my project.

I also want to mention T. Eason, B. Engle, P. Bilgunde, M. Baquera and all the members in my group, they helped me a lot during our four years working together. They are all life-long time friends. I want to say thank you to all the staff and faculty at CNDE and in the aerospace department.

My family always supported me, my mom and dad. They always guided me in the right direction and gave me support from all the possible aspects. I just want to say thank you, mom and dad, and I love you all the time. As a teacher, my uncle, Shuheng, gave me a lot help from primary school on, which has and will benefit me my whole life. I also want to say thank you to my cousins, Guijun, Dong et al., thanks guys for accompanying me as I finished my thesis.

Finally, I want to thank China Scholarship Council (CSC) for their financial support.

ABSTRACT

The global production of metal, in particular, steel and aluminum keeps increasing. This material is used with various fabrication processes, such as, welding, forging, and rolling that can induce stresses in the material that can subsequently impact product performance and cause phenomena such as cracking and corrosion. When investigating plate materials it is necessary to map both texture and stress under a range of loading conditions. To address these needs a wide range of both destructive and nondestructive tools have been used. One family of methods are those based on ultrasonic measurements that relate ultrasonic velocity to properties, in particular stress. Two particular challenges are faced which are the relative insensitivity of compression and shear waves to stress and that there are also other factors which can also change velocity and these are temperature, texture and grain size.

This project focused on an analysis of ultrasonic velocity measurements and specifically ways to improve performance and capabilities for stress characterization. Two approaches were considered and are reported: the critically refracted ultrasonic longitudinal (LCR) wave and higher order Lamb waves.

The LCR wave method was modelled and optimized based on the fact that the sensitivity between waves and stress can reach maximum when they propagate in the same direction. However, in reality this wave typically propagates at an angle to stress, which will decrease its sensitivity. This thesis reports a numerical model used to investigate the transducers parameters that can influence the directivity of the LCR wave and hence enable performance optimization when used for industrial applications. An orthogonal test method is used to study the transducer parameters which influence the LCR wave beams and this method provides a design tool that can be used to study and optimize multiple parameter experiments and identify which parameter or parameters are of most significance. The example considered simulation of the acoustic field in a 2-D water-steel model is obtained using a Spatial Fourier Analysis method. The significance of the effects of incident angle, the aperture and the center frequency of the transducer were studied. Results show that the aperture, the center frequency and the incident angle are the most important factors in controlling the directivity of the resulting LCR wave fields.

The second method considered Lamb wave propagation in the direction perpendicular and parallel to an applied stress. Sensitivity, in terms of changes in velocity, for both symmetrical and anti-symmetrical modes was determined. An available model due to Gandhi, was extended to higher order Lamb modes which were discovered to be more sensitive to stress than either bulk waves or fundamental Lamb modes. The study considered the case of an aluminum plate both analytically and experimentally. Dispersion characteristics were investigated. The experimental system used a pair of compression wave transducers on variable angle wedges, with set separation, and variable frequency tone burst excitation, on an aluminum plate 1.6 mm thick with uniaxial applied loads. The loads used were up to 600 $\mu\varepsilon$, which were measured using strain gauges. The measurement was taken in various locations on the plates to investigate the effects of small changes in plate thickness, the grain size and texture. Model and experimental data are in good agreement. It was discovered that the change in Lamb wave velocity, due to the acoustoelastic effect, for the S_1 mode exhibits about 10 times more sensitive, in terms of velocity change, than the traditional bulk wave measurements, and those performed using the fundamental Lamb modes. The data presented demonstrate that there is potential for the use of higher order Lamb modes for on-line characterization of stress in plate materials and that these methods offer potential for higher sensitivity than that reported previously.

CHAPTER 1. INTRODUCTION

Metal in the form of plates is used in a diverse range of structures and components (Altan and Tekkaya, 2012). Such material can be formed by a diverse range of forming processes including rolling, and when formed it is necessary to ensure that the material meets appropriate specifications. Such specifications can include chemical (elemental) composition, grain size, texture/anisotropy, thickness, uniformity, and strength. In many cases there is also a need to provide characterization of both residual stress, induced during forming and subsequent loading, including in-service behavior.

Global production of steel has continued to increase; in 2015 it had already reach 1620.9 million tons according to WorldSteel Association (2016). Also, the annual global production of aluminum reaches 58.89 million tons, according to the website of the International Aluminum Institute. In many cases the basic metal used in systems is in the form of plates, and the applications for plate material can be as diverse as ship-building and aircraft skin.

There therefore remains a need for improved on-line real time measurements of stress in thin metal plates. There are many available methods for stress (both applied loads and residual stress) characterization, and they can be generally classified as destructive methods (like hole drilling (Schajer, 1988) and layer removal (Greving et al., 1994), and non-destructive methods (like X-ray Diffraction (Welzel et al., 2005) and ultrasonic (Lee et al., 1997)), with each method offering both advantages and disadvantages. From all these methods an ultrasonic method, based on the acoustoelastic effect (Pao and Gamer, 1985) and using the relationships between elastic properties and velocity, will be highlighted here (Kandil et al., 2001). Ultrasonic methods have been proven to represent an effective modality; they are nondestructive, in principle easy to perform, and relatively inexpensive. They also can be used in a non-contact method with potential for in-process implementation during either forming or processing. However, there are also obvious disadvantages associated with such methods. On the one hand, ultrasound velocity is not very sensitive to stress, while on the other hand, other factors like texture (Hirao

et al., 1987), material grain size (Palanichamy et al., 1995) and temperature (Salama and Ling, 1980) can all influence ultrasound velocity, so precision timing is required for wave propagation measurement.

1.1 Problem description

The main problem associated with the traditional ultrasonic method is that the acoustoelastic effect relationship (Pao and Gamer, 1985) is weak between stress and ultrasound velocity (or Time of Flight (TOF)). Fig. 1.1 shows the relationship between ultrasound velocity and stress (strain) for the elastic media (Egle and Bray (1976)). Also, as mentioned above, texture and temperature all have about the same level of influence as stress. For a sample with residual stress, the travel time is related to combined effects of residual stress, texture, temperature and applied loads, and can be written as (Bray and Stanley, 1996):

$$t = t^* + \Delta t_F + \Delta t_{RS} + \Delta t_{TX} + \Delta t_T \tag{1.1}$$

Where

t = measured travel-time;

t^* = travel-time for homogeneous, isotropic, stress-free steel at a standard temperature;

Δt_F = travel-time effect from the applied (active) force;

Δt_{RS}= travel-time effect from the residual stress;

Δt_{TX}= travel-time effect from the material texture (uniform and polycrystalline material);

Δt_T= travel-time effect from the temperature difference from a standard temperature at the time of measurement;

As shown in Eq. 1.1, the measured TOF reflects the contribution of stress (applied stress and residual stress), texture, and temperature, so the influence of texture and temperature must be considered when using an ultrasonic method for stress characterization.

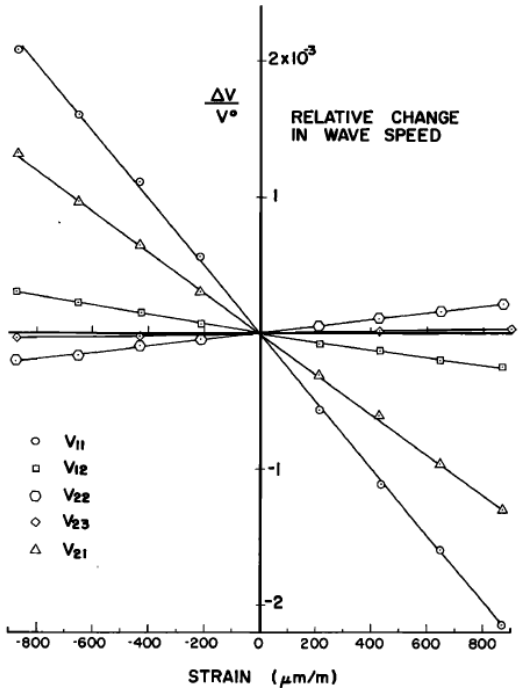

Figure 1.1: Relative change of velocity with strain for bulk waves (Reprinted with Permission from Egle, D and Bray, D. J. Acoust.Sco. Am. 60(3):741-744.)

The problem can be solved in several ways. One would be to separate the influence of various factors (texture and temperature), and there are presently many experts focusing on this approach. Musgrave (1954) demonstrated the propagation of the three major velocity modes (longitudinal wave: L wave; shear vertical wave: SV wave, and shear horizontal wave: SH wave) in transversely isotropic materials. The treatment of these three major modes in combination for an arbitrary texture was described by Etter et al. (2003). Egle (1980) tried to combine velocities sensitive to stress while insensitive to material texture to separate the influence of stress and texture on velocity. While they defined a line for representing zero stress based on an isotropic model, their method could not be used for all kinds of textured material and could measure only the change in stress, not its absolute value. Further more, the combination velocity method seems difficult to apply to highly textural complexity (Musgrave 1970).

Temperature can cause a significant change to TOF, and as previously discussed by many experts. Egle and Bray (1976) showed how wave speed changes with steel and PMMA, i.e., it follows a linear relationship. Fraga et al. (2008) discussed temperature effects on stresses in API 5L steel bars with ultrasonic LCR waves. Their results showed that there is a linear relationship between stress and tem-

perature; as the temperature changed by 1^oC, the TOF of ultrasound velocity would change by $18ns$, about the same level of influence on TOF as stress. (It has already been pointed out (Allen et al., 1982) that the TOF resolution should usually reach $1ns$ for adequate stress characterization with ultrasonic methods). As a way is to deal with the linear relationship between stress and temperature, temperature compensation (Song et al., 2013) can be used to eliminate the influence of temperature.

Even though the relationship between ultrasound velocity and stress, the acoustoelastic effect, is weak, its measurement should be accurate enough to obtain the required resolution for stress (Allen et al., 1982). There are many methods (Breazeale et al., 1981) for accurate measurement of TOF for velocity and two commonly used methods will be highlighted. The first, the sing-around technique (Crecraft, 1968) is based on the principle that measuring TOF for many consecutive cycles and obtaining the a single TOF value by dividing by the number of cycles. The other method, the pulse overlap technique (Hsu, 1974), use the difference between two overlapped signals to determine TOF.

1.2 Overview of the research

This study focuses on enhancing the sensitivity between ultrasound velocity and stress. If the sensitivity is high enough, the influence of other parameters (like texture and grain size) can be diminished and more accurate results for loads/stress can be obtained. The study is mainly focused on two topics: the LCR wave method, and higher order Lamb wave method. Egle and Bray (1976) discussed the change in velocity for different bulk waves as a function of stress (strain), showing that a longitudinal wave in the same direction as the stress (strain) exhibits the maximum sensitivity (Fig. 1.1). Based on this principle, the LCR wave is widely used for stress characterization (Leon-Salamanca and Bray, 1996; Bray and Junghans, 1995). The the direction of the LCR wave should theoretically propagate parallel with the interface of the two media, but in reality it propagates at an angle to the interface. If the velocity and the stress were in the same direction the acoustoelastic effect can reach a maximum as mentioned above. The real problem is therefore how to make the LCR wave and other possible loads align in the same direction. A model was established to simulate generation of LCR waves and model results compared and found to agree with those in the literature (Chaki et al., 2013). Factors that could possibly contribute to the directionality of LCR wave were investigated. The importance of different

parameters was obtained to provide guidance in determining the LCR wave directivity and improve the LCR wave's sensitivity.

Based on the acoustoelastic Lamb wave modal reported by Gandhi et al. (2012), a new MATLAB code was developed and used to investigate the sensitivity of higher Lamb modes to stress. It was found that higher Lamb modes are much more sensitive to stress than traditional bulk waves, and it turns out that the S_1 mode Lamb wave group velocity is the most sensitive to stress in the near cut-off frequency area, about 10 times more than traditional bulk waves when the direction of stress and the direction of velocity are perpendicular, and about 6 times greater than traditional bulk waves when the stress and velocity are in the same direction.

1.3 The contributions to knowledge

The specific contributions made by this thesis are:

1. Established a numerical model for the LCR wave directivity study. The model used a 2D Fourier transformation to describe a wave incident from water near the first critical angle to generate the LCR waves.

2. Applied the Orthogonal Experiment Method to study parameters including the incident angle, the center frequency and aperture of the transducer, and the location of the receiving transducer, that can contribute to the directivity of the LCR wave.

3. Extended the existing model to higher order modes dispersion curve with uniaxial loading (parallel and perpendicular between stress and velocity).

4. Developed of an experimental method for stimulating higher order Lamb wave modes near the cut-off frequency using tone burst generation system.

5. Identified a new method for possible stress detection in the plate-like sample, achieving about 10 times greater sensitivity than for traditional bulk waves.

1.4 Organization of the thesis

This research focuses on enhancing the sensitivity between stress and ultrasound velocity for both the LCR waves and higher-order Lamb waves.

The contents of the thesis can be summarized as:

Chapter 2 presents the background of the topic: loads and stress, residual stress, different methods for stress detection, and a comparison of these methods. Ultrasonic methods are highlighted, and different ultrasonic methods for stress characterization are identified. Finally, possible factors that can influence measurement results are discussed. In Chapter 3, the LCR waves are discussed, including model development, and the Orthogonal Experiment Method is applied for parameter analysis. The theory for Lamb wave propagation in stressed plate is discussed in Chapter 4. In Chapter 5, numerical results are given for Lamb waves corresponding to stressed plates with different load cases, including both perpendicular and parallel configurations. Chapter 6 describes the experimental system and experimental results for Lamb waves for load and measured axis both perpendicular and parallel. In Chapter 7, numerical and experimental results shown in Chapter 5 and 6 respectively, are compared. Results are discussed in chapter 8, and conclusions and possible further work are summarized in Chapter 9.

CHAPTER 2. BACKGROUND AND LITERATURE REVIEW FOR STRESS CHARACTERIZATION

Stress characterization is one of the main motivation of the thesis and this chapter introduces some stress concepts, including the stress-strain relationship, residual stress, comparison of different methods for stress measurement, and a literature review of the ultrasonic method used for stress characterization.

2.1 Loads and stress

The stress-strain relationship for steel (Roylance, 2001) is shown in Fig. 2.1: Point A is called limit of proportionality; for the curve from point 0 to point A the strain is proportional to the load, after which the stress will no longer change linearly with strain. For a short range beyond reaching the proportionality point A, a material can still elastic, meaning that the deformation can be recovered after the load is removed; this range is that between point A and point B, and point B is called the elastic limit; after elastic limit point B is reached, plastic deformation begin to occur, meaning that the deformation can not be recovered by removing loads. Points C and D are called upper and lower yield points, respectively, where continued increase in load will cause further deformation. The point where the stress reaches its maximum (point E) is called the ultimate strength (or yield strength), and the steel begins to break at point F, called the break point. Deformation can be recovered below the elastic range (from point O to point B in the curve), but in plastic range (from point C to point F in the curve) deformation can not be recovered by removing loads and there some strain remains. The dotted line in Fig. 2.1 shows loads with remaining strain $\varepsilon_{residual}$.

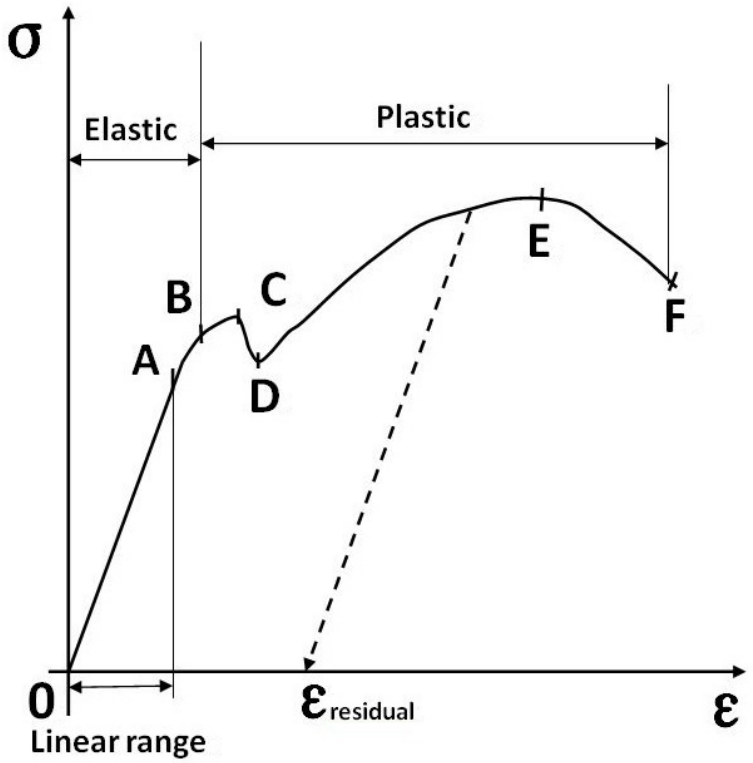

Figure 2.1: Stress and strain relationship for steel.

2.2 Residual stress

Left strains refer to residual stress (Dowell et al., 1977; Egle and Bray, 1976; Kandil et al., 2001; Schajer, 2013), which exist in an elastic solid body in the absence of, or in addition to, the stresses caused by an external load. For residual stresses which are self-equilibrating, the resultant force (sum of compressive and tensile forces) they produce should be zero. Fig. 2.2 shows an example of how residual stress forms and maintained without an external force: a plate originally in a non-stressed state with force added to the left and right edges, if the force is large enough (causing plastic deformation) there is some remaining stress, called residual stress, when the external force has been removed.

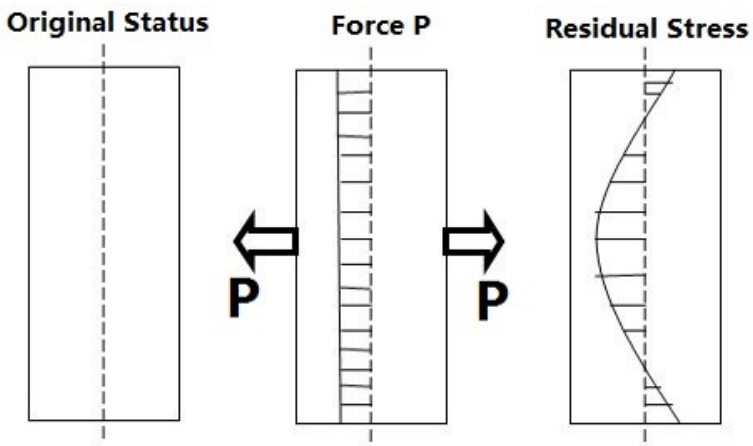

Figure 2.2: Diagram shows how residual stress forms and it is maintained.

Residual stress can be generated by many mechanical process, including the working environment, like temperature difference and applied local force, can contribute to the formation of such stresses. The origin of residual stress can be classified as due to mechanical, thermal or chemical phenomena (Treuting and Read Jr, 1951; Robinson et al., 2009). With response to mechanically-induced forces, non-uniform plastic deformation is one main factor causing residual stress that can be introduced during processes such as turning, milling or rolling. In the case of thermally-induced forces, non-uniform heating and cooling are the usual causes of residual stress. Chemically-induced residual stress usually originates from non-uniform or surface chemical reactions. Fig. 2.3 depicts these possible causes of residual stress.

Residual stresses are often ignored because are self-equilibrating. During manufacturing and engineering design, even though people seldom consider whether residual stresses are or not generated, such stresses should be given much more attention because they are obviously influence component performance. Residual stresses can be either beneficial or harmful depending on their direction and location. To illustrate the beneficial case, a typical applications might introduce compressive residual stress to brittle materials to prevent the formation of fractures, which is the main cause for brittle material failure. A compressive residual stress can prevent the growth of crack because if the cracks are inclined to grow they must first overcome the residual stress, so the growth rate may at least be slowed. There are many methods to generate compressive residual stresses, like shot peening, Laser shock processing

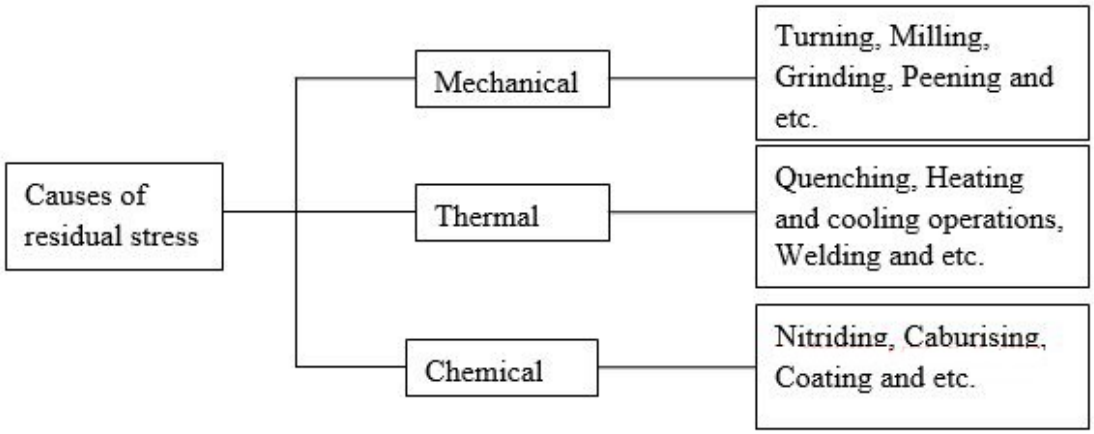

Figure 2.3: Diagram showing different causes of residual stress.

(LSP) and Low Plasticity burnishing (LPB) (Prevéy and Cammett 2001). Residual stresses of course also can have harmful aspects such as shortening component life of decreasing component reliability. The usual residual stresses are tension stresses that can promote the growth of cracks, and there are many examples in industry that show that large component fractures can be caused by residual stress. Because of non-uniform stresses in wheels, railroads can also generate residual stresses, and there have been many railroad accidents reported (Anderson and Barkan 2004) that are caused by residual stresses. Much health monitoring is focused on defect evaluation, and in fact many defects are caused by residual stresses, as is shown in Fig. 2.4. So it is quite desirable to first discover the presence of residual stresses and then remove the bad ones.

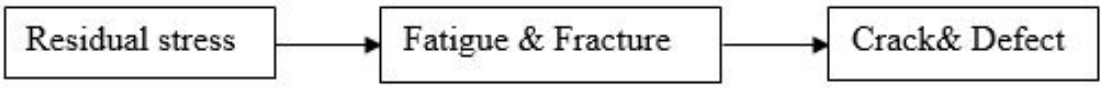

Figure 2.4: Schematic diagram showing residual stresses causing crack and defect.

2.3 Different destructive, semi-destructive and non-destructive methods for stress characterization

As stated above, stresses can be unconsciously created and they can be either beneficial and harmful, so it is important to remove harmful stresses in a component while retaining beneficial stresses. There are many methods for detecting stress and they can be classified (Kandil et al., 2001) as follows:

2.3.1 Mechanical methods

One category is Mechanical Stress Measurement Methods (Shadley et al., 1987; Treuting and Read Jr, 1951; Bulckaen and Gucci, 1975; Keil, 1992), based on the relationship between strain and stress. By measuring the change of strain (deformation), the relevant stress can be obtained through knowledge of the stress-strain relationship. Mechanical Methods include the splitting method, the sectioning method, and the layer removal method, the hole-drilling method, the ring-core method and others. Fig. 2.5 depicts hole-drilling method and the splitting method.

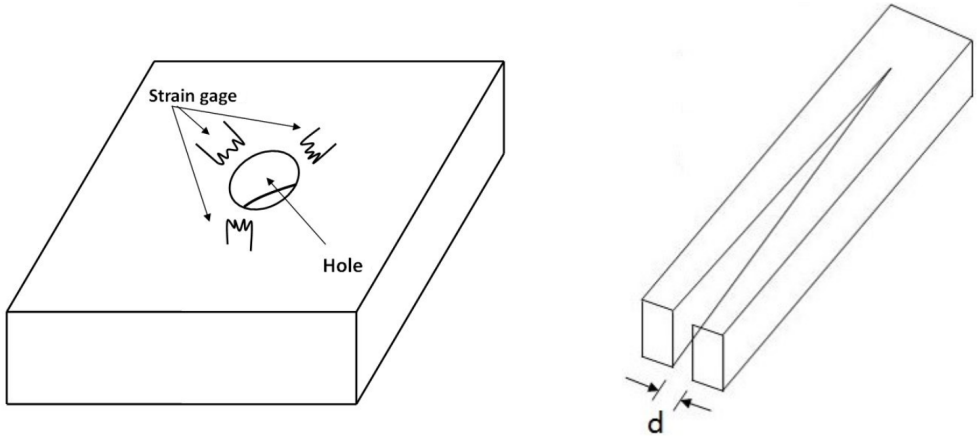

Figure 2.5: The schematic diagram showing hole-drilling method and splitting method.

2.3.2 Radiation based diffraction methods

Diffraction Methods (Ma et al., 2002; Reimers et al., 1999) include X-ray Diffraction method, the Synchrotron X-ray method, the Neutron Diffraction method and others. X-ray Diffraction method is based on Braggs Law:

$$n\lambda = 2d\sin\theta \tag{2.1}$$

Where n can be any positive integer (determined by the order given), λ is the wavelength of the electromagnetic radiation, d is the distance between the diffracting planes, and θ is the Bragg angle. Fig. 2.6 shows the parameters in detail. Strain can be obtained by:

$$\varepsilon = \frac{\Delta d}{d} = -\cot\theta\Delta\theta \tag{2.2}$$

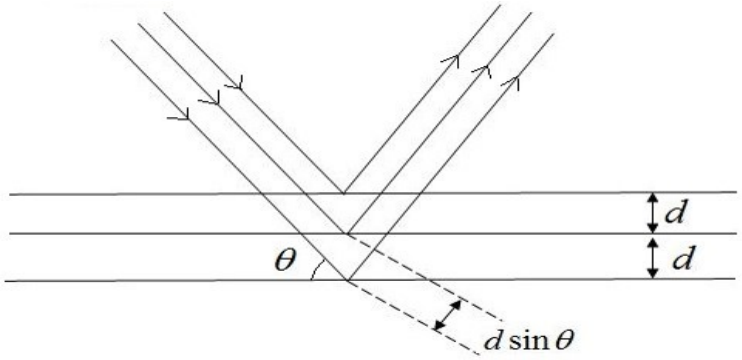

Figure 2.6: Schematic diagram showing an example for radiation diffraction.

2.3.3 Magnetic methods

Magnetic Barkhausen Noise (MBN) detection is a popular magnetic method (Gauthier et al., 1998; Yelbay et al., 2010) for stress detection. The basic theory of using MBN method for stress detection is based on the fact that stresses can influence Barkhausen Noise signals. The phenomenon through which stresses interact with magnetic properties of material is called Magnetoelastic interaction, and it explains how stresses influence Barkhausen Noise signals. Based on a change in MBN, corresponding stresses can be evaluated. Compressive residual stresses will usually decrease MBN while tensile residual stresses will usually increase MBN. The biggest limitation for this method is that it can be applied only to ferromagnetic materials.

2.3.4 Thermoelastic method

Thermoelastic (Robinson et al., 2009) stress analysis (TSA) is a non-destructive and portable method that can be used for stress characterization. This method relies on the relationship between temperature and stresses; temperature will exhibit a small change called the thermoelastic effect when there is a change on stress, and the relationship between temperature and stress can be written as:

$$\Delta T = -KT_0\Delta\sigma_{kk} \tag{2.3}$$

Where T_0 is the absolute temperature, ΔT expresses the change in temperature, $\Delta\sigma_{kk}$ is the change in stress, $K = \alpha/(\rho C_p)$ is the thermoelastic constant, and $\alpha, \rho,\ C_p$ are material constants.

While this linear equation is based on the assumption that the material properties are independent of temperature, in reality the material properties are influenced by temperature, so a nonlinear equation was obtained that considers this influence:

$$\dot{T} = \frac{T_0}{\rho C_p}[-(\alpha + (\frac{\nu}{E^2}\frac{\partial E}{\partial T} - \frac{1}{E}\frac{\partial \nu}{\partial T})\sigma_{kk})\dot{\sigma_{kk}} + (\frac{(1+\nu)}{E^2}\frac{\partial E}{\partial T} - \frac{1}{E}\frac{\partial \nu}{\partial T})\sigma_{ij}\dot{\sigma_{ij}}] \tag{2.4}$$

Where $\dot{T}$ is the rate of change of temperature, E and ν are Youngs modulus and Possions ration, respectively;

2.3.5 Roman/Fluorescence method

The Raman/Fluorescence effect (Hung, 1982) is related to the interaction between light and materials. Information about a material, including possible stresses, can be obtained by analysis of the scattered beam from the material. Fluorescence lines have a liner relationship with stresses, and as a non-destructive method for stress detection, the Raman/Fluorescence method has high spatial resolution compared to other methods. The disadvantage of this method is also obvious, i.e., the method can only be applied at the material surface.

2.3.6 Ultrasonic methods

The Ultrasonic Method (Bray, 2002) is based on the acoustoelastic effect, i.e., the velocity of ultrasound will change with a change in stress. The biggest challenges for this method is that the velocity of

ultrasound is not very sensitivity to stress, and the velocity can also be affected by many other factors such as grain size and texture. All these extraneous factors that can influence the measurement results for these factors have about the same level of influence as stress itself. The measurement's accuracy should also be considered. (This method will be described in more detail later)

2.3.7 Comparison of different stress measurement methods

The following three tables (Table 2.1, Table 2.2, Table 2.3) (Kandil et al., 2001) compare different methods of stress measurement from the different perspectives of material applicability, physical characteristics, and application analysis. Table 2.1 indicates the kind of materials the methods can be applied for and the requirements for measurement. Table 2.2 describes different physical characteristics for different methods. Table 2.3 is concerned with application analysis, including cost, messurement speed, and other factors. In choosing an application or selecting a method, the various choices should be compared and their relative advantages and disadvantages should be considered.

2.4 Ultrasonic methods for stress characterization

As described in the last section, there are many methods for stress characterization, each with advantages and disadvantages. In this section methods based on acoustoelastic effects, including the relationships between the material elastic properties and ultrasound velocity are highlighted. Ultrasonic methods have proven to be an effective modality: they are nondestructive, in principal easy to perform, and relatively inexpensive. They do however require precise timing of wave propagation with stress calculation based on averaged values over the measurement zone.

2.4.1 Literature review for ultrasonic methods

The theory for ultrasonic methods for stress characterization originated from Murnaghan's theory (Murnaghan, 1937) of nonlinear elasticity, which describes the finite deformation of an elastic solid. Based on Murnaghan's theory, Hughes and Kelly (1953) developed the theory of acoustoelasticity, that describes the relationship between the change in ultrasonic velocity and a change in material strain.

Table 2.1: Comparison based on material applicability [after Kandil et al., (2001)]

	Material Applicability				
Different Techniques	**Material Type**	**Composites**	**Contacted ?**	**Surface Preparation**	**Surface Condition**
Hole Drilling	Matals Plastics Ceramics	Yes	Yes	Light Abrasionstrain Gauge	Flat-Preparation must not affect stresses
X-ray Diffraction	Matals Ceramics	Yes	No	Important	Important
Synchrotron	Matals Ceramics	Yes	No	Important	Not Critical
Neutron Diffraction	Matals Ceramics	Yes	No	Not Critical	Not Critical
Curvature and Layer Removal	All	Yes	Yes	Not Critical	Not Critical
Magnetic	Ferromagnetic Materials	No	No	Not Critical	Not Critical
Ultrasonic	Matals Ceramics	Yes	No	Not Critical	Not Critical
Fluorescence	Ceramics Polymers	Yes	No	Not Critical	Not Critical

Since then experts have further developed the theory and resulting methods for stress (including residual stress and applied stress) characterization with ultrasonic methods.

In the early years, Benson and Raelson (1959) discovered the birefringent phenomenon of stress using polarized shear waves. When a wave is incident at a certain angle, it will separate into two parts: one part polarized parallel to the direction of the stress and the other polarized vertical to the direction of the stress. These two parts spread at different velocities, leading to a birefringent phenomenon through which stress can be analyzed.

Thurston and Brugger (1964) discussed third order elastic constants that can be used to describe the stress dependence of ultrasonic velocities. Crecraft (1967) showed results for the measurement of velocity change with a change in applied stress, for steel, aluminum, and copper and calculated third-order elastic constants. That article also discussed how to separate the influence of stress and grain

Table 2.2: Comparison of different stress measurement methods [after Kandil et al., (2001)]

	Characteristics							
Different Techniques	**Measurement depth**	**Penetration**	**Stress Type**	**Stress State**	**State Gradient**	**Resolution**	**Sampling Volume**	**Remarks**
Hole Drilling	50-100 μm Depth	Hole Diameter	Macro	Uniaxial Biaxial	Yes	Varies With Depth	1-2mm diam/deep	N/A
X-ray Diffraction	20 μm Depth	50 μm-Ti;50 μm-Al	Macro; Micro	Uniaxial Biaxial	Yes	Limited by grain Sampling	$0.1 - 1mm^2$	Resolution for steel 1 mm diameter 15 μm depth
Synchrotron	20 μm Depth	500 μm 100 μm-Al	Macro; Micro	Uniaxial Biaxial Triaxial	Yes	Limited by grain Sampling	$0.1mm^3$	Measures strain only; Rarely possible to obtain stresses
Neutron Diffraction	500 μm	100 μm-Al 25 mm-Fe 4 mm-Ti	Macro Micro	Uniaxial Biaxial Triaxial	Yes	Limited by number of counts	$1mm^3$	N/A
Curvature and Layer Removal	Depends	Not Applicable	Macro	Uniaxial Biaxial	Yes	N/A	N/A	Layer Removal can be combined with other measurement such as XRD
Magnetic	1mm	20-300 μm	Macro	Uniaxial Biaxial	No	N/A	$2mm^3$	Sensitive to microstructure, anisotropy and texture
Ultrasonic	5mm	100 μm along specimen	Macro	Uniaxial Biaxial	No	Measurement process	$1 - 400mm^2$	Should considering other factors that can influence the results
Fluorescence	0.5 μm	Surface	No	Uniaxial Biaxial	N/A	N/A	N/A	N/A

Table 2.3: Comparison based on application analysis [after Kandil et al., (2001)]

Different Techniques	Characteristics								
	Contact or Non-contact	**Destructive or not**	**Lab based or portable**	**Availability of equipment**	**Speed of measure-ment**	**Standards availability**	**Cost of equipment**	**Cost of measure-ment**	**Level of expertise required**
Hole Drilling	Contact	Semi	Both	Widespread	Fast/Medium	ASTM E837-99	low	Low	Low/Medium
X-ray Diffraction	Non-contact	No	Both	Generally avail-able	Fast/Medium	No	Medium	Low	Medium
Synchrotron	Non-contact	No	Lab	Specialist	Fast	No	Strategic	High	High
Neutron Diffraction	Non-contact	No	Lab	Specialist	Medium/Slow	No	Strategic	High	High
Curvature and Layer Removal	Contact	Yes	Lab	Generally avail-able	Medium	No	Low	Low	Low/Medium
Magnetic	Non-contact	No	No	Generally avail-able	Rapid	No	Medium	Low	Low
Ultrasonic	Contact	No	No	Generally avail-able	Rapid	GB/T 32073-2015	Medium	Low	Medium
Fluorescence	Non-contact	No	No	Generally avail-able	Fast	No	Medium	Low	Medium

alignment during measurements by ultrasonic methods. Noronha et al. (1973) proposed a technique that utilizes ultrasonic radiation to measure residual stress, developing a method for measuring both the amplitude and direction of the stress. Their system was called the Modified Time of Flight System.

Wert and Noronha (1975) used a pulse-echo system to measure residual stress based on the travel time of the ultrasonic shear wave. They compared the results obtained using this ultrasonic method with that obtained using strain gauges, and confirmed that ultrasonic methods are a reliable way to measure stress. With a background for measuring residual stress in railroad rails, Egle and Bray (1976) showed that all of the five possible relative changes in wave speeds with the uniaxial stress could be measured, validating the theory developed by Hughes and Kelly. They calculated third-order elastic constants based on experimental data and also found that velocity changes most when the velocity and the stress are in the same direction. Bray et al. (1978) developed an ultrasonic transducer for measuring longitudinal stress changes in rails based on the acoustoelastic phenomenon and reported both laboratory and field measurements. Their results show that the ultrasonic methods are capable of accurate stress measurement.

Kino et al. (1980) measured two-dimensional velocities observing changes caused by both externally applied stress and residual inhomogeneous stress. The change of microstructure of the samples can lead to similar results. The ultrasonic method was further developed shown capable of use for simultaneously measuring stress fields and microstructure. Chern and Heyman (1982) used a new ultrasonic method, called a Reflection Oscillator Ultrasonic Spectrometer (ROUS), to measure stress in fasteners. They discussed the influence of fastener length change under load on stress measurements and also showed that different bolt geometries, like poor geometry bolts and bolts with holes, resulted in different influences on the measurement results.

During the 1990's and the early 2000's, research in this area mainly focused on applying ultrasonic methods for different applications. Wormley et al. (1990) developed an ultrasonic method for measuring texture, stress, and other physical properties for metal sheets. They used guided waves generated by EMAT transducers for the measurement, with the aim of simultaneously considering texture, stress and other physical properties and trying to find application to in predicting sheet metal formability. Deputat et al. (1992) applied ultrasonic methods for residual stress detection in railroad components, including cylindrical forgings, rails, and solid wheels. They used surface skimming longitudinal waves, SV waves,

and SH waves to map the distribution of residual stresses in the near-surface layer of cylindrical forgings and rails.

Hirao et al. (1993) used a miniature shear wave EMAT to map the stress field in thin metallic plates. The method demonstrated high measurement accuracy, high spatial resolution, and tolerance to unprepared surface and could be used in many implementation, especially for small samples. Tanala et al. (1995) measured residual stress caused by welding processes for stainless steel pipe and aluminum alloy plate. Subsurface longitudinal waves and Rayleigh waves were applied during the measurement. Ultrasonic results are confirmed by data obtained using the X-ray diffraction technique. Clark et al. (1995) measured the residual stress in cast-steel wheels. Two different ultrasonic instruments were used to obtain results that could be compared with one another. A destructive method was used to validate the data obtained by ultrasonic methods. Bray and Junghans (1995) used LCR waves to detect the residual stress in the welded area. Two 1.22 m square plates were welded together to generate residual stress. They concluded that this method could characterize both the amplitude and distribution.

During the 2000's, research studies have considered different factors that can influence ultrasonic methods for residual stress characterization. Withers and Bhadeshia (2001) wrote a review paper about measurement techniques for residual stress that mainly discussed different methods for residual stress detection, including the advantages and disadvantages and preferred applications of this methods. They also discussed the nature and origins of the residual stress in detail.

Duquennoy et al. (2002) discussed how to theoretically obtain Rayleigh wave acoustoelastic coefficients, and they compared their results with the experimental data to confirm validity. Their method allows acoustoelastic coefficients to be calculated numerically, rather than obtaining them with experimental method. This method is very important, especially when calibration for experimental measurement is difficult.

Belahcene and Lu (2002) used LCR waves to characterize the possible residual stress in butt-welded specimens. TOF for the LCR wave was measured and calibrated samples were used to obtain the acoustoelastic coefficients. The stresses were successfully reported, and the results were validated with data obtained using the hole-drilling method. Lanza di Scalea et al. (2003) studied the effect of frequency on acoustoelastic responses from steel bars. They found that the acoustoelastic changes sensitively with the change of frequency; for the same steel bar diameters, low frequency values led

to high sensitive acoustoelasticity, while high frequency values led to low sensitive acoustoelasticity. These results can be helpful when choosing a suitable frequency for residual stress detection in steel bars. Murayam and Misumi (2006) discussed the influence of temperature and magnetic field on the elastic constants for Ni-Mn-Al magnetic Heusler alloys, with theoretical analysis and experimental results in good agreement.

In recent years, research has focused on developing ultrasonic methods for stress characterization of new materials. Fraga et al. (2008) discussed the influence of temperature and transducer frequency on the LCR wave for stress measurement on pipelines, with results showing that the temperature influence can as large as 64 MPa/°C, and the frequency of the transducer can also significantly influence the measurement results. Gachi et al. (2009) applied the LCR wave to detect possible residual stress in AA7108 aluminium alloy sheets in the weld area produced by Friction Stir Welding (FSW). The measurement results were proven to be correct by comparing with results obtained from the X-ray method. Karabutov et al. (2008) developed a new transducer for residual stress detection based on the optoacoustic (OA) phenomenon. Their motivation was to enhance the sensitivity between ultrasound velocity and residual stress, considering that the acoustic-elastic relationship is weak between them. To enhance measurement resolution the wide-band ultrasonic pulse would be the best choice, but this can not be achieved using traditional piezoelectric techniques. With a newly-designed transducer, the timing resolution can reach 0.5 ns. Qozam et al. (2010) measured the possible residual stress in the heat affected zone (HAZ) of the welding area of the sample. The hardest task was to obtain a reference sample of the HAZ area, and they reproduced the microstructure for the HAZ zone, with measurement results are in good agreement with the hole drilling method. Palanichamy et al. (2009) compared two welding methods, Tungsten Inert Gas (TIG) and Activated Tungsten Inert Gas (ATIG) welding, using an ultrasonic method for detecting residual stress, with results showing that the ATIG method generates much less residual stress compared to the traditional TIG method. Pei and Demachi (2010) used a finite element method to simulate the acoustoelastic effect in pre-stressed media. They used a traditional PZT transducer and EMAT to generate and receive the LCR waves, with results in good agreement with the theoretical results.

Tsai and Zhu (2012) developed a new method, the modal frequency spacing method, to measure residual stress. The advantage of this method was that water is used as couplant, and the thickness of

this couplant can be well maintained. This method is based on the Modal Frequency Spacing (MFS) that is more sensitive to stress than the traditional method for measuring TOF. They performed experiments to validate the model and also detected residual stress in welded steel plate.

Rossini et al. (2012) did a literature review of residual stress measurement methods in components. One obvious disadvantage of the ultrasonic method is that the change of ultrasonic velocity is insufficiently sensitive to the change of stress. Buenos et al. (2013) measured the residual stress by the ultrasonic method, with an aim of correlating cutting speed, the feed per tooth, and the depth of cut to stress. They performed several measurements and analyzed the data using statistical methods. They also considered the influence of temperature on ultrasound velocities, finding a temperature effect of 11.12 ns/°C.

Javadi et al. (2013) investigated residual stress in austenitic stainless steel plates (AISI 304L) using a 3D thermo-mechanical finite-element model. They obtained a 3D map of residual stress for an entire welded plate by combining the finite-element modal and the LCR wave method. To evaluate the stress in the heat-affected zone, a metallographic method was used to obtain a tensile test sample. Different transducers frequencies were used to measure stress at different depths. They concluded that FELCR (combined finite-element welding simulation and ultrasonic stress measurement by LCR waves) is a reliable method for stress detection.

2.4.2 Currently used ultrasonic methods for stress characterization

Ultrasonic methods for stress characterization are based on the wave field employed, so different types of ultrasonic waves can be used to characterize stress in different locations. Bulk ultrasonic waves can characterize stress inside the samples while surface waves can characterize stress near the surface.

2.4.2.1 Bulk ultrasonic waves for stress characterization

Three typical ways for measuring residual stress using bulk waves are shown in Fig. 2.7. (a) shows through-thickness pulse-echo method that can detect the possible residual stress in the thickness direction. (b) shows the through-thickness pitch-catch method, where the waves are reflected from the bottom of the sample and received by the receiving transducer. This method can measure the possible residual stress deep in the sample. (c) shows wave propagation just below the surface; this type of

wave is known as the LCR wave as discussed previously. This method is widely used in industry for residual stress detection because of the high sensitivity (Bray et al., 1978) between ultrasound velocity and stress.

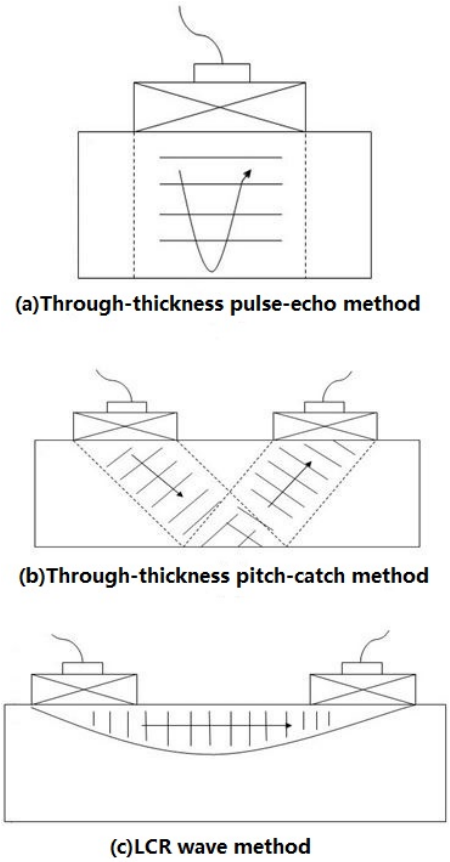

Figure 2.7: Three different ways for stress detection by bulk wave: (a) Through-thickness pulse-echo method; (b) Through-thickness pitch-catch method; (c) the LCR wave method.

Hughes and Kelly (1953) developed the relationship between the elastic wave and the stress, the geometry is shown in Fig. 2.8.

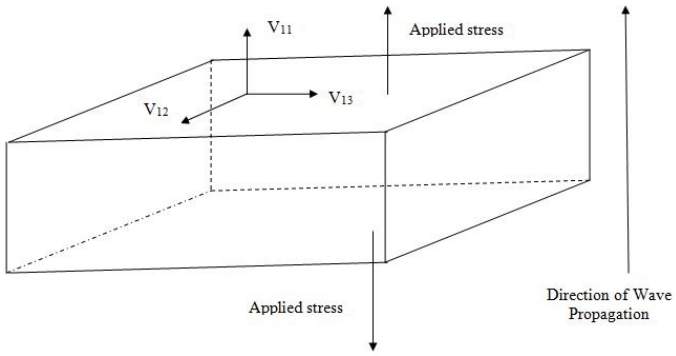

Figure 2.8: Speed of plane waves and stress field on orthogonal coordinate system.

In a stressed sample with three different velocities in different directions, the relationships between the velocity and the strain can be expressed as (Bray and Stanley, 1996):

$$\rho_o v_{11}^2 = \lambda + 2\mu + (2l + \lambda)\theta + (4m + 4\lambda + 10\mu)\alpha_1 \tag{2.5}$$

$$\rho_o v_{12}^2 = \mu + (\mu + \lambda)\theta + 4\mu\alpha_1 + 3\mu\alpha_2 - \frac{1}{2}n\alpha_3 \tag{2.6}$$

$$\rho_o v_{13}^2 = \mu + (\mu + \lambda)\theta + 4\mu\alpha_1 + 3\mu\alpha_3 - \frac{1}{2}n\alpha_2 \tag{2.7}$$

Where $\rho_o =$ initial density;

v_{11}, v_{12}, v_{13} are velocities in different directions;

λ, μ, l, m, n are second and third order elastic constants;

$\alpha_1, \alpha_2, \alpha_3$ are strains in different directions and $\theta = \alpha_1 + \alpha_2 + \alpha_3$

For a state of uniaxial stress, there are five unique wave speeds that can be determined by the equations given above. For example, when the stress acts in the same direction as v_{11}, the strains are expressed as:

$$\alpha_1 = \varepsilon, \alpha_2 = \alpha_3 = -\nu\varepsilon \tag{2.8}$$

Where ν is Poisson's ratio. Considering Eq. 2.8, Eq. 2.5 and Eq. 2.6 reduce to:

$$\rho_o v_{11}^2 = \lambda + 2\mu + [4(\lambda + 2\mu) + 2(\mu + 2m) + \nu\mu(1 + 2l/\lambda)]\varepsilon \tag{2.9}$$

$$\rho_o v_{12}^2 = \rho_o v_{13}^2 = \mu + [4\mu + \nu(n/2) + m(1 - 2\nu)]\varepsilon \tag{2.10}$$

The relative changes in wave speed with axial strain can be calculated from Eq. 2.9 and Eq. 2.10, assuming that relative changes are small. The resulting equations are:

$$\frac{dv_{11}/v_{11}^0}{v_{11}^0} = 2 + \frac{\mu + 2m + \nu\mu(1 + 2l/\lambda)}{\lambda + 2\mu} = L_{11} \tag{2.11}$$

$$\frac{dv_{12}/v_{12}^0}{d\varepsilon} = 2 + \frac{\nu n}{4\mu} + \frac{m}{2(\lambda + \mu)} = L_{12} \tag{2.12}$$

In Eq. 2.11 and Eq. 2.12, L_{11} and L_{12} are the acoustoelastic constants and the superscript 0 indicates the wave speed at zero axial strain. In experiments, the following equation is usually applied for calculation:

$$d\sigma = \frac{E(dv_{11}/v_{11})}{L_{11}} = \frac{E}{L_{11}t_0}dt \tag{2.13}$$

When performing experiments, the following three types of specimens are needed: a, tensile specimens for determining the acoustic-elastic coefficients; b, gauge blocks for determining the wave penetration depth and c, specimens for determining residual stresses.

2.4.2.2 Rayleigh ultrasonic waves for stress characterization

The Rayleigh wave acoustoelastic relationship was firstly developed by Hayes and Rivlin (1961). Their theory was for the case when waves propagate along the principal axes of the stress. Later their theory was extended by Iwashimizu and Kobori (1978) to give an expression for the wave speed for the case when the stress does not propagate along the principle axes. Hirao et al. (1981) discussed the acoustoelastic effect both uniform and non-uniform initial deformations in the depth direction. Their results showed that, with a uniform load, the velocity changes linearly with the principal strain. For the non-uniform case, the Rayleigh wave becomes dispersive and depends on the product of the wave number and the propagating depth. Delsanto and Clark (1987) applied Rayleigh waves to detect both stress and texture in an anisotropic material, with the validity of the results proven by comparison with ultrasonic bulk waves and neutron diffraction data. Duquennoy et al. (2001) detected the possible residual stress in steel sheets by measuring the change of TOF for Rayleigh waves. The residual stress profile was obtained and the results verified by comparing with data from a destructive analysis. They also discussed various factors that could influence the results.

The expression for the relationship between stress and velocity can be written as (Duqennoy et al., 1999):

$$\frac{\Delta v_{R12}}{v^0_{R12}} = \frac{v_{R12} - v^0_{R12}}{v^0_{R12}} = A^{(1)}_{R12} T_1 + A^{(3)}_{R12} T_3 \tag{2.14}$$

$$\frac{\Delta v_{R21}}{v^0_{R21}} = \frac{v_{R21} - v^0_{R21}}{v^0_{R21}} = A^{(2)}_{R21} T_1 + A^{(3)}_{R21} T_3 \tag{2.15}$$

Where v_{R12} is the Rayleigh wave propagating in the X direction and polarized in the Z direction, while v_{R21} is the Rayleigh wave propagating in the Y direction and polarized in the Z direction;

$\boldsymbol{v_0}$ stands for velocity without stress while $\boldsymbol{v}$ stands for velocity with stress. $\boldsymbol{A}$ are the acoustoelastic constants with different superscript and subscript. The schematic is shown in Fig. 2.9.

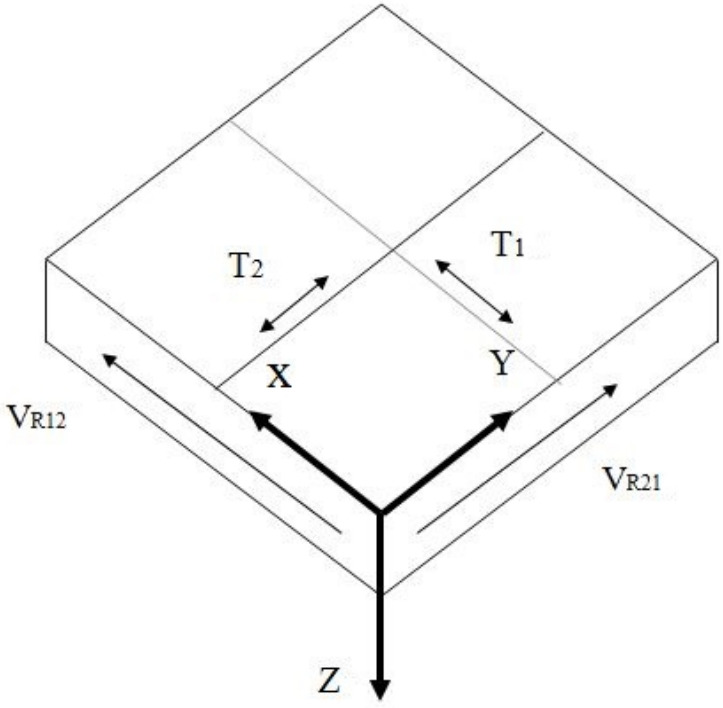

Figure 2.9: Diagram of the Rayleigh wave propagation. [after Duqennoy et al.,(1999)]

2.5 Lamb wave propagation in stressed plates

In a range of metal forming processes, there remains a need for improved on-line real-time measurements of stress in thin metal plates that can not be detected by bulk wave (like the LCR wave) or

surface waves. Guided waves, also known as Lamb waves, have been used to provide one approach to making such measurements nondestructively (Ensminger and Bond 2011). The velocity of these waves is sensitive to the effects of texture, anisotropy, temperature, and stress in the plate material. These phenomena all cause changes in the various higher-order elastic constants that determine wave velocity and these relationships are known as the acoustoelastic effects.

The feasibility of utilizing the acoustoelastic effect, the relationships between elastic properties and velocities, as a mean for investigating texture and stress has long been established (Murnaghan 1937; Hughes and Kelly 1953). An extensive treatment of the fundamental aspects of the topic was provided by Pao et al. (1984). The phenomena have now been applied for measuring both applied and residual stress, and such measurements have been established and reported in many studies (Crecraft, 1967; Kandil et al., 2001; Rossini et al., 2012). There have been a more limited number of studies that have considered methods for measuring residual in-process stress, such as with aluminum plates, and these have included implementations using shear-horizontal (SH) wave EMATs (Clark and Moulder 1985). However, in all these investigations there have been challenges in providing adequate sensitivity, in terms of the accurate time measurement needed for velocity estimation, particularly at lower stress levels where velocity changes are quite small and where these effects can be of an order similar to those related to temperature and texture. An alternative related approach to providing residual stress characterization has been performed using the LCR waves (Bray and Junghans 1995; Belahcene and Lu 2002; Bray and Tang 2001), also known as creeping waves. The LCR wave is usually generated at the first critical angle of the incident wave at the interface, and it then propagates just below the surface of the specimen. These waves are found to be most sensitive to the stress aligned in the direction of wave propagation.

When looking at the case of thin plates it is various Lamb waves rather than LCR waves that are generated using this configuration. Investigations of the use of Lamb modes and the fundamental theory involved that seeks to provide methods for improved stress measurement have remained of interest for many years. For example Husson (1985) extended his perturbation theory for bulk waves to the analysis of surface and Lamb waves. He predicted that Lamb waves would be found only sensitive to symmetric stress fields. Qu and Liu (1998) discussed acoustoelastic phenomena for guided waves by using Strohs method. They compared dispersion curves for a pre-stressed single plate and bonded

layers and concluded that tri-layer medium are very sensitive to residual stress while single layers are less so. However, they offered no experimental results to validate their analysis.

Chen and Wilcox (2007) analyzed the relationship between load and guided wave velocity in plates and in rail-like structures using a finite-element method. They also compared their results with those from an Euler-Bernoulli beam model. Lematre et al. (2006) analysed residual stresses in piezoelectric layers (both single and polylaminate) and used the Christoffel equations and considered the circumstance when the direction of the velocity is consistent with the direction of the load. Shi et al. (2013) developed a method to estimate biaxial loads by measuring the change in phase velocity. This method can be used for in situ stress detection. Gandhi et al. (2012) continued to investigate the theory and extended it from bulk wave acoustoelasticity to Lamb wave acoustoelasticity. They provided both numerical model data and experimental results to show how velocities change with a change in the loading direction. Pau and di Scalea (2015) established an analytical model for analysis of the nonlinear response for guided waves in prestressed plates. An appropriate third-order expression describing the strain energy of the hyperelastic body was added to the model and seen to provide accurate results.

In all the studies discussed, however, there remains however the general challenge that under many circumstances velocity changes induced by stress are relatively small, resulting in the need for implementing precise timing and instrumentation. In looking for increased sensitivity, this study has moved toward considering higher order Lamb modes and their relationship to the effects of applied stress on these waves. Model data and results of experimental measurements in good agreement are given, and the data demonstrate significantly higher sensitivity to stress. The results of the numerical models, where preliminary data had previously been presented (Pei and Bond 2015), showed that some higher order modes exhibit greater sensitivity to stress than in the case of the fundamental Lamb wave modes. A calibrated experimental load frame used in an earlier study to investigate stress and texture was employed in this study to load aluminum plates (Wormley and Thompson 1989) and procedure data to compare with that from the models.

2.6 Chapter summary

This chapter has introduced the concept of stress, its causes and effects, and described different methods for residual stress characterization. Ultrasonic methods are highlighted because of their obvious advantages, while bulk wave, surface waves and Lamb waves are discussed separately to measure possible stresses in different samples.

CHAPTER 3. ANALYSIS OF CRITICALLY REFRACTED LONGITUDINAL WAVES FOR STRESS CHARACTERIZATION

Fabrication processes such as welding, forging, and rolling, can induce stresses in metals that can impact product performance and enhance destructive phenomena such as cracking and corrosion. To better manage stress, tools are needed to map their distribution. The LCR wave is one such approach that has been widely used for stress characterization in recently years. It has been shown to be sensitive to stress and less sensitive to the effects of material texture.

LCR waves are also referred to in some of the literature (Langenberg et al., 1990) as creeping waves. For a fluid-loaded surface the LCR wave is generated at the first critical angle of the incident longitudinal wave, producing waves that propagate below, yet close to the surface of the specimen. It has been found that, for residual stress detection, the LCR wave has some advantages; it is relatively sensitive to the effects of stress, and less sensitive to the structure of materials (Belahcene and Lu, 2002) and the application of LCR waves for stress detection has been considered by several groups (Santos et al., 2008; Bray and Junghans, 1995; Belahcene and Lu, 2002; Bray and Tang, 2001; Lu et al., 2008).

Although the LCR wave has increasingly been widely applied, the factors that can influence the formation of the LCR beam and make a contribution to the sensitivity of the stress measurement are seldom discussed. Theoretical analysis of LCR waves was provided by Basatskaya and Ermolov (1981). They began from the basic wave equations and boundary conditions and established a 2-D model for harmonic waves. The directionality of the LCR wave was calculated and the depth to which it can spread was discussed. The typical acoustical field of the LCR wave was calculated by Langenberg et al. (1990), using a numerical elastodynamic finite integration method. Since then it seems that there has been limited research work on more fundamental aspects of this family of waves.

This chapter describes a numerical model used to investigate the transducer parameters that can contribute to the directionality of the LCR wave and hence enable performance optimization when used

for industrial applications. An orthogonal test method (Cui et al., 2007) has been used to study and optimize multiple parameter experiments and can identity which parameter or parameters are of most significance. The simulation of the acoustics field in a 2-D water-steel model has been obtained using a Spatial Fourier Analysis method. The effects of the incident angle, the aperture and center frequency of the transducer, the received transducer location are studied. Results show that the aperture, the center frequency, and the incident angle of the transducer are the most important factors in controlling the directivity of the resulting the LCR wave fields.

3.1 The relationship between the ultrasonic bulk wave and loading

The LCR method for stress detection is based on the principle that when the possible stress and ultrasound velocity are in the same direction, the sensitivity between stress and velocity are at a maximum. The expression for ultrasonic velocity in stressed media is firstly given by Hughes and Kelly (1953) and the detailed procedures (Appendix A) are offered by Takahashi and Motegi (2015).

The diagram shown in Fig. 3.1 is for the most sensitive case where the longitudinal wave propagation is in the same direction as the loading, serving as a guide for where the LCR wave method is best to applied stress (or residual stress) characterization.

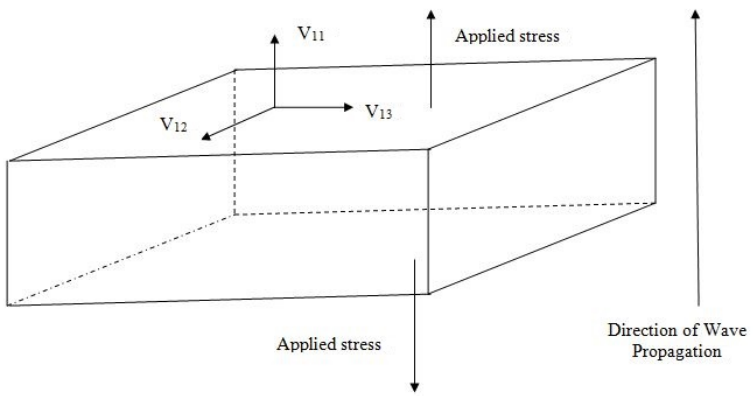

Figure 3.1: Speed of plane waves and stress field on the orthogonal coordinate system.

Usually the LCR wave method has been widely used for detecting stress that parallel to the surface of the media (like the welding area of the steel). While theoretically the LCR wave should travel parallel to the surface, it travels at an angle below the surface, as shown in Fig. 3.2.

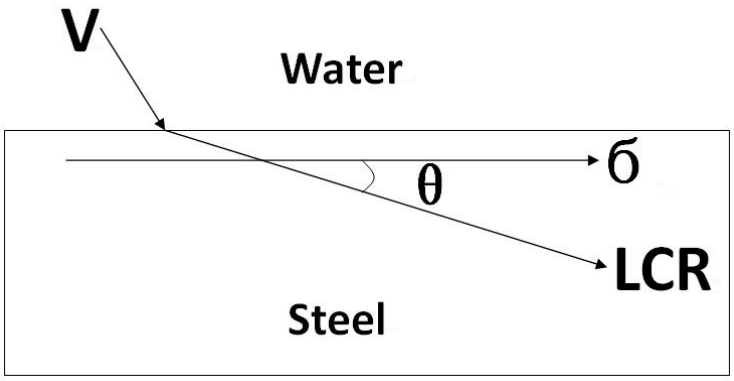

Figure 3.2: Direction difference between the LCR wave and stress.

Fig. 3.2 shows that there is an angle θ between the stress σ and the LCR wave that can decrease the sensitivity between the LCR wave and the stress, so there is a need to decrease the angle θ to increase the sensitivity.

3.2 The generation of the LCR wave

When ultrasound is transmitted from one medium to another, reflection and refraction will occur at the interface. For example, when a longitudinal wave is transmitted from water to steel, both longitudinal and transverse waves will be generated in the steel. The angles for the transmitted waves follow Snell's law:

$$\frac{C_{L1}}{\sin\alpha} = \frac{C_{L2}}{\sin\beta_L} = \frac{C_{S2}}{\sin\beta_S} \tag{3.1}$$

where C_{L1} is the longitudinal velocity in the water, C_{L2} and C_{S2} are the longitudinal and transverse velocities, respectively, in the steel.

According to Snell's law, as the incident angle α increases, the refraction angle β_L will reach 90^o. The vale when β_L reaches 90^o, is called the first critical angle and a wave knows as the LCR wave or creeping wave forms, as shown in Fig. 3.3. In principle this LCR wave or creeping wave (Langenberg et al., 1990) propagates parallel to the interface of water and steel, but in reality the wave is transmitted at an angle to the interface.

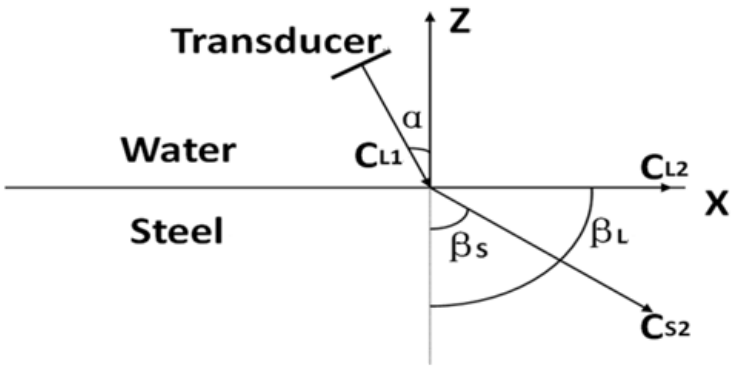

Figure 3.3: The generation of the LCR wave.

3.3 The acoustic field of the LCR wave

The numerical method for the acoustic field calculation has already been well shown (Belgroune et al., 2008; Matsushima and Shimobaba, 2009). When considering a 2D model (Fig. 3.4), the wave equation can be described by a scalar potential $\varphi(x, z, t)$ and a vector potential $\vec{\psi}(x, z, t)$:

$$\nabla^2\varphi = \frac{1}{C_L^2}\ddot{\varphi} \tag{3.2}$$

$$\nabla^2\vec{\psi} = \frac{1}{C_T^2}\ddot{\vec{\psi}} \tag{3.3}$$

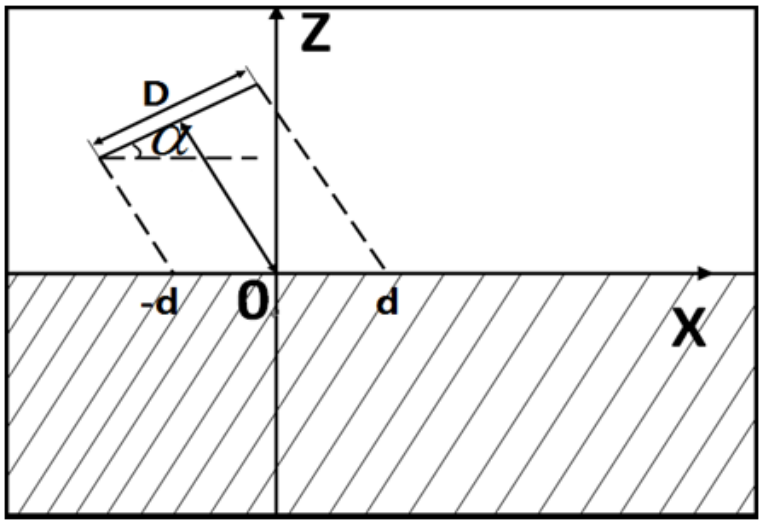

Figure 3.4: Schematic diagram for simulating the LCR wave.

Applying the Fourier transform to both space (x direction) and time (t) domain, for the scalar potential $\varphi(x, z, t)$:

$$\varphi^*(k_x, z, \omega) = \frac{1}{2\pi} \int_{-\infty}^{+\infty} \int_{-\infty}^{+\infty} \varphi(x, z, t) e^{-j\omega t} e^{-jk_x t} dx dt \tag{3.4}$$

$$\varphi^*(k_x, z, \omega) = Ae^{-jk_{f1}z} + Be^{jk_{f1}z} \tag{3.5}$$

where $k_{f1} = \sqrt{\omega^2/C_L^2 - k_x^2}$

It is the same for vector potential $\vec{\psi}(x, z, t)$ and $\vec{\psi}^*(k_x, z, \omega)$:

$$\vec{\psi}^*(k_x, z, \omega) = \frac{1}{2\pi} \int_{-\infty}^{+\infty} \int_{-\infty}^{+\infty} \vec{\psi}(x, z, t) e^{-j\omega t} e^{-jk_x t} dx dt \tag{3.6}$$

$$\vec{\psi}^*(k_x, z, \omega) = Ce^{-jk_{f2}z} + De^{jk_{f2}z} \tag{3.7}$$

where $k_{f2} = \sqrt{\omega^2/C_T^2 - k_x^2}$

For the solid, similarly to the Fourier transform the potential function can be expressed as:

$$\varphi^*(k_x, z, \omega) = T_1 e^{-k_c z} \tag{3.8}$$

$$\vec{\psi}^*(k_x, z, \omega) = T_2 e^{-k_s z} \tag{3.9}$$

Where T_1 and T_2 are the transmission coefficients, and $k_c = \sqrt{\omega^2/v_c^2 - k_x^2}$, $k_c = \sqrt{\omega^2/v_s^2 - k_x^2}$

According to the relationship between the potential and the displacement $\vec{u} = \nabla\varphi + \nabla \times \vec{\psi}$, the normal displacement in the solid can be expressed as:

$$\vec{u_z}^*(k_x, z, \omega) = -jk_c T_1 e^{-jk_c z} + jk_s T_1 e^{-jk_s z} \tag{3.10}$$

According to the relationship between stress and strain and the relationship between strain and displacement, the normal stress in the solid can be written as:

$$\begin{aligned}\sigma^*_{zz}(k_x,z,\omega) &= -\rho_s\omega_s^2\varphi_s^* - 2\mu_s(\frac{\partial^2\varphi_s^*}{\partial x^2} - \frac{\partial^2\vec{\psi}_s^*}{\partial x\partial z}) \\ &= -\rho_s\omega_s^2 T_1 e^{-jk_c z} - 2\mu_s[-k_x^2 T_1 e^{-jk_c z} - k_x k_s T_2 e^{-jk_s z}] \\ &= (2\mu k_x^2 - \rho_2\omega^2)T_1 e^{-jk_c z} + 2\mu k_x k_s T_2 e^{-jk_s z}\end{aligned} \tag{3.11}$$

The tangential stress in the solid can be written as:

$$\begin{aligned}\sigma^*_{zx}(k_x,z,\omega) &= \mu_s(2\frac{\partial^2\varphi_s^*}{\partial x\partial z} + \frac{\partial^2\vec{\psi}_s^*}{\partial x^2} - \frac{\partial^2\vec{\psi}_s^*}{\partial z^2}) \\ &= \mu_s[2k_x k_c T_1 e^{-jk_c z} - k_x^2 T_2 e^{-jk_s z} + k_s^2 T_2 e^{-jk_s z}] \\ &= \mu_s[2k_x k_c T_1 e^{-jk_c z} + (k_s^2 - k_x^2)T_2 e^{-jk_s z}]\end{aligned} \tag{3.12}$$

To simplify the model, the acoustic pressure from the transducer can be projected to the interface of the water and the steel, and the excitation on this interface can then be defined as an applied stress σ_{source} (Fig. 3.4), in time domain which can be expressed as:

$$\sigma_{source}(x, z=0, t) = \begin{cases} Ae^{[j(kx\sin\theta - \omega t)]} & , \quad |x| < d \\ 0 & , \quad |x| \geq d \end{cases} \tag{3.13}$$

where A is the excitation amplitude; $d = \frac{1}{2}D/\cos\theta$, D is the diameter of the transducer; $k = \omega/c$; c is the velocity of the water; ω is the angular frequency.

Applying the Fourier transform for the σ_{source}, yields:

$$\sigma^*_{source}(k_x, z=0, \omega) = \frac{1}{2\pi}\int_{-\infty}^{+\infty}\int_{-\infty}^{+\infty}\sigma_{source}(x, z=0, t)e^{-j\omega t}e^{-jk_x t}dxdt \tag{3.14}$$

Considering boundary conditions that the normal stress continuous and the tangential stress goes to zero at the water/steel boundary:

$$\begin{aligned}\sigma^*_{zz}(k_x, z=0, \omega) &= \sigma^*_{source}(k_x, z=0, \omega) \\ \sigma^*_{zx}(k_x, z=0, \omega) &= 0\end{aligned} \tag{3.15}$$

Solving Eq. 3.15 yields the values of T_1 and T_2, then applying an inverse Fourier transform for normal stress $\vec{\sigma_{zz}}$ to time domain, the acoustic field in the steel can be obtained, as shown in Eq. 3.16.

$$\sigma^*_{zz}(x,z,t) = \int_{-\infty}^{+\infty}\int_{-\infty}^{+\infty}\sigma^*_{zz}(k_x,z,\omega)e^{j\omega t}e^{jk_x t}dk_x d\omega \tag{3.16}$$

3.4 A typical received signal from the model

The simulation of the acoustic field of the LCR wave is calculated using MATLAB. The parameters used are shown in Table 3.1.

Table 3.1: Material properties of water and steel used for calculation

Material	Density (g/cm^2)	Longitudinal Velocity (m/s)	Transversal Velocity (m/s)
Water	1.0	1480	$---$
Steel	7.8	5940	3230

The acoustic wave field includes longitudinal, transverse, and head waves in the steel. The parameters used here are: a transducer aperture of 6 mm, a transducer frequency of 2 MHz, and an incident transducer angle is 14.5^o. To satisfy the bound conditions, the head wave and transverse wave are always linked to each other at the interface.

The received signal at different locations can be obtained, and a typical example of a displacement signal received at a location (with distance L) is 75 mm from the incident center 0. An angle β at 45^o from the x axial (as shown in Fig. 3.5) in the steel is shown in Fig. 3.6. It clearly shows the longitudinal, transverse waves and their relative amplitudes.

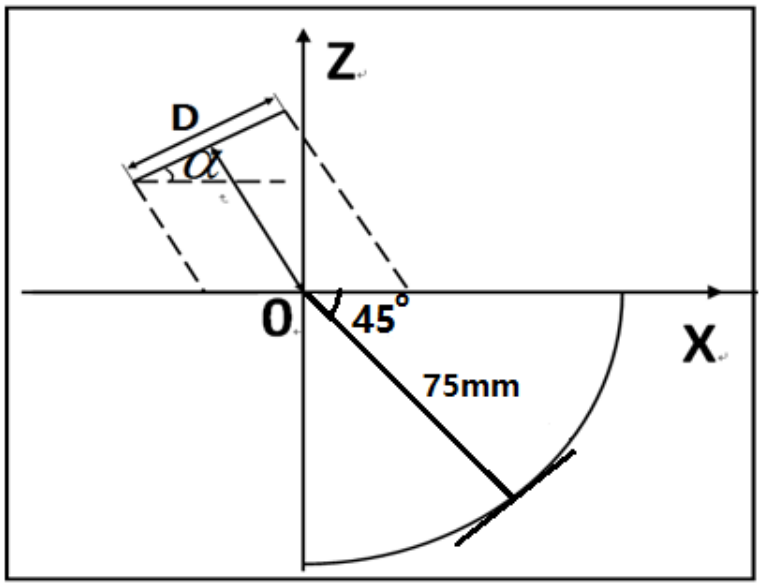

Figure 3.5: Schematic diagram shown the location of the receiving transducer.

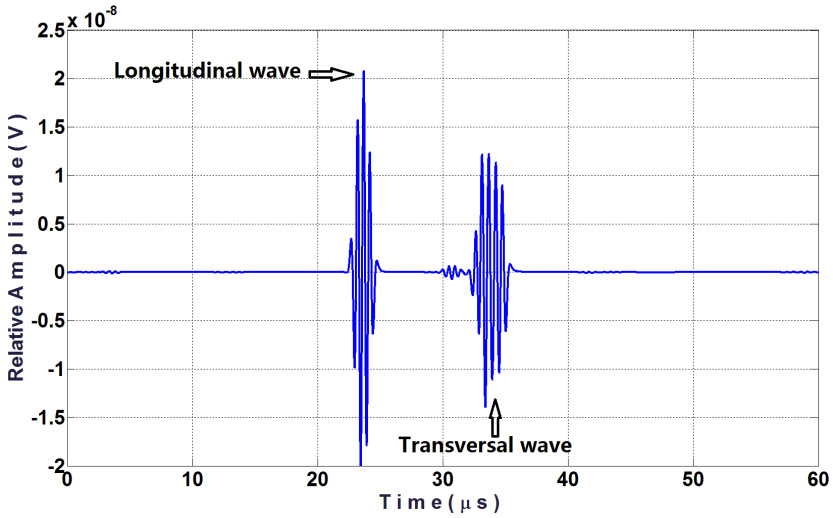

Figure 3.6: A typically received signal for the LCR wave.

3.5 The analysis of parameters that control the directivity of the LCR wave.

The new model described above was used to simulate and investigate the effects of various parameters on the resulting wave fields, and this section will describe a sensitivity analysis. The signals were calculated and assumed to be received at points on a 90^o arc with its center at the point of incidence for the transducers central ray onto the interface, as shown in Fig. 3.7. The receiving distance L from the measurement point on the interface is 75 mm.

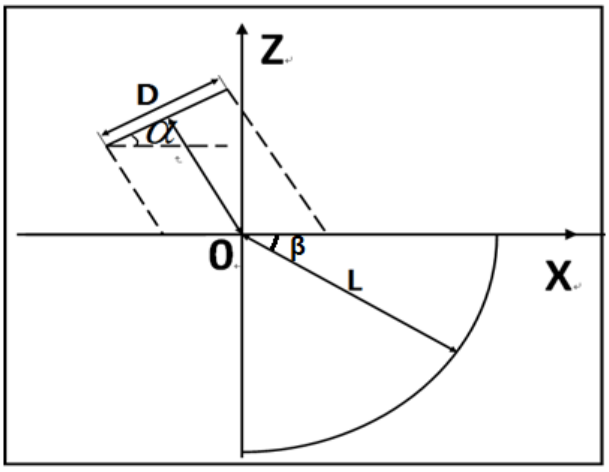

Figure 3.7: Schematic diagram showing the model shown different parameters.

The amplitude of the LCR wave at different locations on the arc was used to plot the directivity of the LCR wave. A comparison of the directivity of the LCR wave obtained by this model with that for the best estimate of the corresponding case shown in the literature (Chaki et al., 2013) is presented in Fig. 3.8. The current data and that taken from the literature are seen to be in general agreement, in terms of both magnitude and angle.

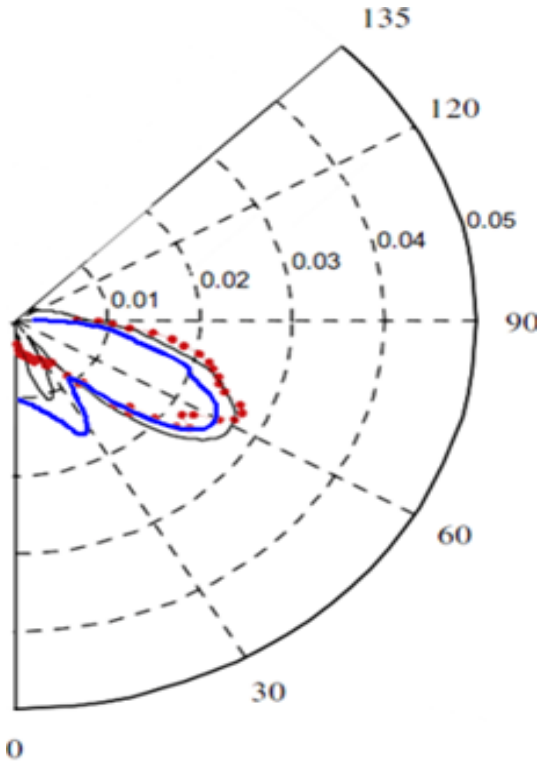

Figure 3.8: Comparison of the LCR wave from the literature and that from the current model: current study (blue curve) and corresponding data from the literature (Chaki, et al., 2013), black curve and red dot.

The frequency (F), the aperture (D) and the incident angle (α) of the transducer and the receiving locations (L) were all varied to permit estimation of their effects on the directivity of the LCR wave (Fig. 3.7). The values of these parameters, for three cases, are shown in Table 3.2.

Table 3.2: The values of the parameters for the three configurations.

	F (frequency:MHz)	D(mm)	α (angle:degree)	L(mm)
1	1.75	6	13.5	50
2	2	7	14.5	60
3	2.25	8	15.5	70

The Orthogonal Experiment Method (Huang et al., 2004) was used for the analysis of the effects of the variation of these parameters on the resulting data. The Orthogonal Experiment Method was used to study the effects on a system when more than two parameters are involved and attempt to provide a sensitivity analysis using an optimized set of simulations (or experiments). The Orthogonal Experiment Table used for this application is L_3^{27}. (shown in Appendix B)

In the L_3^{27} table, $F * D\_1$ and $F * D\_2$ are the two interaction effect of frequency (F) and aperture (D), parameters that can affect one another. With respect to the Orthogonal Experiment Method, Range Analysis and Analysis of Variance are two typical data analysis methods. Range Analysis is used to order the parameters in importance while Analysis of Variance is necessary to make sure whether the result has statistical significance.

For the L_3^{27} table, there are 27 combinations of parameters that can demonstrate the contribution of different parameters. The results of these 27 cases are shown in Fig. 3.9 through to Fig. 3.13. The amplitude of the curves in these figures is used to define the directivity.

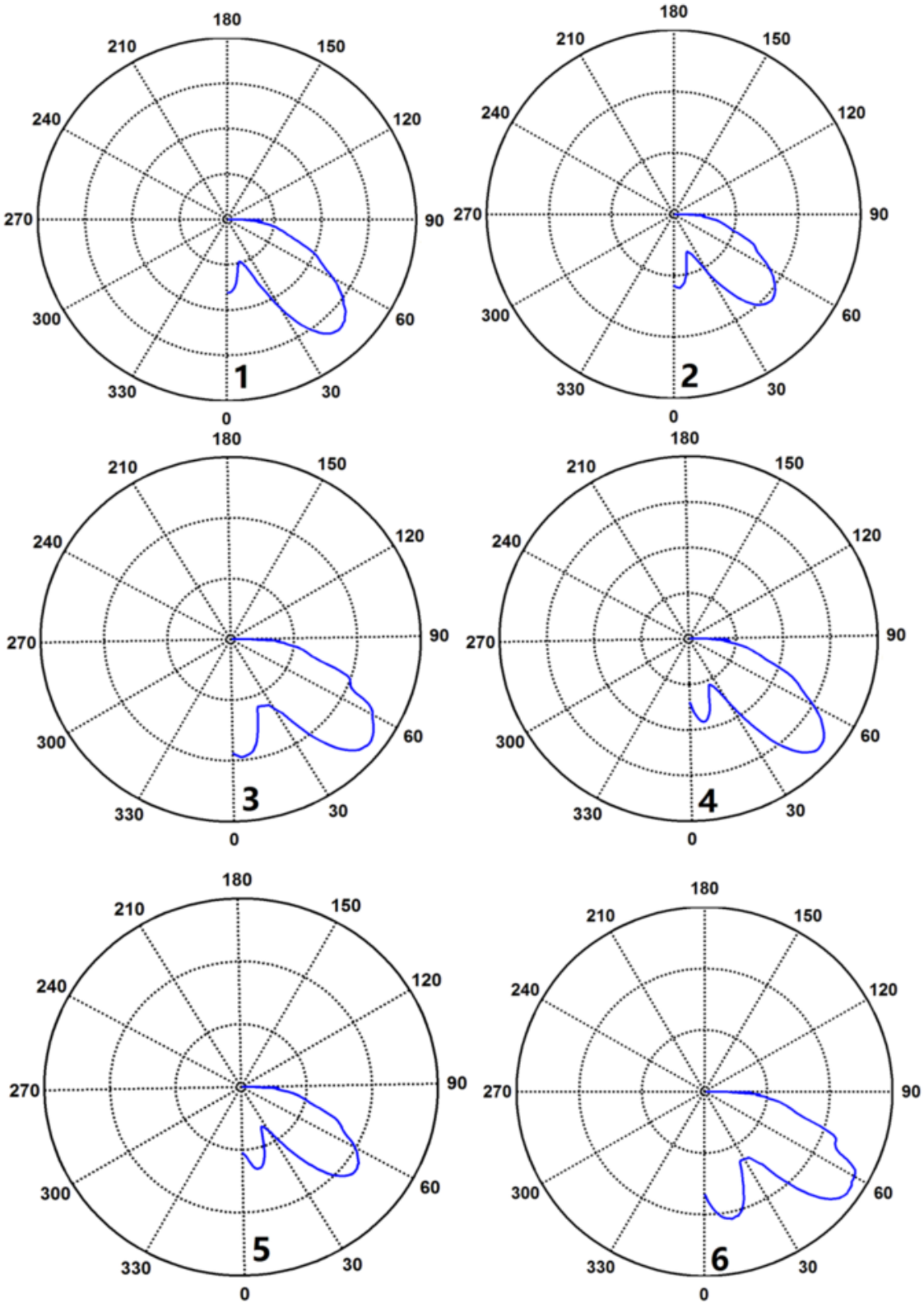

Figure 3.9: The LCR wave beam shown from case '1' to '6' for the L_3^{27} table.

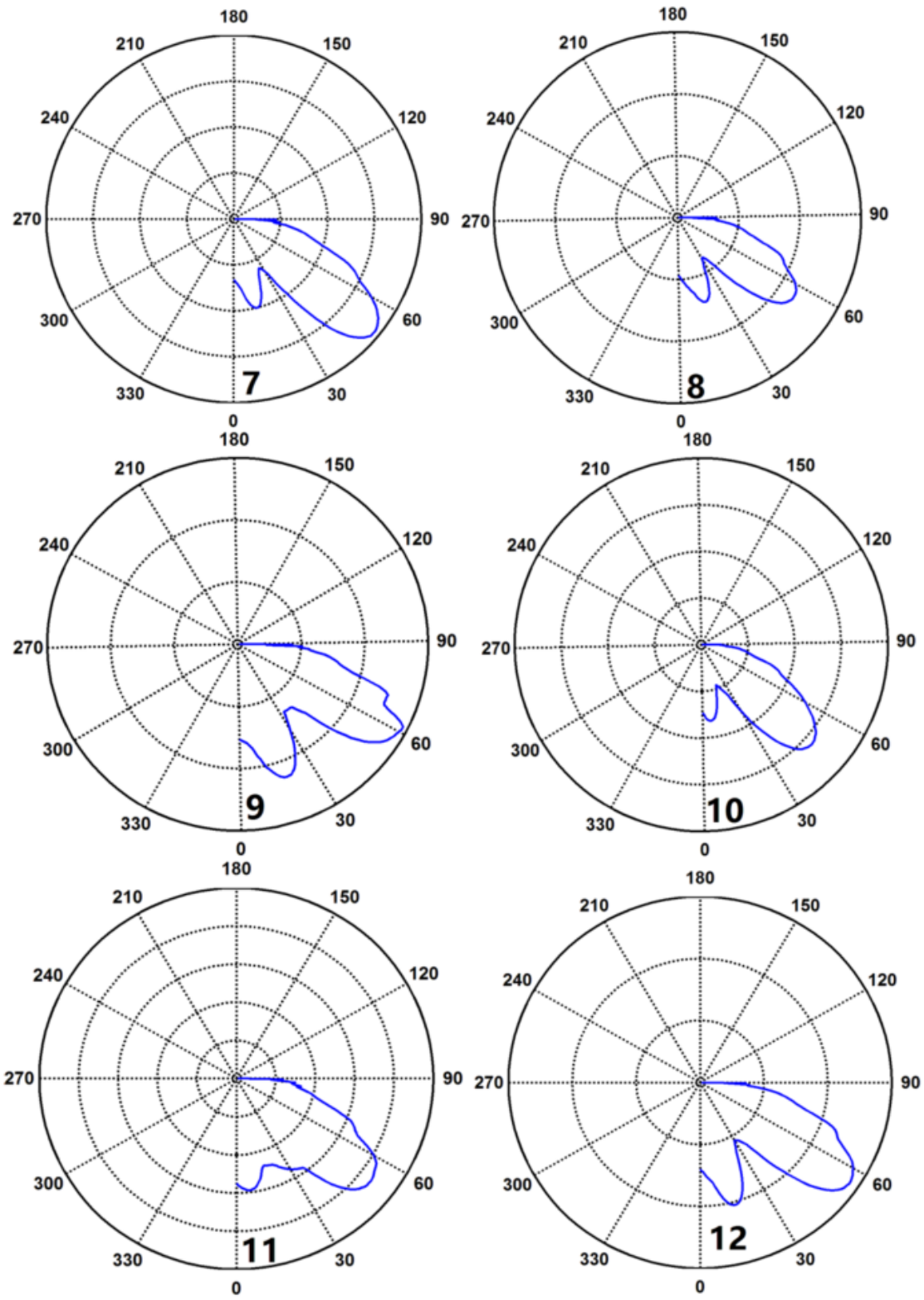

Figure 3.10: The LCR wave beam shown from case '7' to '12' for the L_3^{27} table.

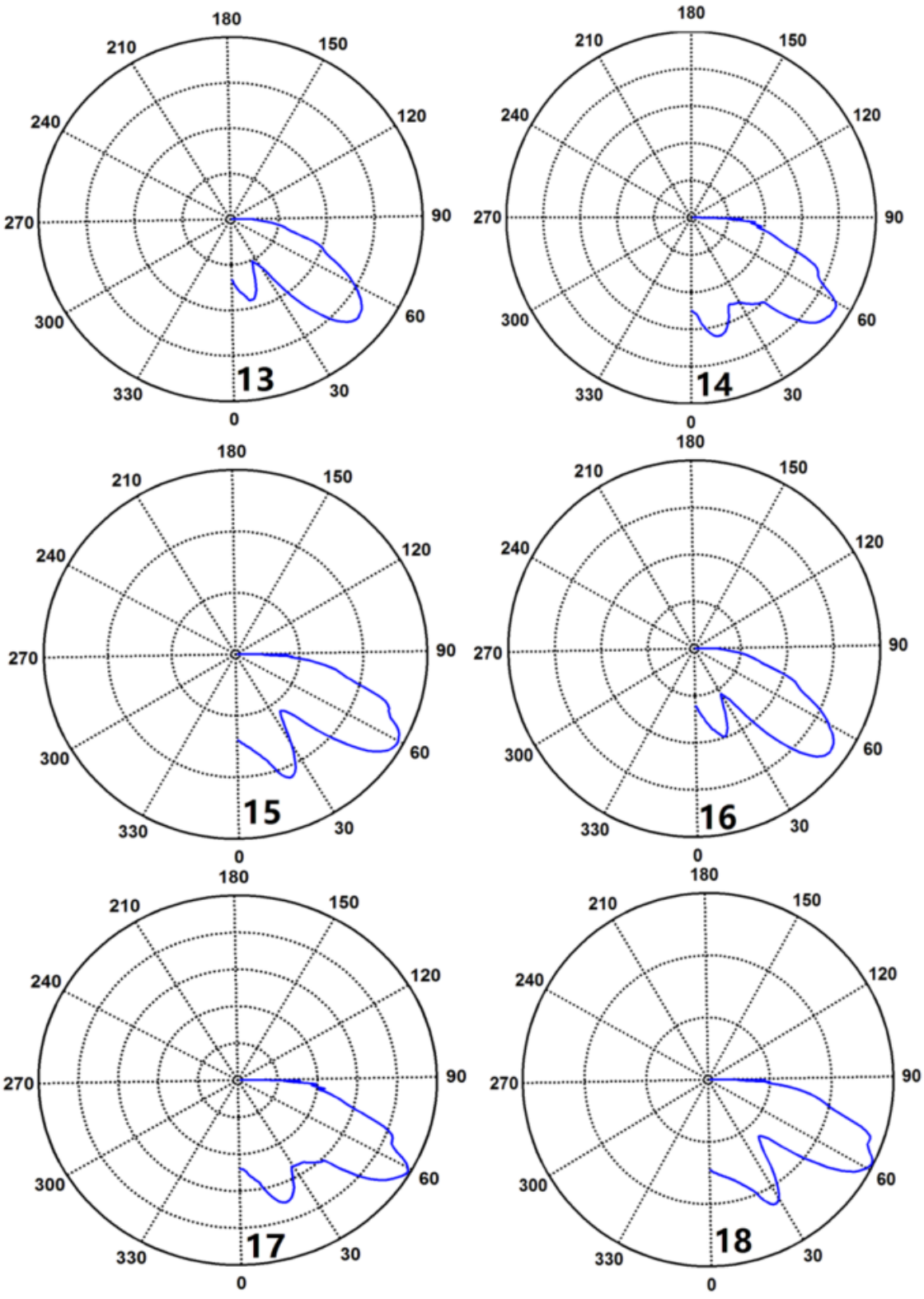

Figure 3.11: The LCR wave beam shown from case '13' to '18' for the L_3^{27} table.

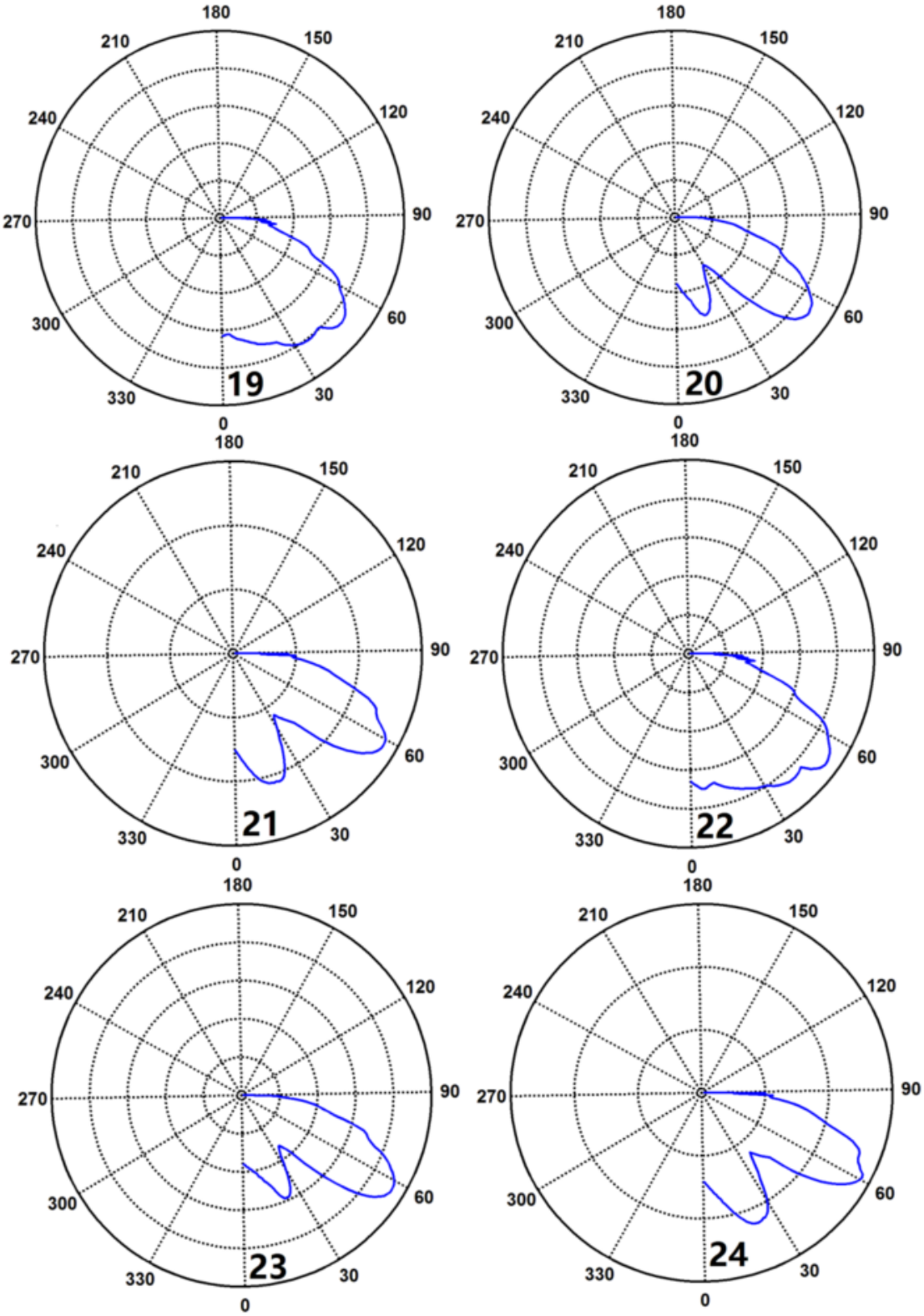

Figure 3.12: The LCR wave beam shown from case '19' to '24' for the L_3^{27} table.

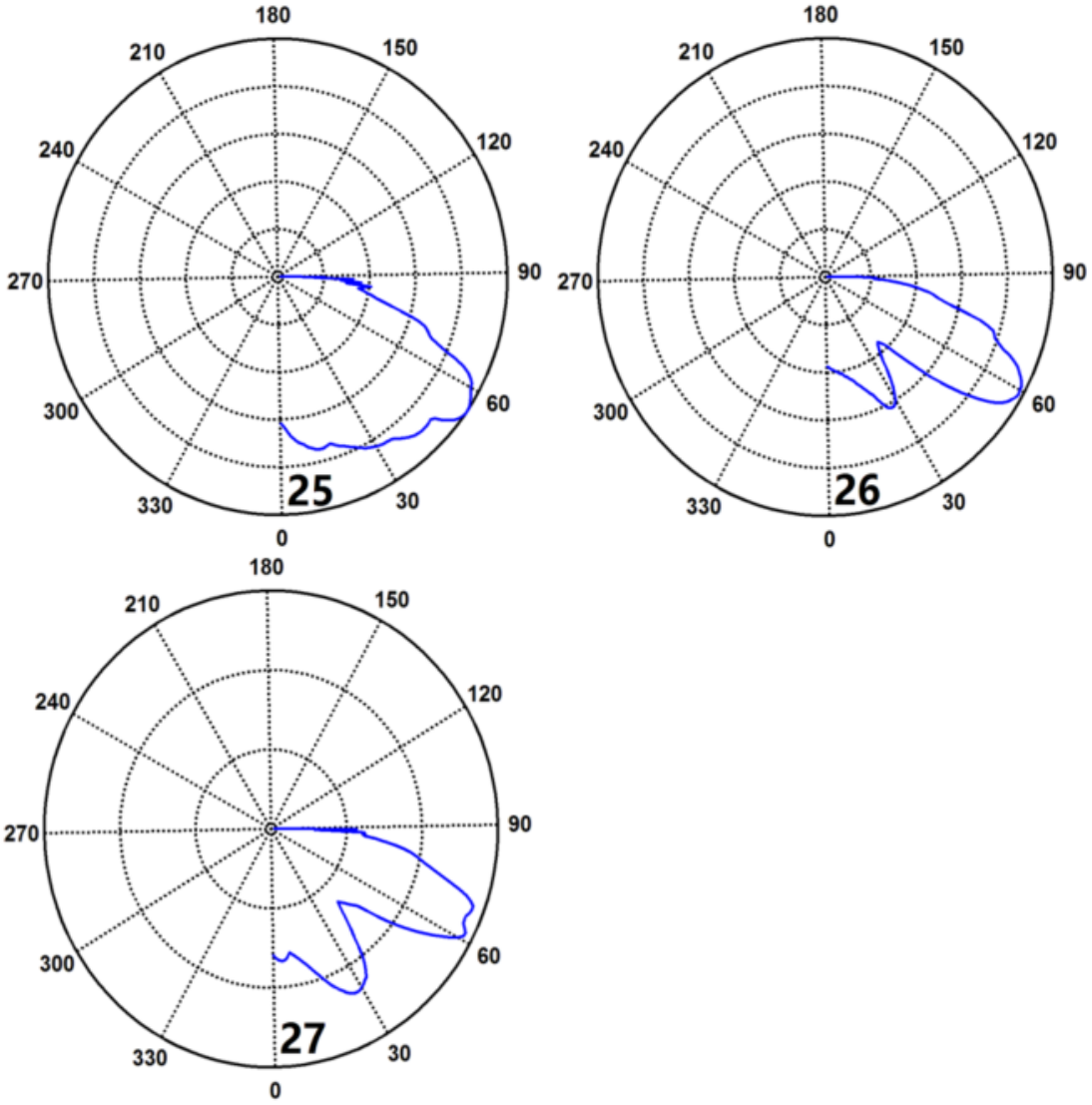

Figure 3.13: The LCR wave beam shown from case '25' to '27' for the L_3^{27} table.

For example, for case one, shown in the Fig. 3.14, the red point shows the amplitude of the curve and the green line goes through the origin and the red point shows the directivity of the curve, 45^o. All the following analysis has been based on this method to acquire the directivity of the curve for each case.

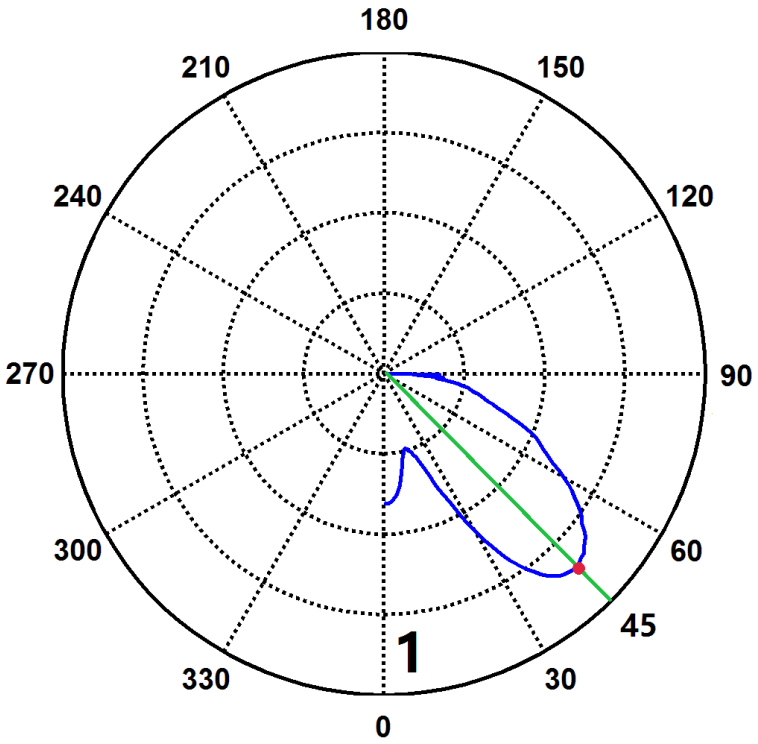

Figure 3.14: Schematic diagram shown the definition of the directivity for the LCR wave.

The analysis for different cases is shown in Table 3.3. These data were obtained using SPSS (Cui et al., 2007), where SPSS stands for Solutions Statistical Package for the Social Sciences, an IBM statistical software tools that can be used for data analysis in many areas. There is a mode in the software that can be used for orthogonal experiment data analysis that shows that F (frequency), D (aperture), $F * D\_1$ and Angle are the main parameters, and their significant are all less than 0.005. For a corrected Model the value should be less than 0.005, where this is defined as a parameter to judge the result (Cui et al., 2007), i.e., the result has valid statistical meaning and it is reliable.

Range Analysis of the results is given in Table 3.4. Based on the Range data in the table, the significance order for the key parameters are $Angle > D > F > F * D\_1$ (Interaction effect). Based on both Range Analysis and Analysis of Variance, it has been shown that F (frequency), D (aperture), Angle, and $F * D\_1$ are the import factors that influence the directivity of the LCR wave, and their order of importance is $Angle > D > F > F * D\_1$ (Interaction effect).

Table 3.3: Analysis of Variance of the result from L_3^{27} table

Source	**Type III Sum of Squares**	**Mean Square**	**Sig.**
F	98.74	49.37	.000
D	180.96	90.48	.000
$\boldsymbol{F * D\_1}$	11.19	5.59	.024
$\boldsymbol{F * D\_2}$	2.3	1.15	.374
Angle	324.52	162.26	.000
L	5.41	2.7	.122
Error	12.89	1.07	
Total	80129	27	
Corrected Total	639.19		

Table 3.4: Range Analysis of the result from L_3^{27} table

	F	**D**	$\boldsymbol{F * D\_1}$	**Angle**
Mean value 1	51.667	51.000	54.111	49.778
Mean value 2	54.899	54.444	53.556	54.778
Mean value 3	56.222	57.333	55.111	58.222
Range	4.555	6.333	1.555	8.444

The variation trend for the important parameters are shown in Fig. 3.15. As the value of the parameter F (frequency), D (aperture) and Angle increased, the directivity of the LCR wave relative to the horizontal direction changed. To increase the directivity of the LCR wave, the value of the parameters should be increased. As shown above, there are interaction effects between F (frequency) and D (aperture). Binary Table (Cui et al. 2007) is used to provide further analysis of two interaction factors:

their joint contributions to the results. Table 3.5 is the Binary Table for F (frequency) and D (aperture), showing their contribution to the directivity with different values.

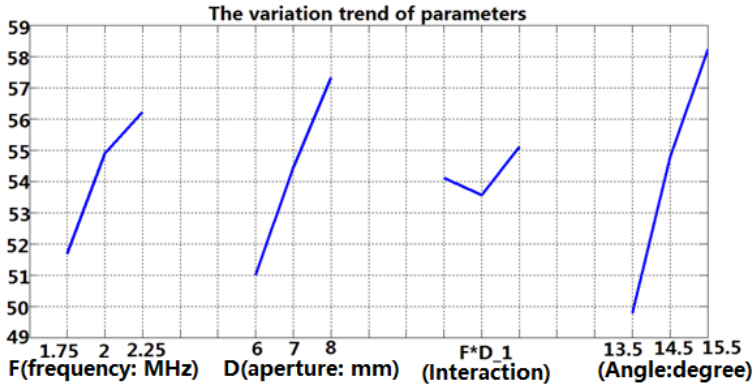

Figure 3.15: The variation trend for the important parameters.

Table 3.5: Binary Table for F (frequency) and D (aperture)

D_F	**1.75**	**2**	**2.25**
6	48	51.33	53.67
7	51	55.67	56.67
8	56	57.67	58.33

A Biplot Mapping (Chen et al., 2007) is shown in Fig. 3.16 corresponding to the data in the Binary Table. It visualizes the trends for variations more clearly compared to Binary Table. As shown in the figure, as F (frequency) and D (aperture) go up, the direction of the LCR wave exhibits a trend to go up to 90^o, the directivity can reach nearly 60^o when the value of D (aperture) is 8 mm and the frequency value is 2.25 MHz.

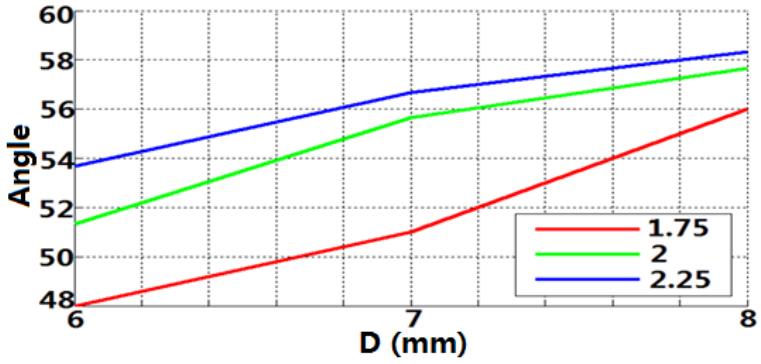

Figure 3.16: Biplot Mapping of F (frequency) and D (aperture).

3.6 The contribution of transducer aperture to the LCR wave directivity

As shown in the last section, the center frequency, the aperture and the incident angle of the transducer all make significant contributions to the directivity of the LCR wave. The incident angle effect is, as has already been discussed in the literature (Chaki et al., 2013), that if the angle about 1^o larger than the first critical incident angle, the directivity of the LCR wave can reach a maximum. Beam parameters are shown in Fig. 3.17 for larger transducer aperture ranges.

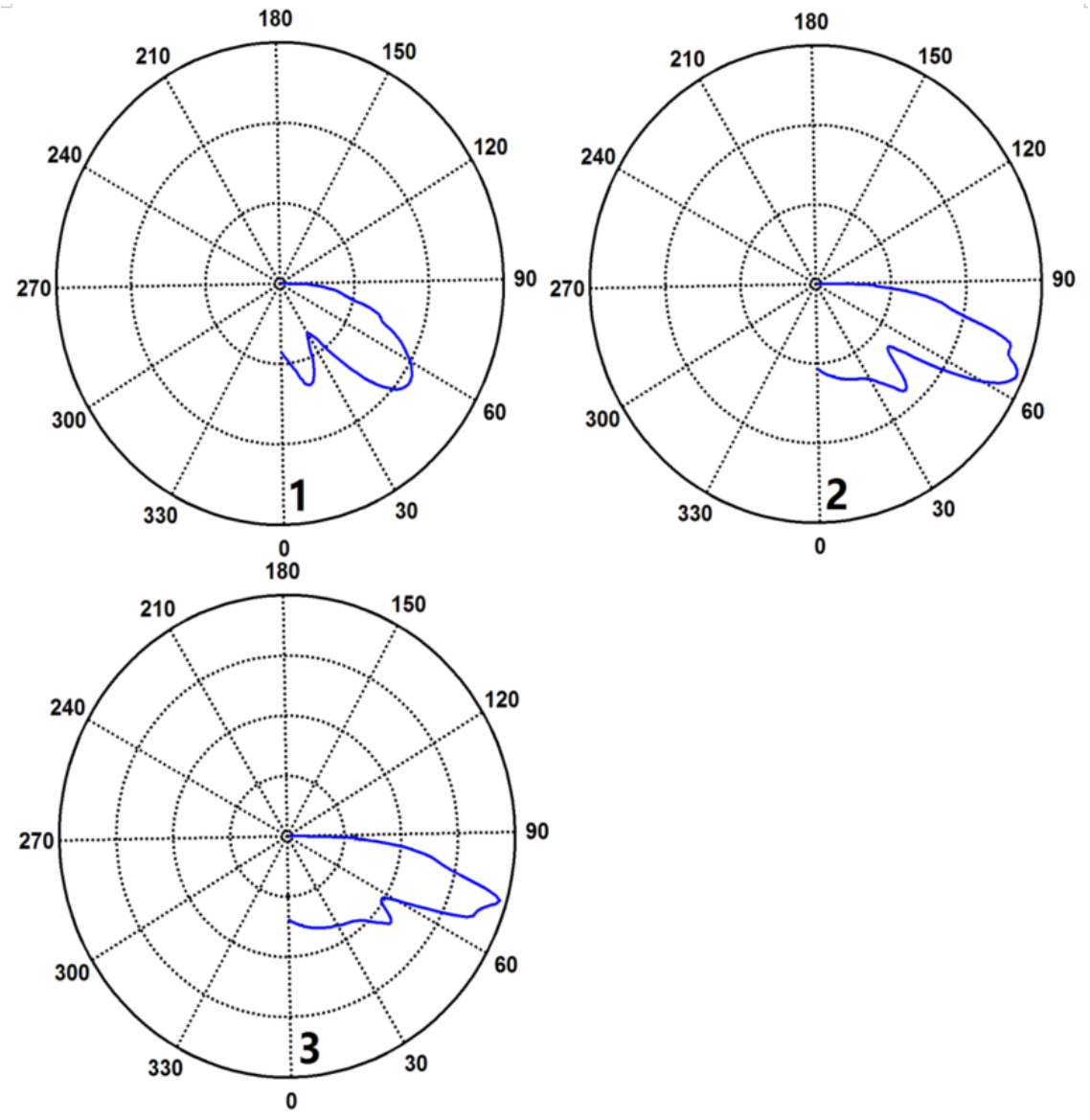

Figure 3.17: Comparing results for different transducer apertures.

In Fig. 3.17, the first plot, marked '1', refers to the case when the aperture is 6 mm, with the transducer center frequency is 2 MHz, the incident angle is 15^o, and the directivity is about 55^o; the plot marked "2" refers to the case when the aperture is 12 mm, the other parameters the same as in case 1, and the directivity about 65^o. The plot marked "3" refers to the case when the aperture is 18 mm, with others parameters the same as for the other two cases, and the directivity about 75^o. As the transducer aperture increases the directivity of the LCR wave trends to increase to 90^o, meaning that increasing the aperture of the transducer can increase the directivity of the LCR wave and increase the sensitivity between the LCR wave and residual (applied) stress in the samples.

3.7 Chapter summary

The effects of transducer and system configuration for the generation of the LCR or creeping wave have been studied. A new MATLAB-based model using a Spatial Fourier Analysis method is described, providing results in good general agreement with more complex and previously published models. The model was used to investigate the effect of various parameters on the directivity of the LCR wave. The Orthogonal Experiment Method was used to analyze the effects of parameters as seen in the model data. The data show that F (the frequency of the transducer), D (the aperture of the transducer), α (the incident angle), and F*D (the interaction between F and D) all influence the directivity of the LCR wave, and their order of significance is $Angle > D > F > F * D\_1$ (Interaction effect). This model data provides insights into the penetration of the wave into a sample. When the amplitude of the LCR wave and the possible stress in the same direction, the sensitivity of the LCR wave to stress can reach a maximum.

CHAPTER 4. CHARACTERIZATION OF LAMB WAVES PROPAGATING IN STRESSED PLATE

This chapter discusses wave propagation in the stressed plate, following and extending the approach by Gandhi (2010). The governing equation for the Lamb wave propagating in the stressed plate can be obtained by considering wave motion equations under loading for bulk waves and Lamb waves propagating in an anisotropic plate.

4.1 Governing wave equations

If a wave travels in an infinite medium, it is known as a bulk wave. Depending on the vibration direction and the propagation direction of the waves, bulk waves can be divided into longitudinal waves (when the direction of vibration and propagation direction are parallel) and shear waves (when the direction of vibration and propagation direction are perpendicular). When the wave travels along the boundaries of the medium, or the boundaries between two media, it is known as a guided wave. Guided waves (Rose, 2004) are widely used in the Nondestructive Testing (NDT) field because of its long propagation distances and high sensitivity to the properties of the material. When a guided wave propagates in plate-like samples, it is known as a Lamb wave. Lamb waves are somewhat complex because the velocity and frequency of the wave have a relationship with the thickness of the plate, a phenomenon called dispersion. From their physical description, Lamb waves are formed by the mixing of different bulk waves in thin plane-shaped media to form symmetry and anti-symmetry modes. Lamb waves are widely used for studying possible fatigue cracks and defects in pipes and rods. Rayleigh waves (also known as surface wave) propagate along the surface of a semi-infinite medium, with amplitudes that decay exponentially with the depth below the surface, and Rayleigh waves are usually applied for de-

tecting possible defects along the material surface. Stonely wave usually exist within the interface of two media. Schematic for various waves are shown as Fig. 4.1.

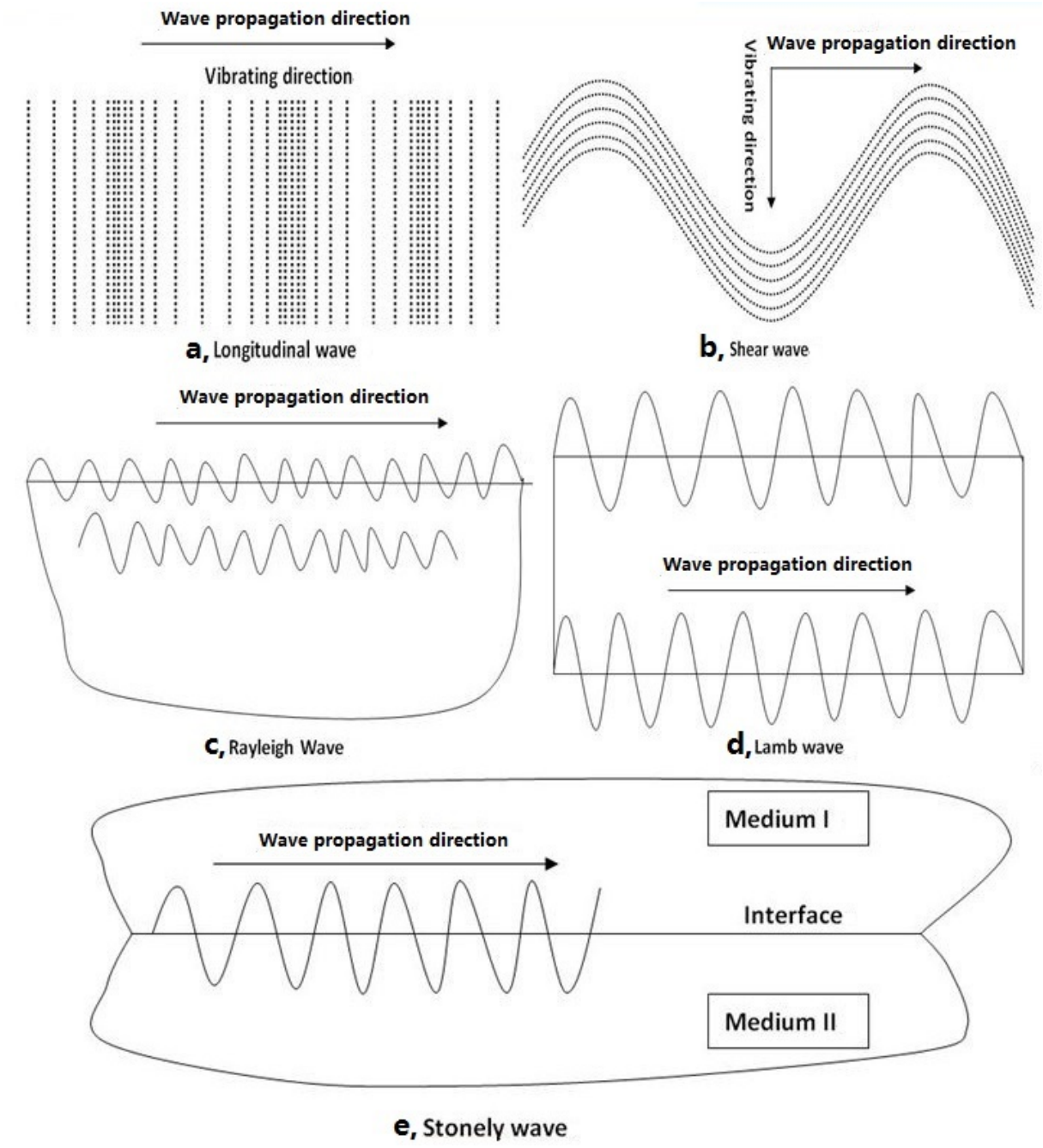

Figure 4.1: Schematic diagram showing various waves: a, Longitudinal wave; b, Shear wave; c, Rayleigh wave; d, Lamb wave; e, Stonely wave.

4.1.1 Governing wave equations for isotropic materials

The governing equations for the wave propagation in isotropic material are well-established (Ensminger and Bond 2011), and combined with the equation of motion produces:

$$\sigma_{ij,j} + \rho f_i = \rho \ddot{u}_i \tag{4.1}$$

the strain-displacement relation:

$$e_{ij} = \frac{1}{2}(u_{i,j} + u_{j,i}) \tag{4.2}$$

and the constitutive equation:

$$\sigma_{ij} = \lambda e_{kk}\delta_{ij} + 2\mu e_{ij} \tag{4.3}$$

can get the yield relationship:

$$(\lambda + \mu)u_{j,ji} + \mu u_{i,jj} + \rho f_i = \rho \ddot{u}_i \tag{4.4}$$

Or in the form:

$$(\lambda + \mu)\nabla(\nabla \cdot \vec{u}) + \mu\nabla^2\vec{u} + \rho\vec{f} = \rho\ddot{\vec{u}} \tag{4.5}$$

Where

$$\nabla^2 = \frac{\partial^2}{\partial x_1^2} + \frac{\partial^2}{\partial x_2^2} + \frac{\partial^2}{\partial x_3^2} \tag{4.6}$$

$$\nabla = \frac{\partial}{\partial x_1}\vec{i_1} + \frac{\partial}{\partial x_1}\vec{i_2} + \frac{\partial}{\partial x_1}\vec{i_3} \tag{4.7}$$

The above Eq. 4.4 and Eq. 4.5 are the government equations for waves propagating in isotropic materials. They can be also written in Cartesian coordinates:

$$
\begin{aligned}
(\lambda+\mu)\frac{\partial}{\partial x_1}(\frac{\partial u_1}{\partial x_1}+\frac{\partial u_2}{\partial x_2}+\frac{\partial u_3}{\partial x_3})+\mu\nabla^2 u_1+\rho f_x=\rho\frac{\partial^2 u_1}{\partial t^2}\\
(\lambda+\mu)\frac{\partial}{\partial x_2}(\frac{\partial u_1}{\partial x_1}+\frac{\partial u_2}{\partial x_2}+\frac{\partial u_3}{\partial x_3})+\mu\nabla^2 u_2+\rho f_y=\rho\frac{\partial^2 u_2}{\partial t^2}\\
(\lambda+\mu)\frac{\partial}{\partial x_3}(\frac{\partial u_1}{\partial x_1}+\frac{\partial u_2}{\partial x_2}+\frac{\partial u_3}{\partial x_3})+\mu\nabla^2 u_3+\rho f_z=\rho\frac{\partial^2 u_3}{\partial t^2}
\end{aligned}
\tag{4.8}
$$

Characteristics of guided waves can be obtained by combining the above equations with the boundary equations.

4.1.2 Governing wave equations for an-isotropic materials

For anisotropic media, the equation of motion, the strain-displacement relationship, and the constitutive equation are all needed to generate the wave government equation (Rose 2004); in this case the constitutive equation should be written as:

$$\sigma_{ij}=C_{ijlm}e_{lm} \tag{4.9}$$

Considering the equation of motion without external force:

$$\sigma_{ik,k}=\rho\ddot{u}_i \tag{4.10}$$

Combining Eq. 4.9 and Eq. 4.10, yields:

$$\sigma_{ij}=C_{ijlm}e_{lm,k} \tag{4.11}$$

Considering the strain-displacement relation (Eq. 4.2) and combining with Eq. 4.11, yields:

$$\rho\ddot{u}_i=\frac{1}{2}C_{ijlm}(u_{l,km}+u_{m,kl}) \tag{4.12}$$

Supposing the solution of the Eq. 4.12 to be of the form:

$$u_i=A_i e^{i(k_j x_j-\omega t)} \tag{4.13}$$

Where u_i represents the particle displacement; $A_i = A\alpha_i$, A is the amplitude while α_i represent the direction of displacement; k_i is the wave number, and ω is the angular frequency.

Substituting the expression of u_i into Eq. 4.13 to produce Eq. 4.12, and considering the symmetry of the stiffness tensor C_{ijlm}, yields:

$$(\rho\omega^2\delta_{im} - C_{ijlm}k_k k_l)u_m = 0 \tag{4.14}$$

Considering that $k_k = kn_k, k_l = kn_l$ (n_k, n_l are the normal cosine of the wave front) and $k = \omega/c$, rewritting Eq. 4.14 yields,

$$(\Gamma_{im} - \rho c^2\delta_{im})u_m = 0 \tag{4.15}$$

Where $\Gamma_{im} = C_{ijlm}n_j n_l$, known as Christoffel tensor. C_{ijlm} is the second-order elastic constant, and δ_{im} is the Cauchy stress tensor.

4.2 Acoustoelasticity

The acoustoelastic effect (Pao and Gamer, 1985) shows the relationship between the sound (ultrasound) velocity and possible stress in the elastic media. For the simplified case of infinitesimal deformations in perfectly elastic solids, the constitutive relationship between the stress and the strain is known as Hooke's law. While the velocity is determined by the second-order elastic constants (λ and μ) and the density of the material, when finite deformations are considered, the higher-order constants in the constitutive relationship should be considered, leading to a more complex relationship between the stress and the strain.

The scalar strain energy density function $W(E)$ can be expanded by a Taylor series expansion as a function of the strain E, expressed as Gandhi (2010):

$$W \approx C_0 + C_{ij}E_{ij} + \frac{1}{2}C_{ijkl}E_{ij}E_{kl} + \frac{1}{6}C_{ijklmn}E_{ij}E_{kl}E_{mn} + \cdots \tag{4.16}$$

Where **E** is the Lagrangian strain tensor and **C** is the elastic modulus with different orders.

The strain energy function should be zero and have a minimum with zero deformation [$(W(E_{ij} = 0) = 0)$], while the energy density function can be rewritten, removing the constant and linear term to yield:

$$W \approx \frac{1}{2}C_{ijkl}E_{ij}E_{kl} + \frac{1}{6}C_{ijklmn}E_{ij}E_{kl}E_{mn} + \cdots \tag{4.17}$$

Where C_{ijkl} are the second-order elastic constants and C_{ijklmn} are third-order elastic constants.

The stress related to the strain energy, which can be expressed as:

$$T_{ij} = \frac{\partial U}{\partial E_{ij}} \tag{4.18}$$

Combing Eq. 4.17 and Eq. 4.18, yields:

$$T_{ij} = C_{ijkl}E_{kl} + \frac{1}{2}C_{ijklmn}E_{kl}E_{mn} \tag{4.19}$$

4.3 Wave equations for the pre-stressed media

To analysis the relationship between wave velocity and higher-order elastic constants, the government equations for the wave propagating in the pre-stressed media must be established. As shown in Appendix A, natural state, initial state, and final state must be established for the pre-stressed media analysis. (Toupin and Bernstein, 1961). For easier reading, the definitions are repeated here.

As shown in Fig. 4.2, a physical particle in the natural, initial, and final state is represented by a superscript label 0, i , or f respectively. The position of a particle in the body at natural, initial, and final states are described by the vector ξ, X,and x respectively. The components of ξ in different directions refer to the natural coordinate denoted by Greek subscripts; the components of X refer to the initial coordinate, denoted by upper-case Roman subscripts, and the components of x refer to the final coordinate, denoted by lower case Roman subscripts. Then the vectors can be expressed in these three different configurations as: ξ_α, X_J and x_j $(\xi, X, x = 1, 2, 3)$.

From the natural to the initial states, the deformation is static and it can be expressed as $\mathbf{u}^i$; from the initial to the final states, the displacement can be written as $\mathbf{u}^f$. These vectors are related to the position vectors that can be written as:

$$\begin{aligned} \mathbf{u}^i(\boldsymbol{\xi}) &= \mathbf{X} - \boldsymbol{\xi} \\ \mathbf{u}^f(\boldsymbol{\xi}, t) &= \mathbf{x} - \boldsymbol{\xi} \end{aligned} \tag{4.20}$$

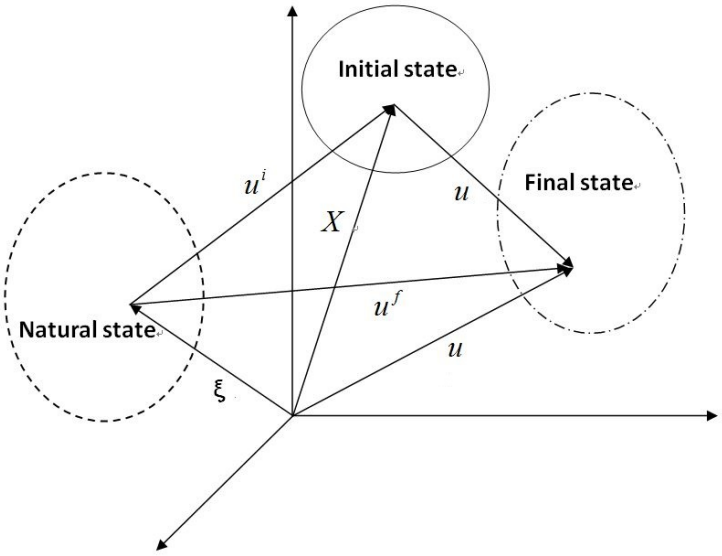

Figure 4.2: Coordinates describing a material point at the natural (ξ), initial (X), and final (x) configuration for a pre-deformed body.

Then the displacement from initial to final state can be written as:

$$\mathbf{u}(\boldsymbol{\xi}, t) = \mathbf{x} - \mathbf{X} = \mathbf{u}^f - \mathbf{u}^i \tag{4.21}$$

The Lagrangian strain tensor is defined as:

$$E_{ij} = \frac{1}{2}\left(\frac{\partial u_i}{\partial \xi_j} + \frac{\partial u_j}{\partial \xi_i} + \frac{\partial u_k}{\partial \xi_i}\frac{\partial u_k}{\partial \xi_j}\right) \tag{4.22}$$

The Lagrangian strain tensors in the initial and final states can be written as:

$$\begin{aligned} E^i_{\alpha\beta} &= \frac{1}{2}\left(\frac{\partial u^i_\alpha}{\partial \xi_\beta} + \frac{\partial u^i_\beta}{\partial \xi_\alpha} + \frac{\partial u^i_\lambda}{\partial \xi_\alpha}\frac{\partial u^i_\lambda}{\partial \xi_\beta}\right) \\ E^j_{\alpha\beta} &= \frac{1}{2}\left(\frac{\partial u^j_\alpha}{\partial \xi_\beta} + \frac{\partial u^j_\beta}{\partial \xi_\alpha} + \frac{\partial u^j_\lambda}{\partial \xi_\alpha}\frac{\partial u^j_\lambda}{\partial \xi_\beta}\right) \end{aligned} \tag{4.23}$$

Substituting $E^j_{\alpha\beta}$ from $E^i_{\alpha\beta}$, yields:

$$E_{\alpha\beta} = E^f_{\alpha\beta} - E^i_{\alpha\beta} = \frac{1}{2}\left(\frac{\partial u_\alpha}{\partial \xi_\beta} + \frac{\partial u_\beta}{\partial \xi_\alpha} + \frac{\partial u^i_\lambda}{\partial \xi_\alpha}\frac{\partial u_\lambda}{\partial \xi_\beta} + \frac{\partial u^i_\lambda}{\partial \xi_\beta}\frac{\partial u_\lambda}{\partial \xi_\beta}\right) \tag{4.24}$$

As is stated by Pao et al. (1984), the equilibrium equation for the static undeformed case in the natural coordinates can be expressed as:

$$\frac{\partial}{\partial \xi_\beta}[T^i_{\beta\gamma}(\delta_{\alpha\gamma} + \frac{\partial u^i_\alpha}{\partial \xi_\gamma})] = 0 \tag{4.25}$$

The equation of motion for the final state can be written as:

$$\frac{\partial}{\partial \xi_\beta}[T^f_{\beta\gamma}(\delta_{\alpha\gamma} + \frac{\partial u^f_\alpha}{\partial \xi_\gamma})] = \rho_0 \frac{\partial^2 u^f_\alpha}{\partial t^2} \tag{4.26}$$

Subtracting the two equations (Eq. 4.25 and Eq. 4.26) and omitting the small term $T_{\beta\gamma}\frac{\partial u_\alpha}{\partial \xi_\gamma}$, yields:

$$\frac{\partial}{\partial \xi_\beta}[T_{\alpha\beta} + T^i_{\beta\gamma}\frac{\partial u_\alpha}{\partial \xi_\gamma} + T_{\beta\gamma}\frac{\partial u^i_\alpha}{\partial \xi_\gamma}] = \rho_0 \frac{\partial^2 u_\alpha}{\partial t^2} \tag{4.27}$$

Eq. 4.27 describes the equation of motion for incremental displacement in natural coordinates.

Considering the stress-strain relationship given in Eq. 4.19, the relationship for the initial and final status can be shown to be:

$$T^i_{\alpha\beta} = C_{\alpha\beta\gamma\delta}E^i_{\gamma\delta} + \frac{1}{2}C_{\alpha\beta\gamma\delta\epsilon\eta}E^i_{\gamma\delta}E^i_{\epsilon\eta} \tag{4.28}$$

and

$$T^f_{\alpha\beta} = C_{\alpha\beta\gamma\delta}E^f_{\gamma\delta} + \frac{1}{2}C_{\alpha\beta\gamma\delta\epsilon\eta}E^f_{\gamma\delta}E^f_{\epsilon\eta} \tag{4.29}$$

Subtracting $T^f_{\alpha\beta}$ from $T^i_{\alpha\beta}$, yields:

$$\begin{aligned} T_{\alpha\beta} &= T^f_{\alpha\beta} - T^i_{\alpha\beta} \\ &= C_{\alpha\beta\gamma\delta}E^f_{\gamma\delta} + \frac{1}{2}C_{\alpha\beta\gamma\delta\epsilon\eta}E^f_{\gamma\delta}E^f_{\epsilon\eta} - (C_{\alpha\beta\gamma\delta}E^i_{\gamma\delta} + \frac{1}{2}C_{\alpha\beta\gamma\delta\epsilon\eta}E^i_{\gamma\delta}E^i_{\epsilon\eta}) \\ &= C_{\alpha\beta\gamma\delta}E_{\gamma\delta} + \frac{1}{2}C_{\alpha\beta\gamma\delta\epsilon\eta}(E^i_{\gamma\delta}E_{\epsilon\eta} + E_{\gamma\delta}E^i_{\epsilon\eta} + E_{\gamma\delta}E_{\epsilon\eta}) \\ &= C_{\alpha\beta\gamma\delta}E_{\gamma\delta} + C_{\alpha\beta\gamma\delta\epsilon\eta}(E^i_{\gamma\delta}E_{\epsilon\eta} + \frac{1}{2}E_{\gamma\delta}E_{\epsilon\eta}) \end{aligned} \tag{4.30}$$

For Eq. 4.30, the $\frac{1}{2}E_{\gamma\delta}E_{\epsilon\eta}$ term can be ignored because it is the product of two small quantities. The Cauchy strain tensors can be used instead of the Lagrangian strain tensors for the first term in the bracket, considering the consistency with the strain energy function (Pao et al., 1984; Gandhi, 2010), yielding:

$$T_{\alpha\beta} = C_{\alpha\beta\gamma\delta}E_{\gamma\delta} + C_{\alpha\beta\gamma\delta\epsilon\eta}e^i_{\gamma\delta}e_{\epsilon\eta} \tag{4.31}$$

Where

$$e_{\alpha\beta} = \frac{1}{2}[\frac{\partial u_\alpha}{\partial \xi_\beta} + \frac{\partial u_\beta}{\partial \xi_\alpha}]$$
$$e^i_{\alpha\beta} = \frac{1}{2}[\frac{\partial u^i_\alpha}{\partial \xi_\beta} + \frac{\partial u^i_\beta}{\partial \xi_\alpha}] \tag{4.32}$$

Substituting the stress-strain relationship of Eq. 4.32 to the Eq. 4.27, yields (Gandhi, 2010):

$$A_{\alpha\beta\gamma\delta}\frac{\partial^2 u_\gamma}{\partial \xi_\beta \partial \xi_\delta} = \rho_0 \frac{\partial^2 u_\alpha}{\partial t^2} \tag{4.33}$$

Where $A_{\alpha\beta\gamma\delta} = T^i_{\beta\gamma}\delta_{\alpha\gamma} + C_{\alpha\beta\gamma\delta} + C_{\alpha\beta\rho\delta}\frac{\partial u^i_\gamma}{\partial \xi\rho} + C_{\rho\beta\gamma\delta}\frac{\partial u^i_\alpha}{\partial \xi\rho} + C_{\alpha\beta\gamma\delta\epsilon\eta}e^i_{\epsilon\eta}$

This equation describes wave propagation in stressed media.

4.4 Acoustoelastic constants for biaxial stressed media

Eq. 4.33 describes wave propagation in stressed media, and the parameter $A_{\alpha\beta\gamma\delta}$ refers to the different value corresponding to different stress configurations. This section provides values for the parameter $A_{\alpha\beta\gamma\delta}$ for the biaxial stress status media, following the work by Gandhi (2010).

4.4.1 Acoustoelastic constants for biaxial stress status media

For thin plate materials with small predeformations, Eq. 4.31 can be simplified as:

$$T^i_{ij} = C_{ijkl}e^i_{kl} \tag{4.34}$$

Substituting the parameter $A_{\alpha\beta\gamma\delta}$ given by Eq. 4.33 into Eq. 4.34 yields:

$$A_{\alpha\beta\gamma\delta} = C_{\beta\delta\lambda\rho} + C_{\alpha\beta\gamma\delta} + C_{\alpha\beta\rho\delta}\frac{\partial u^i_\gamma}{\partial \xi\rho} + C_{\rho\beta\gamma\delta}\frac{\partial u^i_\alpha}{\partial \xi\rho} + C_{\alpha\beta\gamma\delta\epsilon\eta}e^i_{\epsilon\eta} \tag{4.35}$$

For the biaxial stress σ_{11} along the ξ_1 direction and σ_{22} along the ξ_2 direction, the stress tensor in the natural system can be written as:

$$T^i_{\alpha\beta} = \begin{bmatrix} \sigma_{11} & 0 & 0 \\ 0 & \sigma_{22} & 0 \\ 0 & 0 & 0 \end{bmatrix} \tag{4.36}$$

The stiffness matrix for orthogonal an-isotropic material can be written as:

$$C = \begin{bmatrix} C_{11} & C_{12} & C_{13} & 0 & 0 & 0 \\ C_{21} & C_{22} & C_{23} & 0 & 0 & 0 \\ C_{31} & C_{32} & C_{33} & 0 & 0 & 0 \\ 0 & 0 & 0 & C_{44} & 0 & 0 \\ 0 & 0 & 0 & 0 & C_{55} & 0 \\ 0 & 0 & 0 & 0 & 0 & C_{66} \end{bmatrix} \tag{4.37}$$

Considering the stress vs. strain relationship in the natural system, substituting Eq. 4.36 into Eq. 4.37, yields:

$$\begin{bmatrix} \sigma_{11} \\ \sigma_{22} \\ 0 \\ 0 \\ 0 \\ 0 \end{bmatrix} = \begin{bmatrix} C_{11} & C_{12} & C_{13} & 0 & 0 & 0 \\ C_{21} & C_{22} & C_{23} & 0 & 0 & 0 \\ C_{31} & C_{32} & C_{33} & 0 & 0 & 0 \\ 0 & 0 & 0 & C_{44} & 0 & 0 \\ 0 & 0 & 0 & 0 & C_{55} & 0 \\ 0 & 0 & 0 & 0 & 0 & C_{66} \end{bmatrix} \begin{bmatrix} e_1^i \\ e_2^i \\ e_3^i \\ e_4^i \\ e_5^i \\ e_6^i \end{bmatrix} \tag{4.38}$$

Considering the relationship between the second order elastic constants (μ and λ) and the stiffness constants C_{ijkl}, the relationship between the third order elastic constants (l, m and n) and the stiffness constants C_{ijkl} gives:

$$C_{\alpha\beta\gamma\delta} = \lambda\delta_{\alpha\beta}\delta_{\beta\gamma} + \mu(\delta_{\alpha\gamma}\delta_{\beta\delta} + \delta_{\alpha\delta}\delta_{\beta\gamma}) \tag{4.39}$$

and

$$\begin{aligned} C_{\alpha\beta\gamma\delta\epsilon\eta} = 2(l - m + \frac{n}{2})\delta_{\alpha\beta}\delta_{\gamma\delta}\delta_{\epsilon\eta} + 2(m - \frac{n}{2})(\delta_{\alpha\beta}I_{\gamma\delta\epsilon\eta} + \delta_{\gamma\delta}I_{\epsilon\eta\gamma\delta} + \delta_{\epsilon\eta}I_{\alpha\beta\gamma\delta}) \\ + \frac{n}{2}(\delta_{\alpha\gamma}I_{\beta\gamma\epsilon\eta} + \delta_{\alpha\delta}I_{\beta\gamma\epsilon\eta} + \delta_{\beta\gamma}I_{\alpha\delta\epsilon\eta} + \delta_{\beta\delta}I_{\alpha\gamma\epsilon\eta}) \end{aligned} \tag{4.40}$$

Where

$$I_{\alpha\beta\gamma\delta} = \frac{(\delta_{\alpha\gamma}\delta_{\beta\delta} + \delta_{\alpha\delta}\delta_{\beta\gamma})}{2} \tag{4.41}$$

Based on the relationships given as Eq. 4.38 to Eq. 4.41 , the parameter of $A_{\alpha\beta\gamma\delta}$ can be obtained, which can be written as:

$$A_{\alpha\beta\gamma\delta} = C_{\beta\delta\lambda\rho} + C_{\alpha\beta\gamma\delta} + C_{\alpha\beta\rho\delta}e^i_{\gamma\rho} + C_{\rho\beta\gamma\delta}e^i_{\alpha\rho} + C_{\alpha\beta\gamma\delta\epsilon\eta}e^i_{\epsilon\eta} \tag{4.42}$$

4.4.2 Acoustoelastic constants for the stress-strain relationship

Considering the stress-strain relationship given in Eq. 4.19, the stress-strain relationship in the initial state can be written as:

$$T^i_{\alpha\beta} = C_{\alpha\beta\gamma\delta}E^i_{\gamma\delta} + \frac{1}{2}C_{\alpha\beta\gamma\delta\epsilon\eta}E^i_{\gamma\delta}E^i_{\epsilon\eta} \tag{4.43}$$

$$T^j_{\alpha\beta} = C_{\alpha\beta\gamma\delta}E^j_{\gamma\delta} + \frac{1}{2}C_{\alpha\beta\gamma\delta\epsilon\eta}E^j_{\gamma\delta}E^j_{\epsilon\eta} \tag{4.44}$$

Incremental stress can then be obtained by subtracting the initial stress from the final stress:

$$T_{\alpha\beta} = T^f_{\alpha\beta} - T^i_{\alpha\beta} = C_{\alpha\beta\gamma\delta}E_{\gamma\delta} + C_{\alpha\beta\gamma\delta\epsilon\eta}e^i_{\gamma\delta}e_{\epsilon\eta} \tag{4.45}$$

Where $e_{\epsilon\eta}$ and $e^i_{\gamma\delta}$ are the infinitesimal strain tensors, which are used to substitute for the Lagrangian strain tensor to consist with the strain energy function (Gandhi, 2010).

Substituting Eq. 4.24 into Eq. 4.45, yields (Gandhi, 2010):

$$T_{\alpha\beta} = B_{\alpha\beta\gamma\delta}\frac{\partial u_r}{\partial \xi_\delta} \tag{4.46}$$

Where $B_{\alpha\beta\gamma\delta} = (C_{\alpha\beta\gamma\delta} + C_{\alpha\beta\gamma\delta}e^i_{\gamma\lambda} + C_{\alpha\beta\gamma\delta\epsilon\eta}e^i_{\epsilon\eta})$

4.5 Dispersion relationship under biaxial initial stress

Considering the equation of motion under stress (Eq. 4.33) and the relationship between stress and strain under stress (Eq. 4.46), the dispersion relationship can be obtained under biaxial initial stress.

Supposing the general solution for Eq. 4.33 to be:

$$u_j = U_j e^{i\xi(x_1 + \alpha x_3 - ct)} \tag{4.47}$$

The solution procedures are similar to those for isotropic and anisotropic plates (Appendix C). Substituting Eq. 4.47 into the equation of motion Eq. 4.33, yields the Christoffel equation:

$$K_{mn}(\alpha)U_n = 0, \tag{4.48}$$

Where

$$\begin{aligned}
K_{11} &= c^2\rho^0 - A_{1111} - \alpha^2 A_{1313} \\
K_{12} &= -A_{1112} - \alpha^2 A_{1323} \\
K_{13} &= -\alpha(A_{1133} + A_{1331}) \\
K_{21} &= -A_{1112} - \alpha^2 A_{1323} \\
K_{22} &= c^2\rho^0 - A_{1212} - \alpha^2 A_{2323} \\
K_{23} &= -\alpha(A_{1233} + A_{1332}) \\
K_{31} &= -\alpha(A_{1133} + A_{1331}) \\
K_{32} &= -\alpha(A_{1233} + A_{1332}) \\
K_{33} &= c^2\rho^0 - A_{1313} - \alpha^2 A_{3333}
\end{aligned} \tag{4.49}$$

K_{mn} should go to zero for non-trivial solutions and this will lead to a equation for α:

$$P_6\alpha^6 + P_4\alpha^4 + P_2\alpha^2 + P_0 = 0 \tag{4.50}$$

The expression of stress and displacement can be written as:

$$\begin{aligned}
\{u_1, u_2, u_3\} &= \sum_{q=1}^{6} \{1, V(\alpha_q), W(\alpha_q)\} U_{1q} e^{i\xi(x_1 + \alpha_q x_3 - ct)}, \\
\{\sigma_{33}, \sigma_{23}, \sigma_{13}\} &= \sum_{q=1}^{6} i\xi \{D_{1q}, D_{2q}, D_{3q}\} U_{1q} e^{i\xi(x_1 + \alpha_q x_3 - ct)}
\end{aligned} \tag{4.51}$$

Where

$$\begin{aligned}
V_q(\alpha_q) &= \frac{K_{11}(\alpha_q)K_{23}(\alpha_q) - K_{13}(\alpha_q)K_{12}(\alpha_q)}{K_{13}(\alpha_q)K_{22}(\alpha_q) - K_{12}(\alpha_q)K_{23}(\alpha_q)} \\
W_q(\alpha_q) &= \frac{K_{11}(\alpha_q)K_{23}(\alpha_q) - K_{13}(\alpha_q)K_{12}(\alpha_q)}{K_{33}(\alpha_q)K_{23}(\alpha_q) - K_{13}(\alpha_q)K_{23}(\alpha_q)}
\end{aligned} \tag{4.52}$$

and

$$\begin{aligned} D_{1q} &= B_{3311} + B_{3312}V_q + \alpha_q B_{3333}W_q \\ D_{2q} &= \alpha(B_{1313} + B_{1323}V_q) + B_{1331}W_q \\ D_{3q} &= \alpha(B_{1323} + B_{2323}V_q) + B_{1332}W_q \end{aligned} \tag{4.53}$$

Applying free boundary conditions $\sigma_{13} = \sigma_{23} = \sigma_{33} = 0$ to the expression for σ_{13}, σ_{23} and σ_{33} at the boundaries $x_3 = \pm\frac{d}{2}$ will result in six equations that yield the displacement amplitudes $U_{11}, U_{12}, \cdot, U_{16}$. For the nontrivial solutions the determination of coefficients should go to zero:

$$\begin{bmatrix} D_{11}E_1 & D_{12}E_2 & D_{13}E_3 & D_{14}E_4 & D_{15}E_5 & D_{16}E_6 \\ D_{21}E_1 & D_{22}E_2 & D_{23}E_3 & D_{24}E_4 & D_{25}E_5 & D_{26}E_6 \\ D_{31}E_1 & D_{32}E_2 & D_{33}E_3 & D_{34}E_4 & D_{35}E_5 & D_{36}E_6 \\ D_{11}\tilde{E}_1 & D_{12}\tilde{E}_2 & D_{13}\tilde{E}_3 & D_{14}\tilde{E}_4 & D_{15}\tilde{E}_5 & D_{16}\tilde{E}_6 \\ D_{21}\tilde{E}_1 & D_{22}\tilde{E}_2 & D_{23}\tilde{E}_3 & D_{24}\tilde{E}_4 & D_{25}\tilde{E}_5 & D_{26}\tilde{E}_6 \\ D_{31}\tilde{E}_1 & D_{32}\tilde{E}_2 & D_{33}\tilde{E}_3 & D_{34}\tilde{E}_4 & D_{35}\tilde{E}_5 & D_{36}\tilde{E}_6 \end{bmatrix} = 0 \tag{4.54}$$

Where $E_q = e^{i\xi\alpha_q d/2}$ and $\tilde{E}_q = e^{-i\xi\alpha_q d/2}$.

Solving Eq. 4.54, the dispersion relationships for a biaxial stressed plate can be obtained. Simplifying Eq. 4.54, which can lead to two separate equations that describe the symmetric and anti-symmetric modes (Gandhi, 2010):

For symmetric modes:

$$D_{11}G_1 \cot(\gamma\alpha_1) + D_{13}G_3 \cot(\gamma\alpha_3) + D_{15}G_5 \cot(\gamma\alpha_5) = 0 \tag{4.55}$$

For anti-symmetric modes:

$$D_{11}G_1 \tan(\gamma\alpha_1) + D_{13}G_3 \tan(\gamma\alpha_3) + D_{15}G_5 \tan(\gamma\alpha_5) = 0 \tag{4.56}$$

Where

$$G_1 = D_{23}D_{35} - D_{33}D_{25}$$
$$G_3 = D_{31}D_{25} - D_{21}D_{35} \tag{4.57}$$
$$G_5 = D_{21}D_{33} - D_{31}D_{23}$$

4.6 Dispersion relationship under uniaxial initial stress

When uniaxial stress is applied, the expression for the initial stress tensor can be written as:

$$T^i_{\alpha\beta} = \begin{bmatrix} 0 & 0 & 0 \\ 0 & \sigma_{11} & 0 \\ 0 & 0 & 0 \end{bmatrix} \tag{4.58}$$

The stress tensor given in Eq. 4.58 can be applied for the case when the direction of the applied stress and the direction of the velocity are perpendicular, as will be discussed in detail in the next chapter.

The initial stress tensor can also be written as Eq. 4.59, and applied in the circumstance when the direction of the applied stress and the direction of the velocity are parallel, as will be discussed in detail in the next chapter.

$$T^i_{\alpha\beta} = \begin{bmatrix} \sigma_{11} & 0 & 0 \\ 0 & 0 & 0 \\ 0 & 0 & 0 \end{bmatrix} \tag{4.59}$$

Substituting Eq. 4.58 and Eq. 4.59 into Eq. 4.36 and following the steps shown in Sections 4.5 and 4.6, the dispersion relationship under uniaxial stress can be obtained and produce an expression like that of Eq. 4.55 and Eq. 4.56.

4.7 Chapter summary

This chapter shows the progress achieved by establishing the governing equation for the Lamb wave propagating in a stressed plate by considering wave motion equations under loading for bulk waves combined with Lamb waves propagating in the anisotropic plate.

CHAPTER 5. NUMERICAL RESULTS FOR PLATE WITH DIFFERENT UNIAXIAL STRESS

This chapter reports an investigation into Lamb waves, dealing with the phase velocity and group velocity changes with applied stress for the cases when the direction of stress and direction of velocity are perpendicular and parallel. It is shown that, for both perpendicular and parallel cases, the S_1 mode velocity is most sensitive to the effects of the applied stress.

5.1 For the case when the stress and the velocity are perpendicular

This section discusses the configuration when the direction of the applied stress and the direction of the velocity are perpendicular, in which case the expression for initial stress tensor can be written as shown below:

$$T^i_{\alpha\beta} = \begin{bmatrix} 0 & 0 & 0 \\ 0 & \sigma_{11} & 0 \\ 0 & 0 & 0 \end{bmatrix} \tag{5.1}$$

The coordinates used for a thin metal plate under uniaxial applied stress, where the thickness of the plate is h, and the Lamb wave propagates in the x_1 direction while the applied stress is in the x_2 direction, are shown in Fig. 5.1.

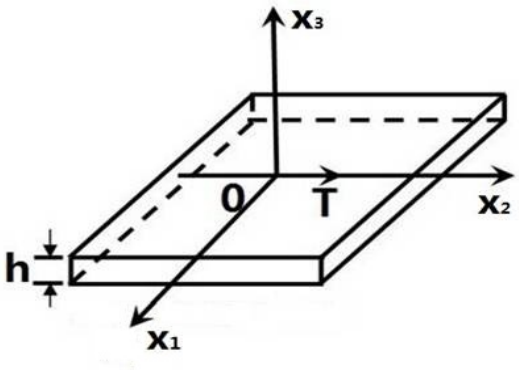

Figure 5.1: Schematic showing coordinates for a thin plate with uniaxial stress.

5.1.1 Dispersion curves under applied stress

The Lamb wave dispersion curves for thin plates under an axial stress can be obtained using MATLAB code based on Eqs. 4.55 and 5.1. The code was validated with calculations using material properties parameters previously reported in the literature (Gandhi et al., 2012), and a 1.0 mm thick aluminum plate was considered. Results considered the case of the aluminum plate with no-loading and when the applied stress is 100 MPa. The material parameters used are shown in Table 5.1.

Table 5.1: Aluminum parameters for calculation [After Gandhi et al.,(2012)]

Parameter	**Value**	**Units**
λ	54.308	GPa
μ	27.174	GPa
l	-281.5	GPa
m	-339.0	GPa
n	-416.0	GPa
ρ_0	2704	km/m^3
v_l	6303	m/s
v_t	3102	m/s
thickness	1	mm

The symmetric modes dispersion curves calculated for the two cases of uniaxial stress and no-load are shown in Fig 5.2. It can be seen that there are small differences between the results for the two cases.

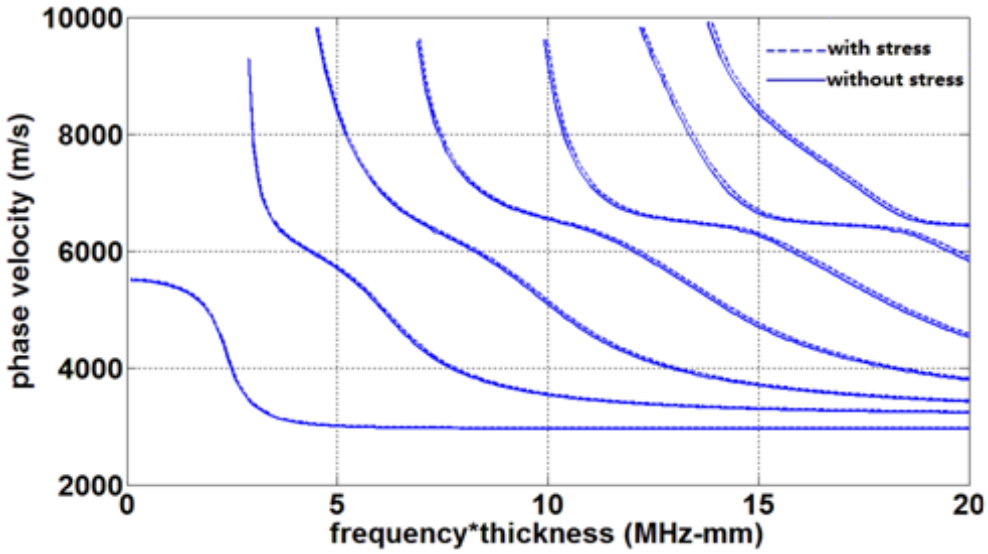

Figure 5.2: Dispersion curve for 1 mm thick aluminum plate without and a 100 MPa uniaxial stress.

5.1.2 Changes of phase velocity under applied stress

Because of the dispersion quality for fundamental and higher order Lamb waves, both phase velocity and group velocity will be discussed here(Pei and Bond, 2016). In this section the phase velocity is discussed, while the group velocity will be considered in a later section.

Validation of the code is provided by comparing the data reported in the literature (Gandhi et al., 2012) with the present calculations which used as many of the same parameters as possible. Here the case considered is to seek the differences for the S_0 mode either with or without stress, and the difference curves are shown in Fig. 5.3. It can be seen that the new data are in good general agreement with that from the literature. Data for higher order modes with load have not been previously published, but the general form of the unloaded curves are in good agreement with published data.

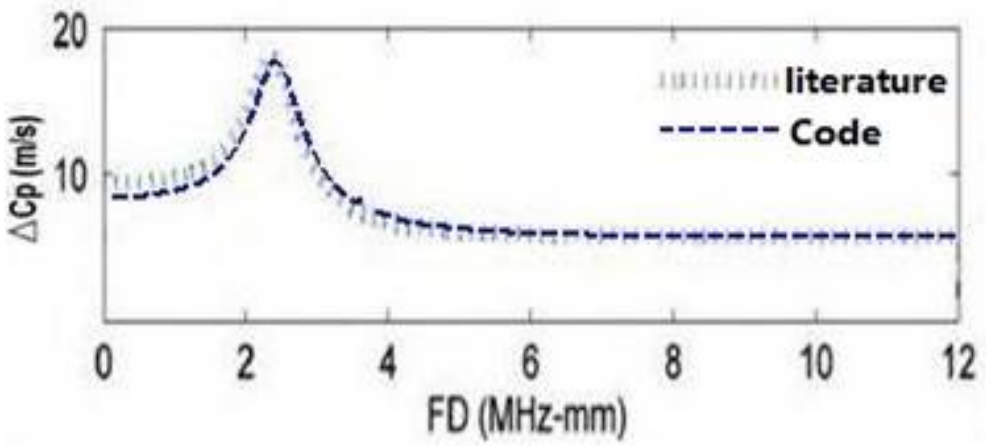

Figure 5.3: The difference in velocity for the S_0 mode with and without stress, comparing (i) given in the literature (Gandhi, et al., 2012) with (ii) results obtained using the new code.

The analysis was then extended to consider the effects of stress on higher-order Lamb modes. The differences in velocity between cases of stress and no stress as a function of normalized frequency-thickness for different symmetrical modes are shown in Fig. 5.4. As higher-order modes are considered, the cut-off frequencies increase, (on the MHz-mm scale), and the difference in the phase velocity decreases. It can also be seen that the S_0 mode is a special case, since when compared to other modes it has a peak rather than an obvious cut-off frequency.

Data for the corresponding cases of the difference in velocity for the cases of stress and no stress, and for different anti-symmetrical modes as a function of frequency, are given in Fig. 5.5.

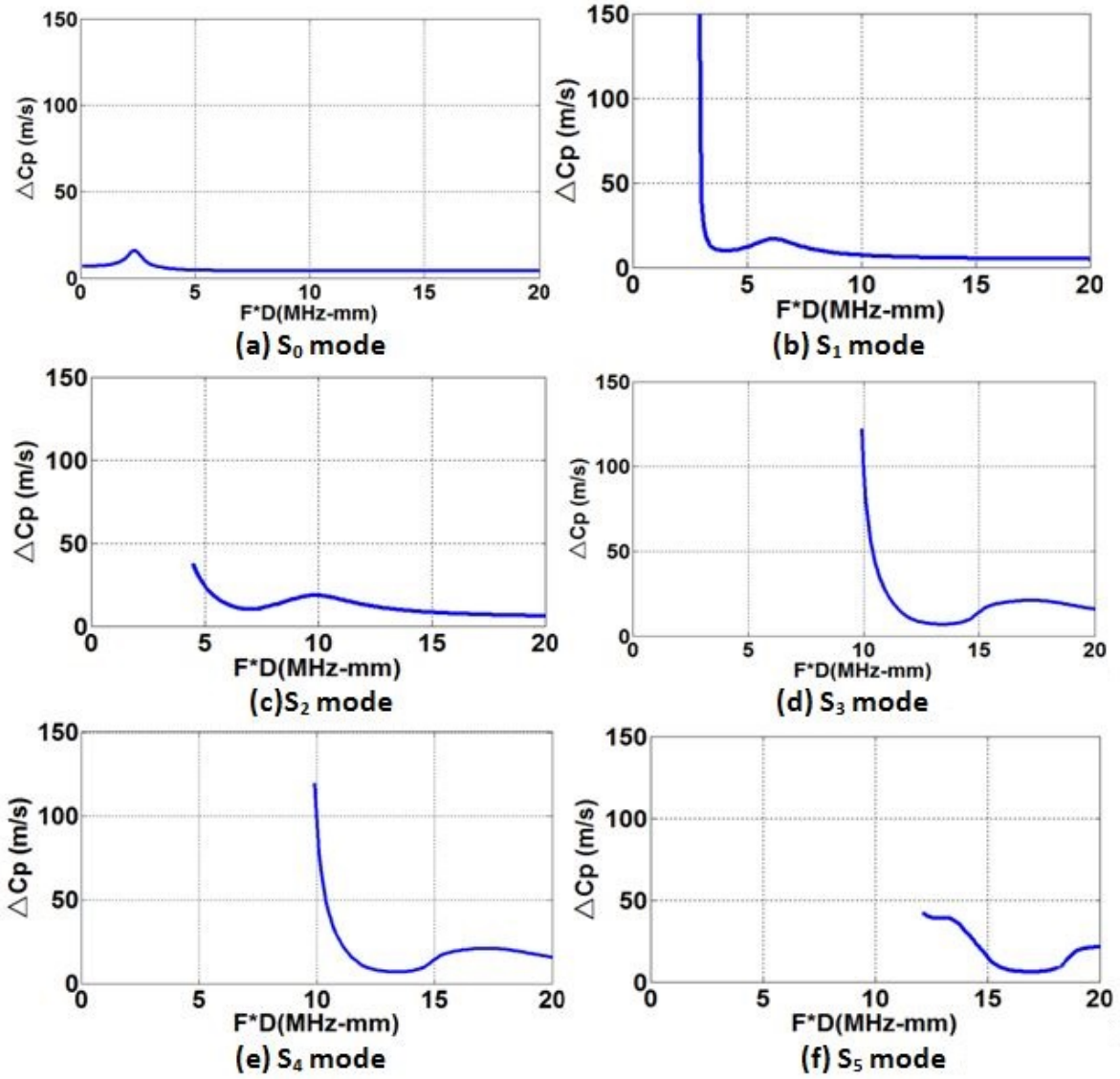

Figure 5.4: Symmetrical mode velocity difference in a 1 mm aluminum plate as a function of frequency, for cases of 100 MPa load and no load.

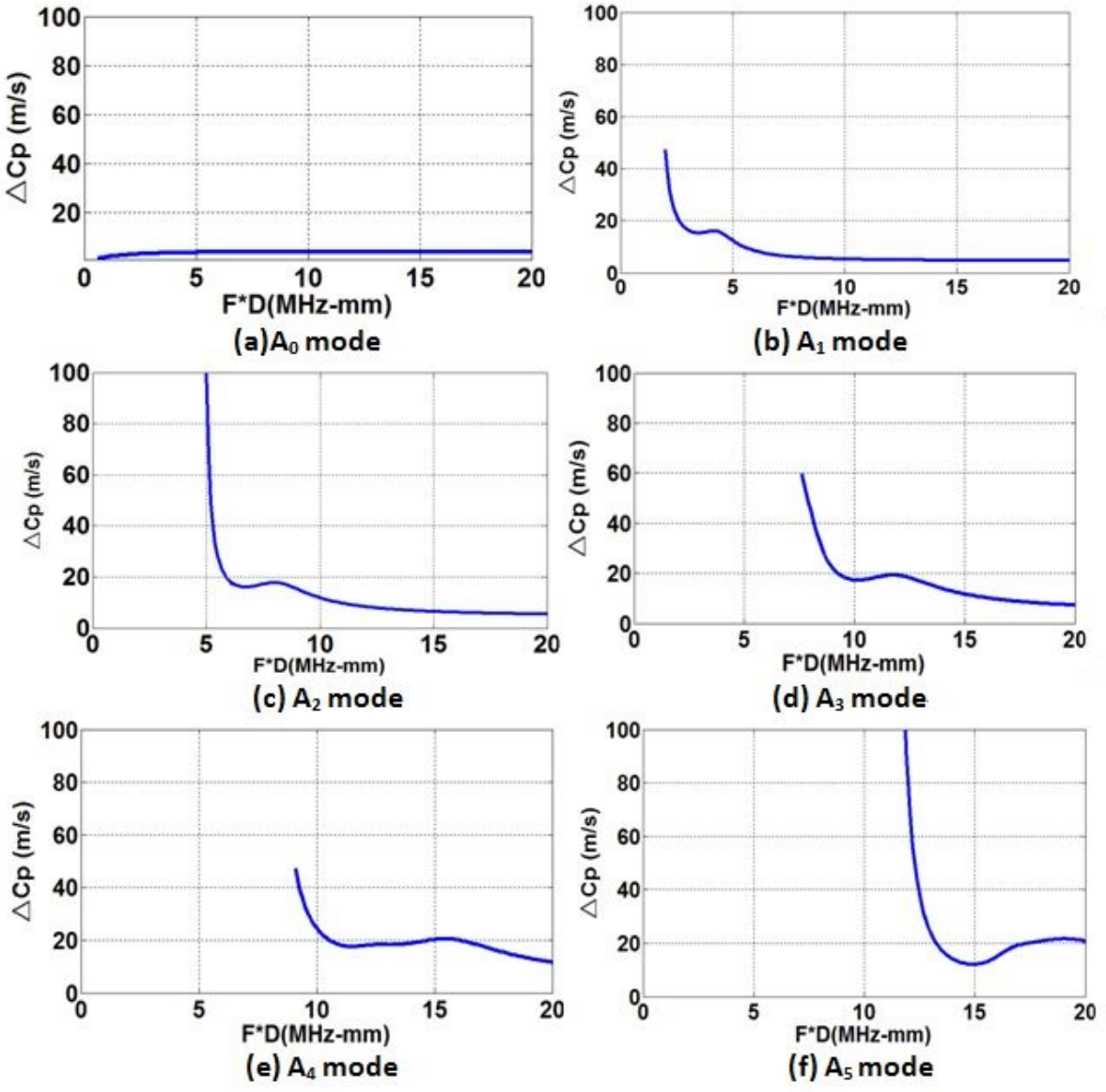

Figure 5.5: Anti-symmetrical mode velocity difference in a 1 mm aluminum plate as a function of frequency, for cases of 100 MPa load and no load.

It can be seen in Fig. 5.5 that, as mode order increases from the A_1 to A_5, the cut-off frequency moves to higher values on the MHz-mm scale. The form of the differences for the A_0 mode is different from that for the other modes in that it has an increasing value starting from zero. The form of this response is the same as for results previously given in the literature (Gandhi et al., 2012).

5.1.3 Changes of group velocity under applied stress

In an experiment it is the group velocity that is measured, so to provide data for comparison with experiment, it is necessary to calculate the group velocity. These data were calculated and the changes seen in the group velocity under a 100 MPa uniaxial stress for the cases of the S_0, S_1, A_0 and A_1 modes are shown in Fig. 5.6. From the data it can be seen that the S_1 mode exhibits the largest change under load at lower frequency-thickness values and that this mode appears to have the highest sensitivity to stress.

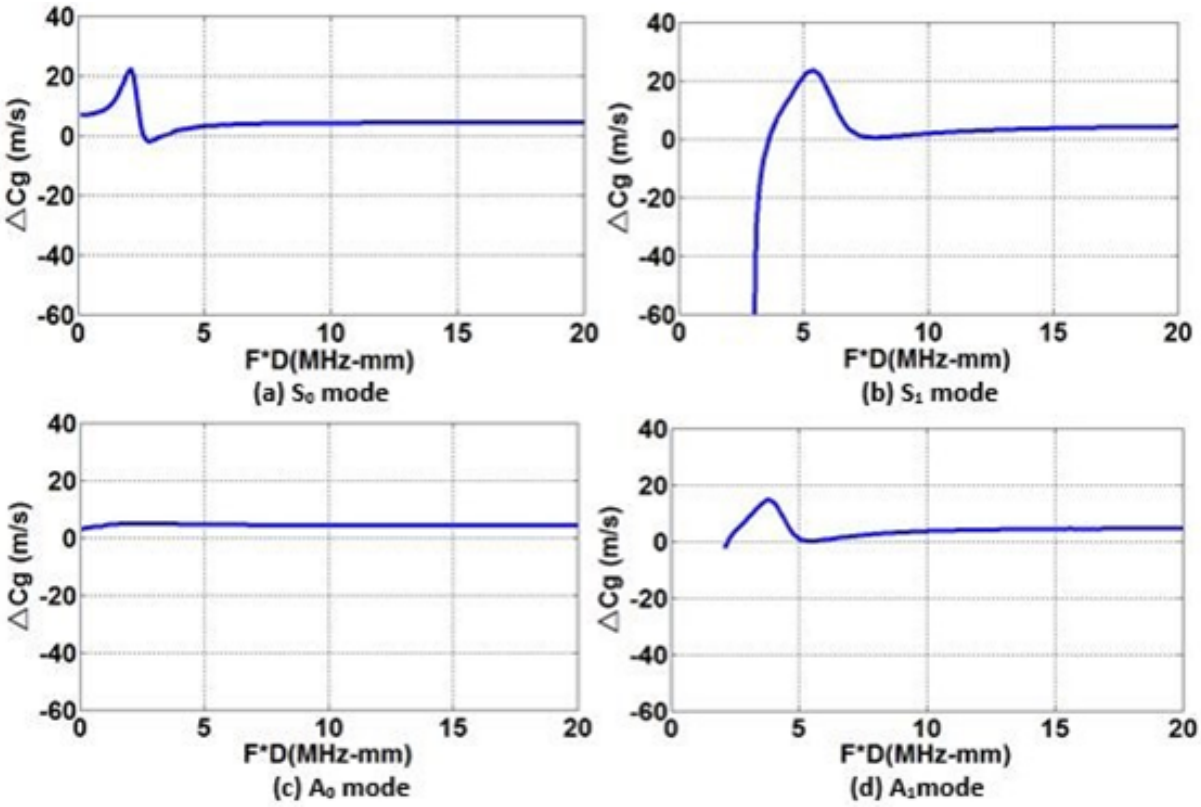

Figure 5.6: The differences in group velocity for the S_0, S_1, A_0 and A_1 modes as a function of frequency, between no-load and with 100 MPa stress applied.

To compare sensitivity to stress for different bulk wave types with Lamb wave modes, the use of velocity normalized in frequency and thickness form at 3.0 MHz-mm was selected. The relative change in velocity with load for the range of strain from 0 to 600 $\mu\varepsilon$ was calculated. The data for the cases of

the S_0, S_1, A_0 and A_1 modes are shown in Fig. 5.7. It can be seen that the relative change in velocity for the S_1 mode Lamb wave is much larger when compared to that for other Lamb modes under the same strain.

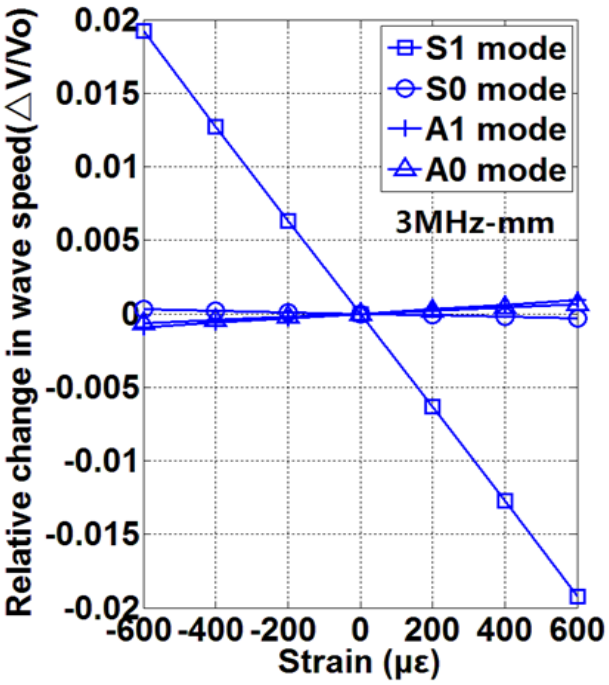

Figure 5.7: The change of group velocity for $S_0, S_1, A_0$and A_1 Lamb modes with strain under and at a normalized thickness frequency combination, 3MHz-mm, in an aluminum plate.

When considering the data shown in Fig. 5.7, the absolute value of the slope gives a measure of velocity change sensitivity for different wave modes and the stress sensitivity coefficient is in units of $\mu\varepsilon^{-1}$. For comparison, the corresponding data for the change of velocity with strain for compressional waves in aluminum (Rossini et al., 2012) and in Steel (Egle and Bray, 1976) are shown in Fig. 5.8. The data in Fig. 5.8 shows that the S_1 mode Lamb wave in aluminum is about 10 times more sensitive to load than for the case of a bulk compressional wave.

The sensitivity is also a function of the frequency-thickness parameter and Fig. 5.9 shows the sensitivity coefficient for the S_1 mode. It is seen that the coefficient value is highest (most sensitive) close to 3.0 MHz-mm, the cut-off frequency, and then decreases sharply as the frequency*thickness parameter increases. It also exhibits a second smaller peak at a value close to twice the cut-off frequency.

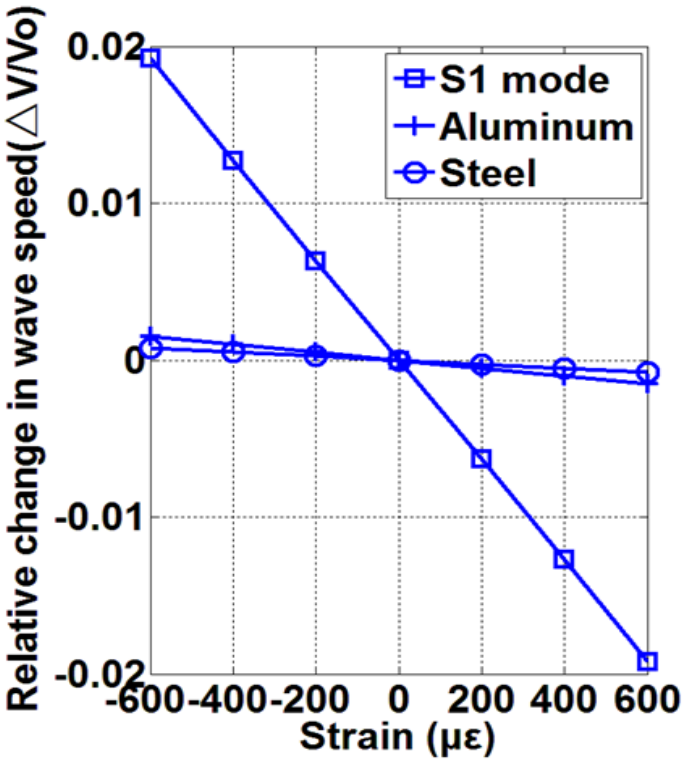

Figure 5.8: The change of velocity with strain of a compressional wave for aluminum and for steel compared with data for the S_1 Lamb mode in aluminum.

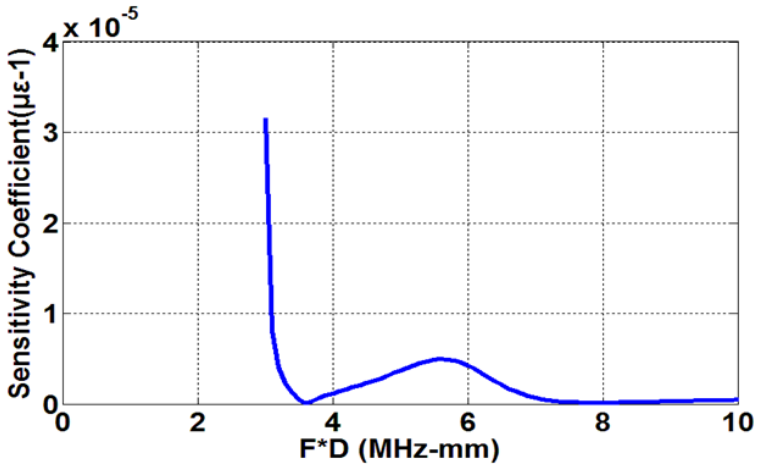

Figure 5.9: Sensitive coefficient for the S_1 Lamb mode in aluminum, as a function of normalized frequency-thickness product.

5.2 For the parallel case

This section discusses the case in which the direction of the stress and the direction of the velocity are parallel. The expression for the initial stress tensor can be written as Eq. 5.2:

$$T^i_{\alpha\beta} = \begin{bmatrix} \sigma_{11} & 0 & 0 \\ 0 & 0 & 0 \\ 0 & 0 & 0 \end{bmatrix} \tag{5.2}$$

The coordinates for a thin plate under parallel stress are shown in Fig. 5.10

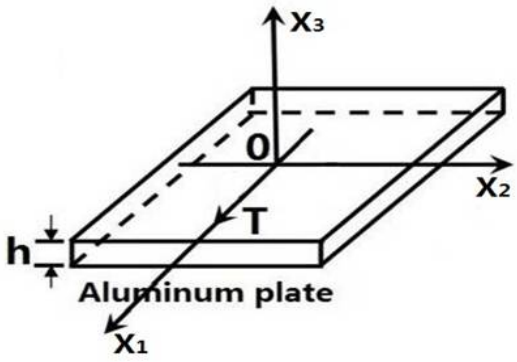

Figure 5.10: Schematic showing coordinates for a thin plate with uniaxial stress.

5.2.1 Dispersion relationship for parallel case

The parameters for the parallel case used here are unchanged, as shown in Table 5.1. The dispersion relationship is shown in Fig. 5.11. The general form is similar as the form in the perpendicular case and for zero stress the results are identical, and it can be seen that there are only small differences between the results for the two cases.

Further validation of the code is provided by considering the difference in velocity for the S_0 mode with and without 100 MPa stress, and by comparing data produced by the new code with that previously reported in the literature (Gandhi et al., 2012). These difference between the two data sets are shown in Fig. 5.12. It can be seen that the new data are in good general agreement with those from the literature.

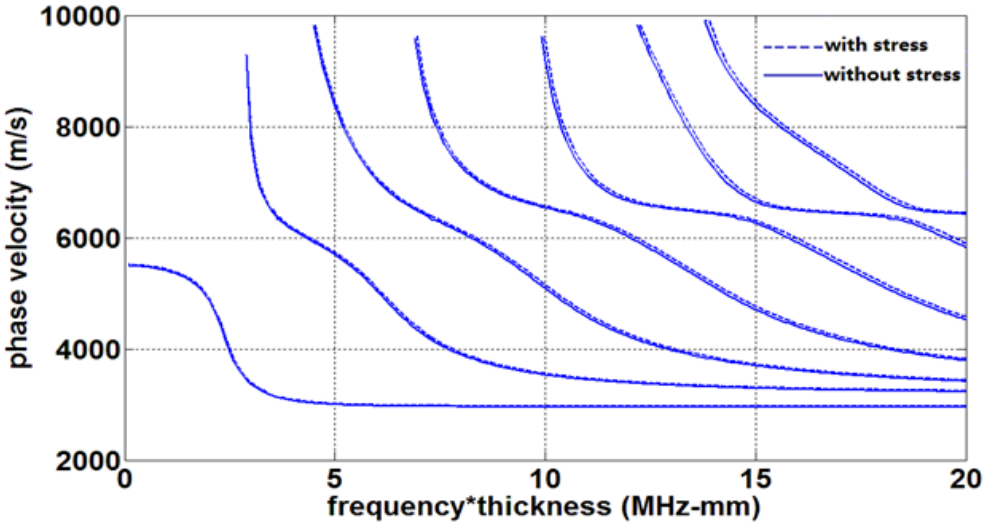

Figure 5.11: Symmetric dispersion curve for 1 mm thick aluminum plate without stress and with a 100 MPa unixaial stress.

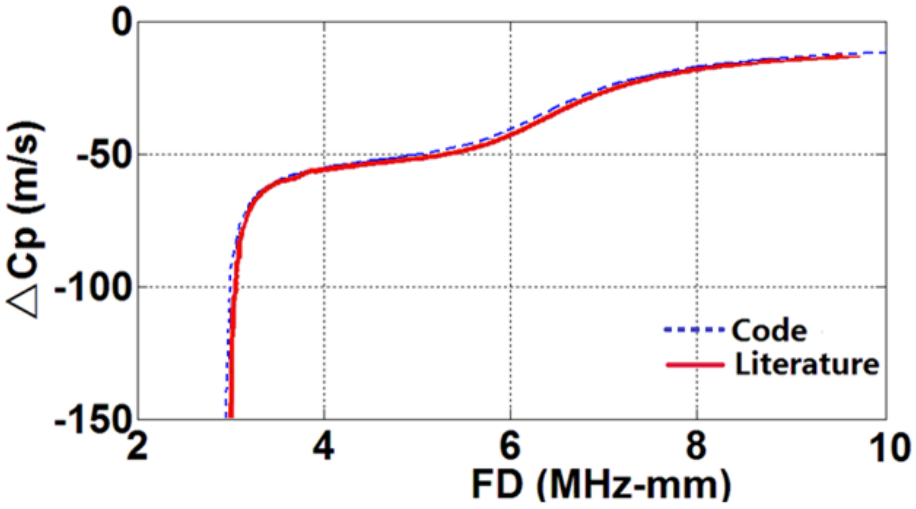

Figure 5.12: The difference in velocity for the S_0 mode with and without stress, with load and measurement axis parallel, comparing (i) that given in the literature (Gandhi, et al., 2012) and (ii) data obtained using the new code.

5.2.2 Changes of phase velocity under applied stress

The analysis was then extended to consider the effects of stress on higher-order Lamb modes. The differences in velocity between cases of stress and no stress as a function of normalized frequency-

thickness for different symmetrical modes is shown in Fig. 5.13. Because higher-order modes are considered, the cut-off frequencies increases (on the MHz-mm scale), and the phase-velocity differences decreases. It can also be seen that the S_0 mode is a special case when compared to other modes, in that it has a peak rather than an obvious cut-off frequency.

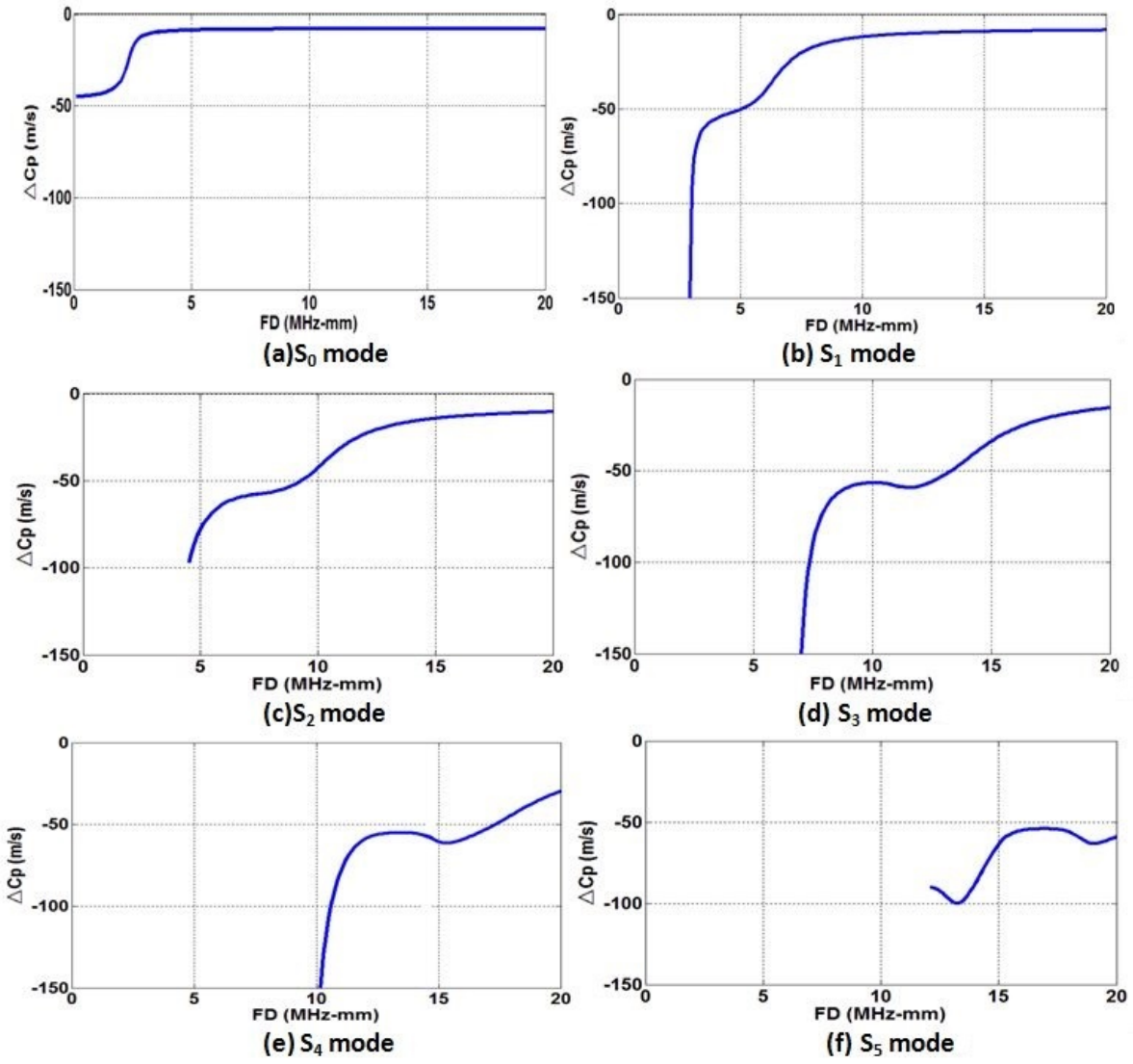

Figure 5.13: Symmetrical mode phase velocity difference in a 1 mm aluminum plate, as a function of normalized frequency-thickness, for 100 MPa's load and no-load cases.

Data for the corresponding cases for the difference in velocity for the cases of stress and no stress for different order anti-symmetrical modes as a function of normalized frequency, are given in Fig. 5.14.

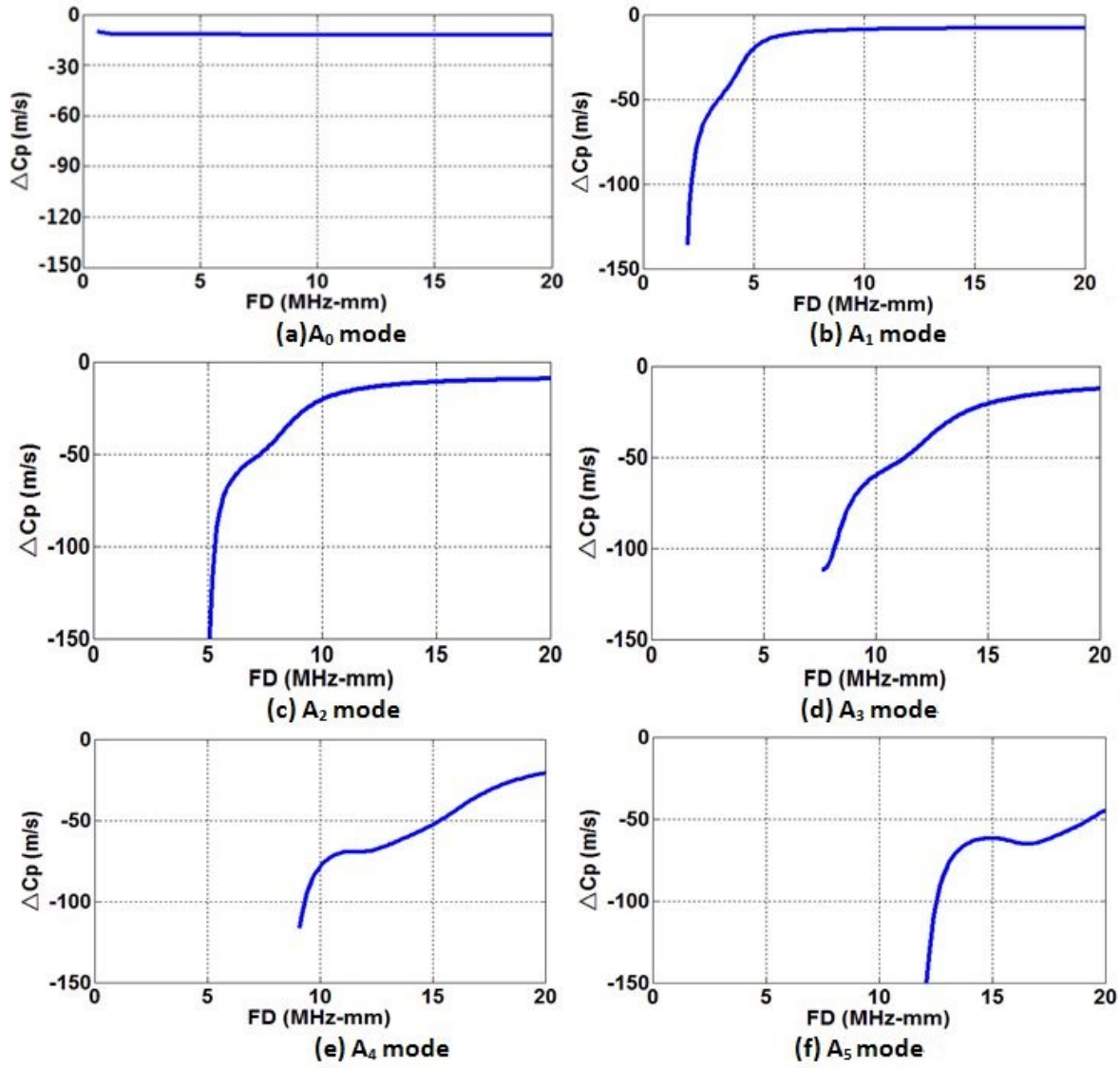

Figure 5.14: Anti-symmetrical mode velocity difference in a 1 mm aluminum plate, as a function of normalized frequency-thickness for 100 MPa's load and no-load cases.

It can be seen in Fig. 5.14 that, as mode order increases from A_1 to A_5, the cut-off frequency moves to higher values on the MHz-mm scale. The form of the differences for the A_0 mode is different from

that for the other modes in that it has an increasing value starting from zero. The form of this response is the same as for results previously given in the literature (Gandhi et al., 2012).

5.2.3 Changes of group velocity under applied stress

Here again the group velocity will be discussed. These data were calculated and the changes seen in the group velocity under a 100 MPa uniaxial stress for the cases of the S_0, S_1, A_0 and A_1 modes are shown in Fig. 5.15. From the data it can be seen that the S_1 mode exhibits the largest change under load at lower frequency-thickness values, and that this mode appears to have the highest sensitivity to stress.

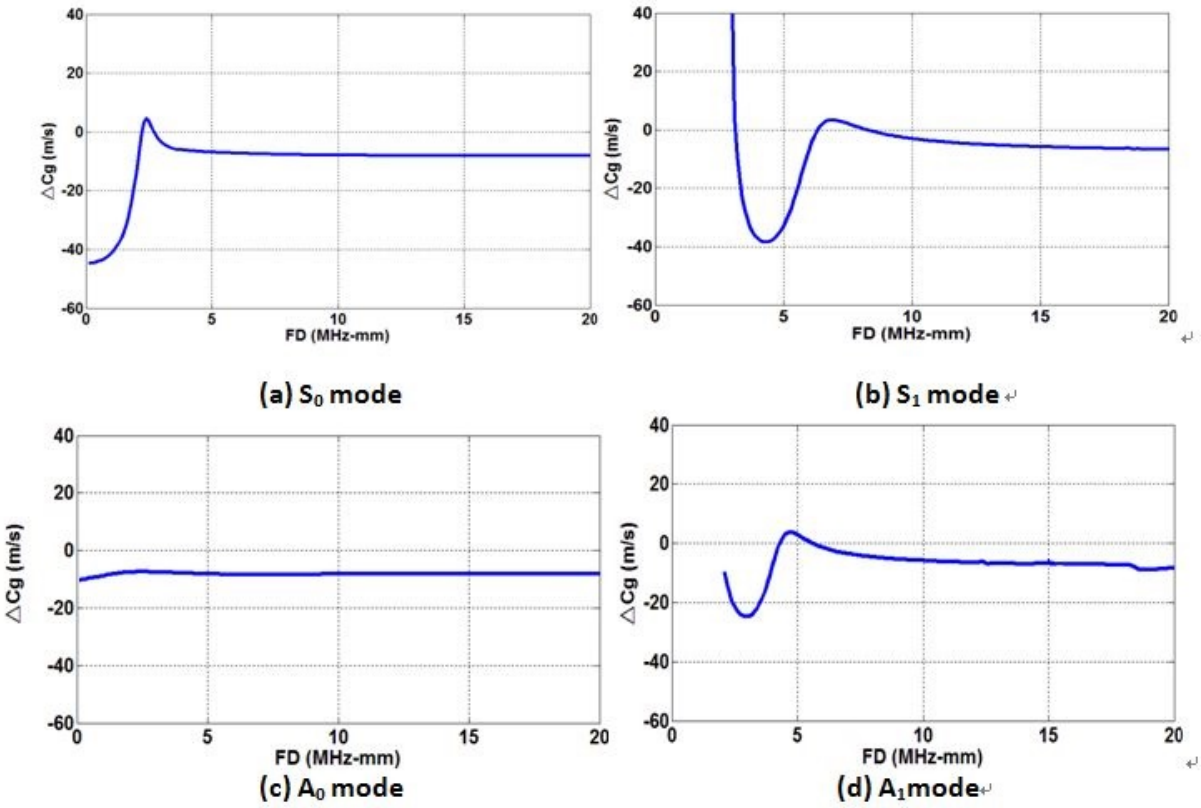

Figure 5.15: The differences in group velocity between no-load and with 100 MPa stress applied for the S_0, S_1, A_0 and A_1 modes as a function of normalized frequency-thickness.

To compare sensitivity to stress for different bulk wave types and Lamb wave modes for a typical case, the use of velocity normalized in a frequency and thickness form at 3.0 MHz-mm for aluminum

was selected. The relative change in velocity with load for the range of strain from 0 to 600 $\mu\varepsilon$ was calculated. The data for the cases of the S_0, S_1, A_0 and A_1 modes are shown in Fig. 5.16, where it can be seen that the relative change of the velocity for the S_1 mode Lamb wave is much larger, when compared to that for other modes under the same strain.

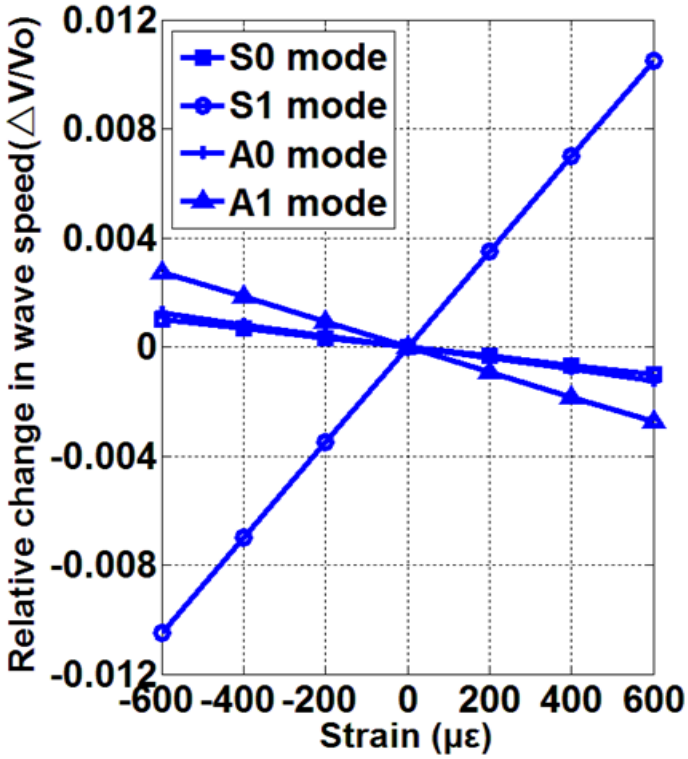

Figure 5.16: The change in group velocity for S_0, S_1, A_0 and A_1 modes with strain under and at a normalized frequency-thickness combination, 3 MHz-mm, in an aluminum plate.

The sensitivity of the S_1 mode is shown in Fig. 5.17 as a function of the normalized frequency-thickness parameter. It can be seen that the coefficient value is highest (most sensitive) close to 3.0 MHz-mm, the cut-off frequency, and it then decreases sharply as the value of the frequency-thickness parameter increases. It does exhibit a second and even a third, but smaller peak, at a value close to that close to a multiple of the cut-off frequency.

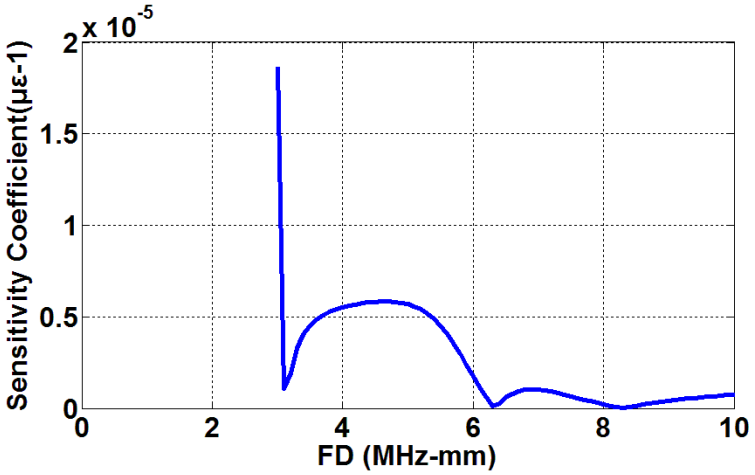

Figure 5.17: Sensitive coefficient for the S_1 mode, as function of normalized frequency-thickness.

5.3 Comparison of Acoustoelastic effect on Lamb wave propagation in stressed plates with different measurement orientations

In section 5.1 and 5.2 the sensitivity of higher Lamb modes to loads was investigated using models in which the load and measurement axis are perpendicular (Configuration A) and when load and measurement axis are parallel (Configuration B) as shown in the following Fig. 5.18. In this section a comparison between these two configurations will be presented.

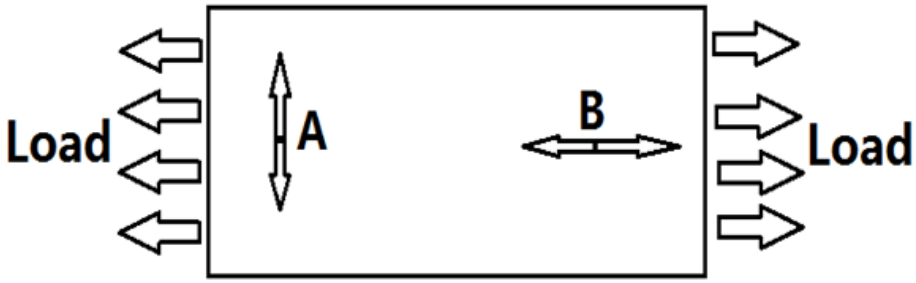

Figure 5.18: Schematic showing load and measurement axes. Configuration A - load and measurement perpendicular, Configuration B - load and measurement parallel.

5.3.1 Comparison of higher order Lamb wave for phase velocity

The data in Fig. 5.19 show that, for the parallel case (B), the velocities increase with loading and the changes in velocity are all positive. In contrast, for the perpendicular case (A), the velocities increase but the changes in velocity are all negative. Although these are the differences, it can be seen that in both cases it is the S_1 mode which changes most.

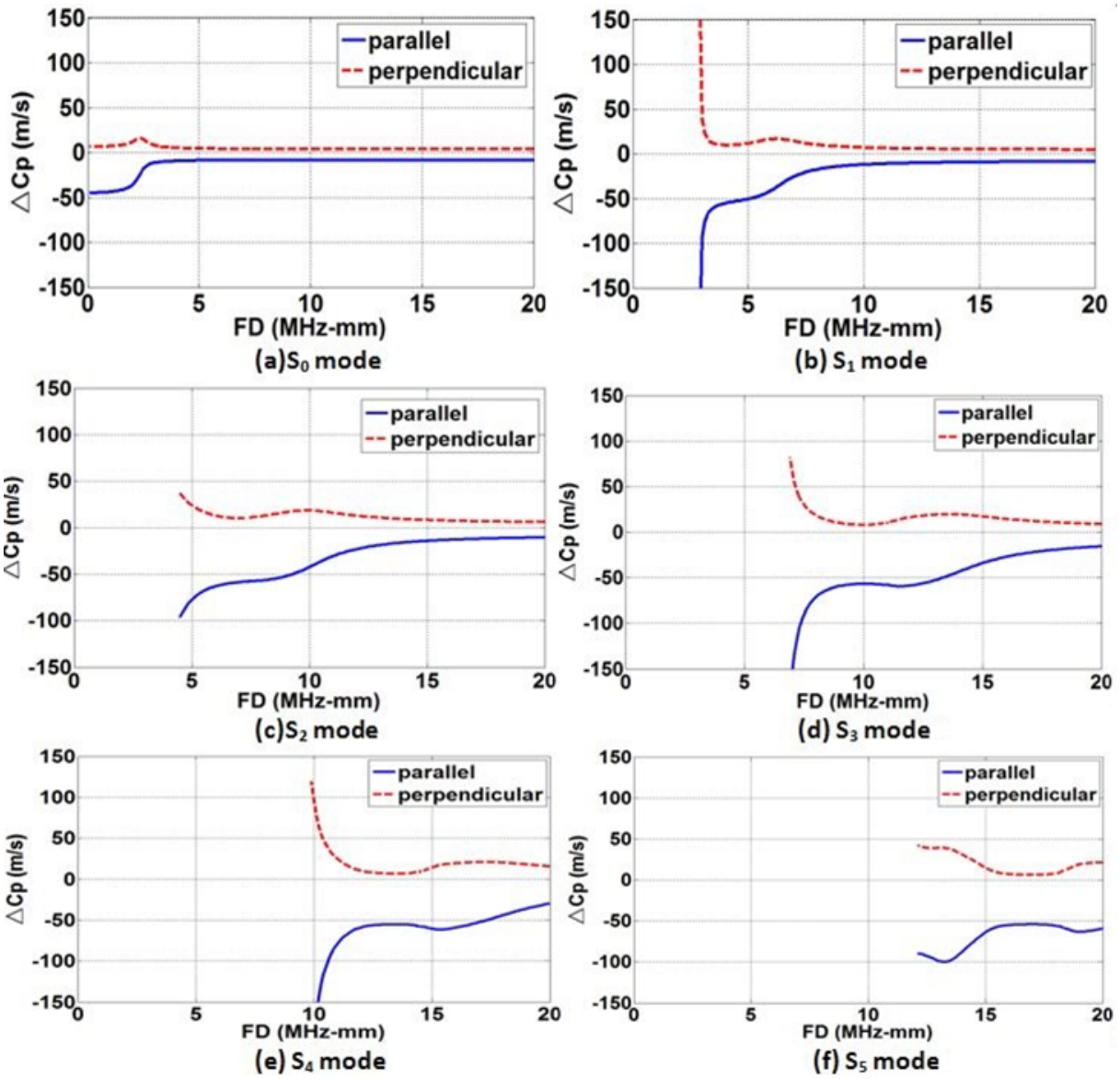

Figure 5.19: Symmetrical mode velocity differences in a 1 mm aluminum plate as a function of frequency-thickness, comparing cases for a 100 MPa load and no-load for the two cases A and B.

Fig. 5.20 shows the corresponding data for the symmetrical phase modes for differences in phase velocity for the cases of 100 MPa stress and no stress for different modes as a function of frequency, for both parallel (B) and perpendicular (A) configurations.

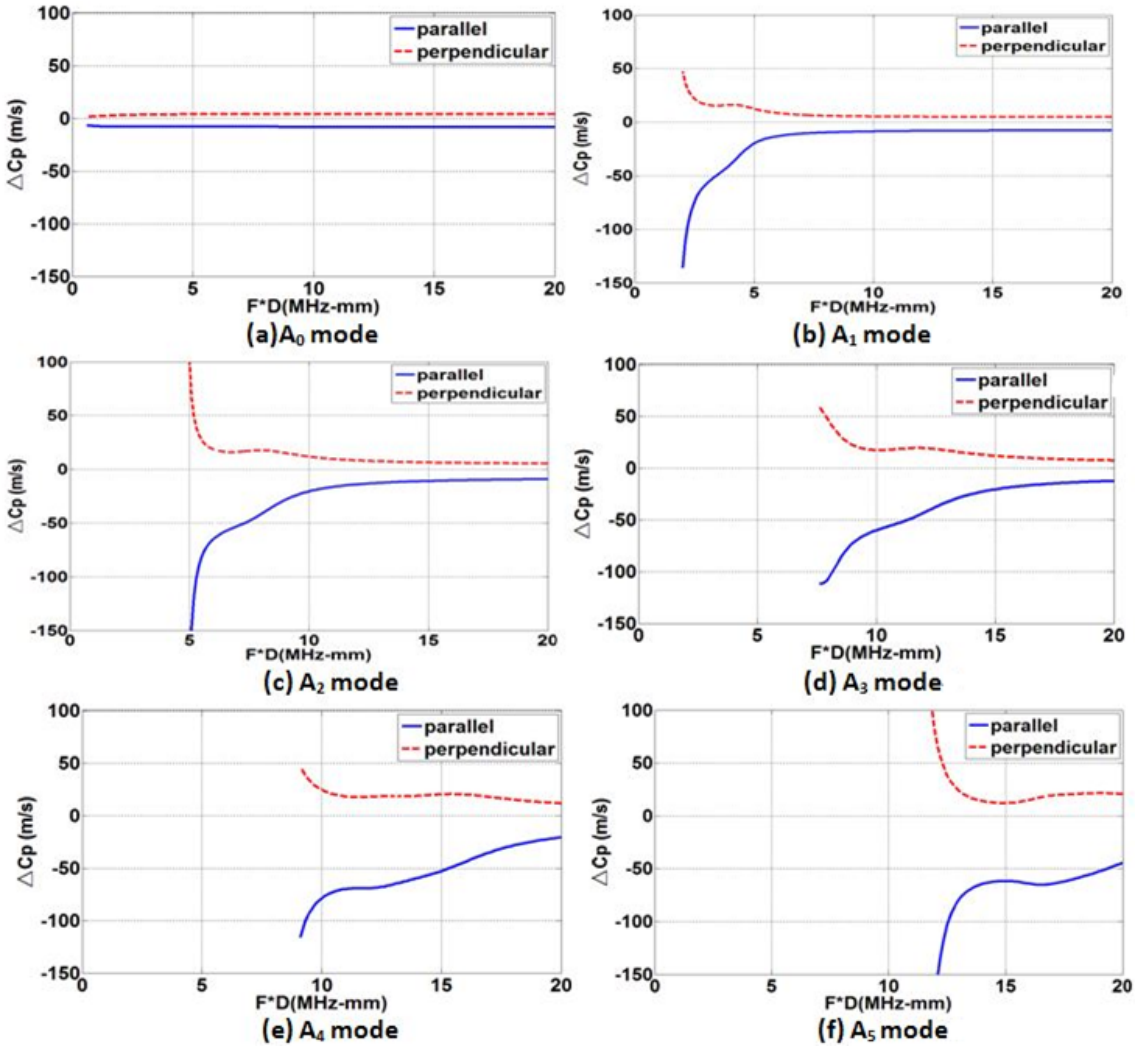

Figure 5.20: Anti-symmetrical mode velocity difference in a 1 mm aluminum plate, as a function of frequency-thickness, comparing cases of a 100 MPa load and no-load, for the measurement cases A and B.

Fig. 5.20 shows the corresponding data for the anti-symmetrical phase modes of the difference in the phase velocity for the cases of 100 MPa stress and no stress for different modes as a function of frequency-thickness, for both parallel (B) and perpendicular (A) cases. It can be seen that, as mode

order increases from A_1 to A_5, the cut-off frequency moves to higher values on the MHz-mm scale. Comparing the parallel with the perpendicular case, it is seen that for the perpendicular case with load added, the velocity increases and the changes in velocity are all positive. In contrast, for the parallel case the velocity increases but the changes in velocity are all negative.

5.3.2 Comparison of higher order Lamb wave for group velocity

Comparison and contrast behavior with respect to group velocity is shown in Fig. 5.21. The data were calculated and the changes can be seen in group velocity under a 100 MPa uniaxial stress for the cases of the S_0, S_1, A_0 and A_1 modes. From the data it can be seen that the S_1 mode exhibits the largest change under load at lower frequency-thickness values and that this mode appears to have the highest sensitivity to stress.

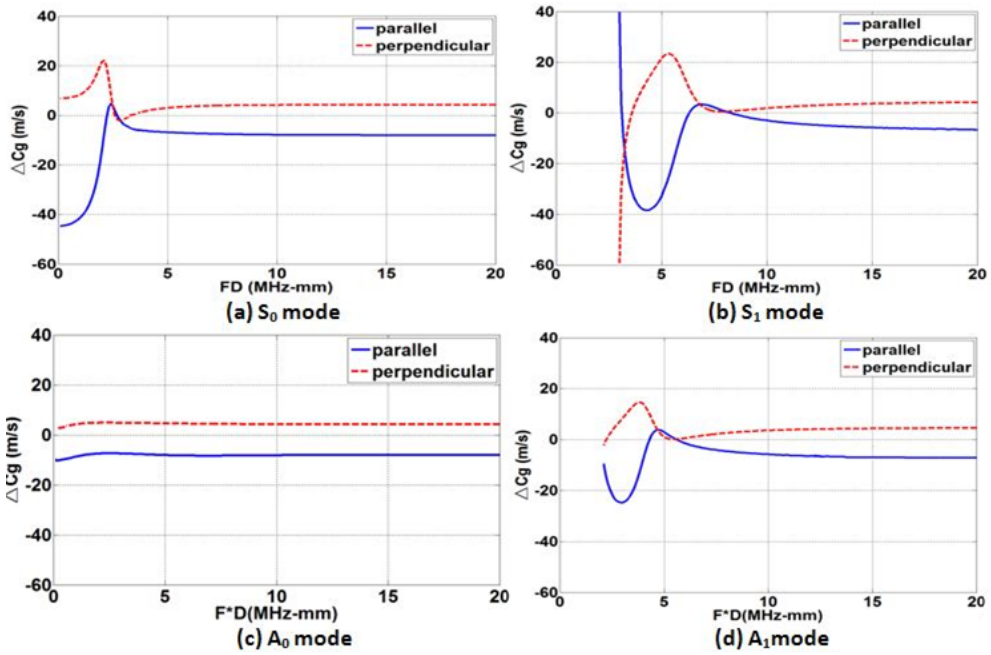

Figure 5.21: The differences in group velocity for the S_0, S_1, A_0 and A_1 modes as a function of frequency-thickness, between no-load and with 100 MPa stress applied for both parallel (B) and perpendicular (A) cases.

The data for the changes in group velocity for the perpendicular (A) and parallel (B) cases are shown in Fig. 5.22. Comparing the data for the parallel and perpendicular cases, it can be seen that in both cases

the S_1 mode group velocity is most sensitive with respect to the effects of stress when compared with the other three modes, and this again is especially true near the cut-off frequency. The difference between the two data sets is that for the perpendicular (A) case the value is negative while for the parallel (B) case the value is positive. To compare the sensitivity of different Lamb modes to load (strain), normalized frequency-thickness was selected at 3.0 MHz-mm (near the cut-off frequency). The relative change in group velocity with strain was calculated for the range from 0 to 600 $\mu\varepsilon$. The sensitivity with respect to aluminum of the S_1 mode for the case of load and measurement axis perpendicular (A) is compared to the case of S_1 mode for the load-measurement axis parallel (B), and the data are compared with the effects for bulk waves in steel (Egle and Bray, 1976) and aluminum (Rossini et al., 2012), the data for which are given in Fig. 5.22. It can be seen that, for the S_1 parallel (B) case, this Lamb mode is about 6 times more sensitive than for a bulk wave, and the S_1 mode for perpendicular (A) is about 10 times more sensitive.

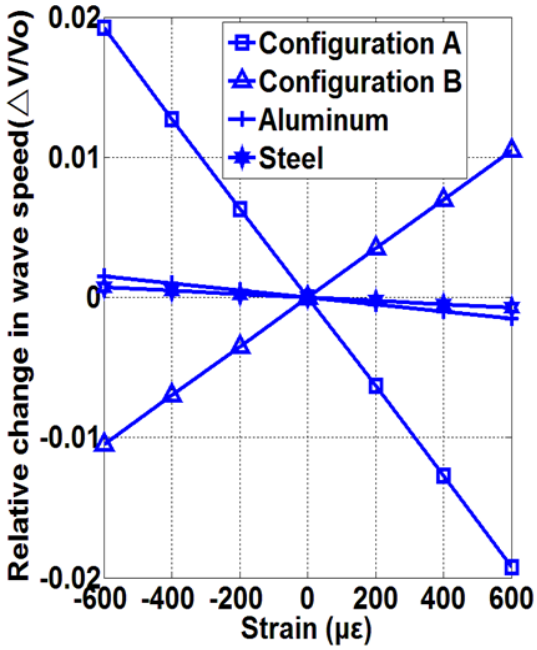

Figure 5.22: The change of velocity with strain for (I) compressional wave for steel (Egle and Bray, 1976), (II) compressional wave for aluminum (Rossini et al., 2012) and (III) S_1 Lamb wave mode in aluminum for parallel and perpendicular load and measurement axis.

5.4 Uncertainty in the numerical calculations for the velocity

Potential sources of errors and uncertainty regarding the numerical calculations was investigated, and the most significant cause of inaccuracy and errors would appear to be the input material parameter values used. The sensitivity to variation in material parameters was investigated by repeating calculations when changing values of one parameter by 5% or 1%; the effect of these changes on relative change in velocity are tabulated in Table 5.2.

Table 5.2: Influence of aluminum parameters for calculation

Parameter	**Value Change 5 %**	**Value Change 1 %**
λ	42.44%	12.75%
μ	54.26%	21.90%
l	2.34 %	0.48 %
m	1.84 %	0.33 %
n	7.05 %	1.35 %

As can be seen with the data in Table 5.2, when changing the values of the input parameters used for λ and μ change in turn by 1%, result in changes in the relative change of velocity of 12.75% and 21.9%, respectively. If reliable calculations of estimates for stress are to be obtained from changes in velocity it is essential to use the best available material property data set for the base material.

5.5 Physical explanation of the numerical results

As shown in Section 5.3, the S_1 mode is most sensitive to stress when compared to others. This can be explained by considering the dispersion curves shown in Fig. 5.23. As shown for the S_1 mode, the slope of the curve near the cut-off frequency is the steepest, meaning that below the cut-off frequency the group velocity changes most with a change in load, and any factor that can contribute to a change of velocity can also increases the sensitivity to the velocity. Stress can be one of the most important factors making a contribution to determining the velocity.

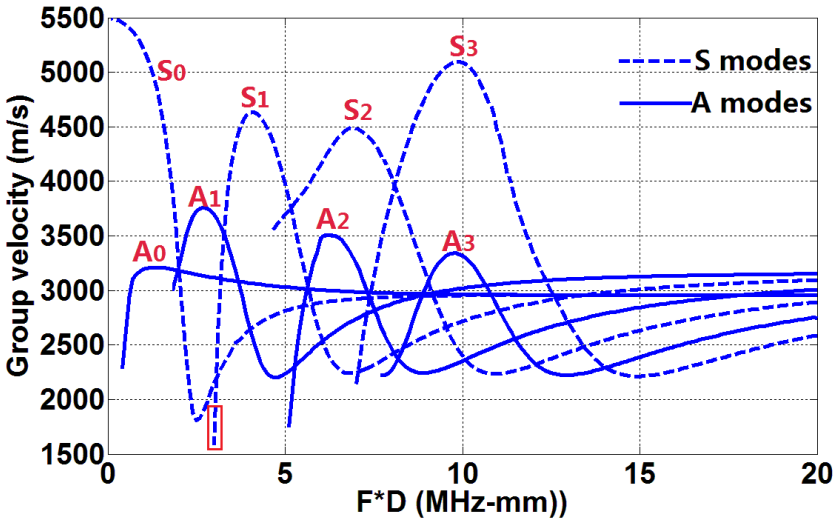

Figure 5.23: Group velocity dispersion curve for Lamb modes in a thin aluminum plate.

5.6 Chapter summary

This chapter shows results for how phase and group velocities change with applied load for the cases when the direction of stress and direction of velocity are either perpendicular or parallel. It shown that the S_1 mode velocity is most sensitive to the applied stress for both cases. Uncertainties in the numerical calculations are also discussed, and an explanation is given as to why the S_1 mode is most sensitive from the perspective of basic physics.

CHAPTER 6. EXPERIMENTAL VERIFICATION OF THE NUMERICAL RESULTS FOR DIFFERENT STRESS CONFIGURATIONS

In this chapter, the experimental system is discussed and data obtained for both perpendicular (A) and parallel (B) cases to be compared with the numerical results reported in chapter 5.

6.1 Experiment set up

To provide the experimental velocity data for comparison with the model estimates with respect to higher-order Lamb wave mode sensitivity to the stress, it is necessary to have obtain samples with controlled loads, so a previously-constructed load frame (Wormley and Thompson, 1989) was dedicated to this project and is shown in Fig. 6.1. It incorporates a manual two-speed hydraulic hand pump that can deliver loads up to 27,000 kg that can be applied to samples with a 6.45 cm^2 cross section, providing loads of up to about 400 MPa. The samples were aluminum sheets 1.6 mm thick with length and width of approximately 50×45 cm. Load is applied to the sheet samples through clamps that attach to bolts set into precision-drilled double rows of 17 holes. The resulting loads were measured using 3 strain gauges (Fig. 6.2) with a P3 Strain Indicator and Recorder (Vishay Measurements Group, Inc). Strain gauges were attached to the aluminum plate with their axes set to be in the same direction as the uniaxial loading, and strain was recorded using the P3 Strain Indicator and Recorder.

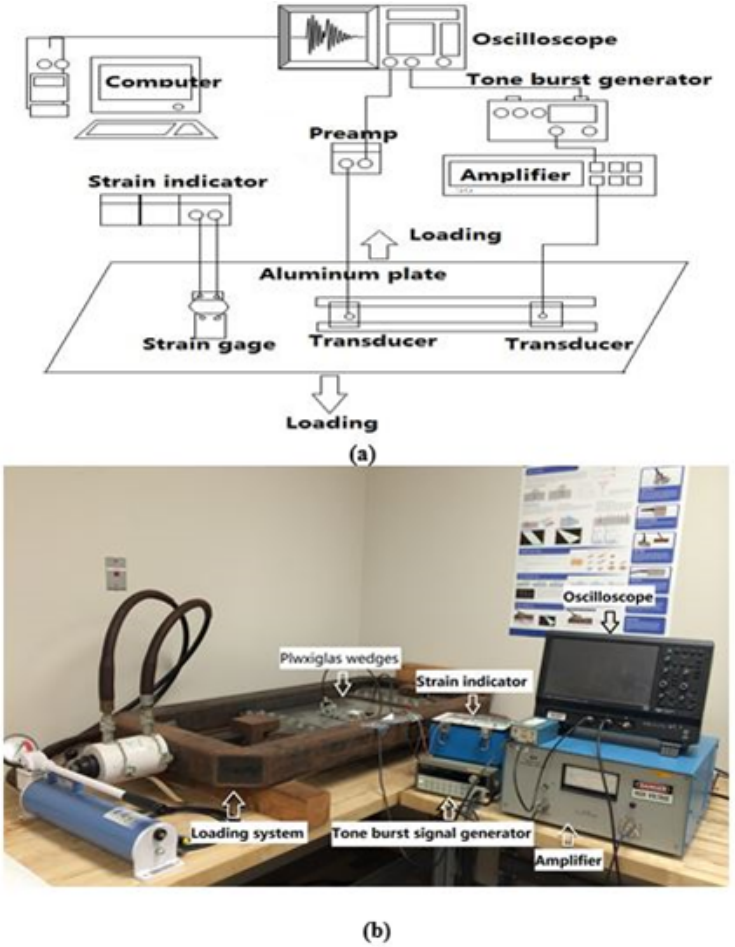

Figure 6.1: Tone burst generator used for the experiment system (for configuration A) (a) system schematic (b) photograph of the complete system.

The ultrasonic plate wave measurement system is comprised of oblique wedges set in a yoke to ensure that they maintain constant separation. Two 2.25 MHz compression wave transducers (Panametrics, type A404) were used. Lamb waves were generated and received using the transducers fastened onto variable-angle Plexiglas wedges, as shown in Fig. 6.3. The transmitter is driven using a tone-burst signal generator (Hewlett Packard 33120A) and a high-power amplifier (Model 3100L, Electronic Navigation Industry, Rochester, NY). The receiver is connected to a pre-amplifier (Olympus) with 50 dB of gain, and signals were measured with a digital oscilloscope (HDO4022, 200MHz High Definition Oscilloscope, TELEDYNE LECROY). The system is used to apply a 30 cycle tone burst intended to generate a specific mode in the plate at a selected frequency, typically at or close to the cut-off frequency. The

incident angle required for each mode was identified using Snell's law and the Lamb wave's velocity dispersion curve. For the case of the S_1 mode, as shown in Fig. 6.4, variation in frequency produced a change in velocity. Mineral oil was used as the couplant between the oblique wedge and aluminum plate. Constant pressure (produced by a cylinder-shape steel element) was applied to the transducer-receiver system to ensure that consistent coupling was maintained. The received signal was amplified and sent to the oscilloscope, where it was digitized at a 100 MHz sampling rate, averaged 64 times to improve the signal-to-noise ratio, and stored for subsequent signal processing.

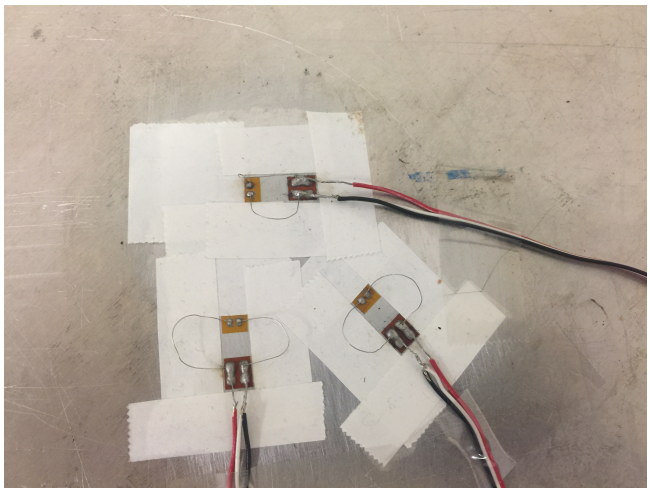

Figure 6.2: Strain gages used in the experiment.

Figure 6.3: Transmission mode used in the experiment.

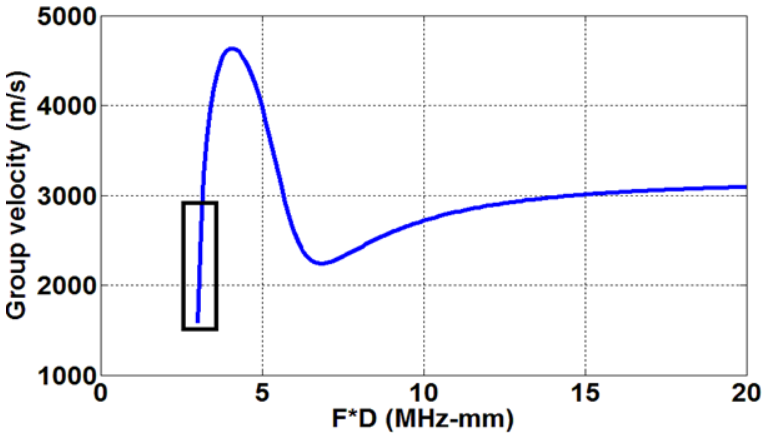

Figure 6.4: S_1 mode group velocity dispersion curve.

An example of a typical received signal is shown in Fig. 6.5. In this case there are four modes in the received signal that can be identified by their velocities, corresponding to the A_1 mode, the fastest, and the S_1 mode, the slowest. These data could be interpreted using the corresponding dispersion curve data shown in Fig. 6.6, the group dispersion curve near 3.0 MHz-mm. The A_1 and A_0 modes arrive first because their velocities are the fastest and the S_1 mode arrives last because it has the slowest velocity. As is discussed, the various modes shown in Fig. 6.5 are in agreement with those predicted for the dispersion curve near 3.0 MHz-mm shown in Fig. 6.6.

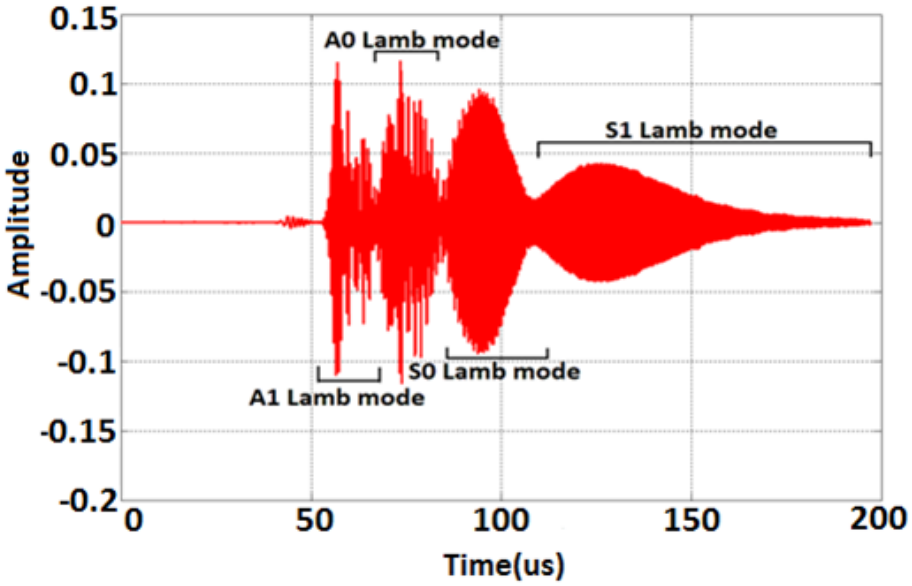

Figure 6.5: An example of a received signal for 3 MHz-mm on an aluminum plate.

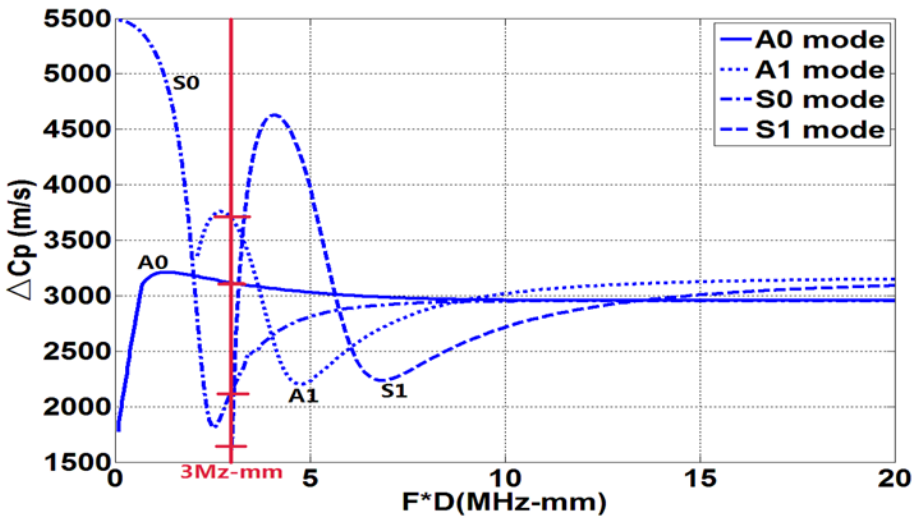

Figure 6.6: Group velocity dispersion curve for aluminum.

For the measurement, the frequency of the tone-burst signal generator was set to the "cut-off" region, based on the thickness of the sample aluminum plate and the dispersion relationship, then the incident angle of the transducer fastened to the variable-angle Plexiglas wedges was identified, based on the Snell's law. The signal generator was then fine-tuned while observing the oscilloscope signal to make the S_1 mode Lamb signal most clear to make sure that the S_1 mode was in the "cut-off" area. The signal was first recorded with no load, then load was added until the strain recorder read 100 $\mu\varepsilon$, after which the signal was recorded after it stabilized. The process was repeated and signal recorded for loads up to 600 $\mu\varepsilon$ at steps of 100 $\mu\varepsilon$. (These strains are read from "P3 strain indicator and recorder", the resolution is $\pm 0.1\% \pm 3\ counts$ of reading.)

6.2 Experiment data analysis

Since the ultrasonic method for stress characterization is based on the change in TOF for ultrasound velocity, appropriate methods for obtaining TOF with required resolution were necessary.

6.2.1 Different methods for TOF measurement

Since ultrasonic methods for stress characterization are based on the relationship between the stress and ultrasound velocity, it is necessary to use a suitable method for an accurate velocity measurement,

which is based on the accurate TOF measurement methods. The signal parameters that are usually applied for TOF evaluation are amplitude, phase, frequency and group delay (Svilainis, 2012; Svilainis and Dumbrava, 2008). For an amplitude based measurement, any factor that can influence the amplitude, such as sample surface roughness and thickness of the couplant, could lead to a inaccurate TOF measurement result. For phase based measurement, the time domain resolution is not available and only limited phase can be measured. The frequency based method also has the disadvantage that on-time domain resolution available, making it hard to select signals for measurement. The group delay method usually uses short signals, signal peak, and zero crossing point, which can all be used as standard for TOF measurement.

The aforementioned methods are only based on the local properties of the signals, there is still a large amount of information of the signal that is not considered. The maximum likelihood criteria, likeness between the reference signal (obtained by using adaptive model) and received signal, can be applied for TOF measurement. The cross-correlation maximum, minimum of difference L1-norm and minimum of difference L2 norm techniques can all be applied for TOF measurement (Svilainis, 2012).

Cross-correlation (CC) method (Zhang and Wu, 2006; Björklund, 2003) is based on the cross-correlation function x for TOF estimation:

$$ToF_{CC} = arg[max(x(\tau))] \tag{6.1}$$

Where x is: $x(\tau) = \int_{-\infty}^{+\infty} S_R(t)S_T(t-\tau)dt$; S_R is the reflected signal and S_T is the transmitted signal.

For the L1-norm minimization method (Zhang and Wu, 2006; Parrilla et al., 1991), TOF can be expressed as:

$$ToF_{L_1} = argmin[L1(\tau)] \tag{6.2}$$

Where $L1$ is: $L1(\tau) = \int_{-\infty}^{+\infty} |S_R(t) - S_T(t-\tau)|dt$.

For the L2-norm minimization method (Zhang and Wu, 2006), TOF can be expressed as:

$$ToF_{L_2} = argmin[L2(\tau)] \tag{6.3}$$

Where $L1$ is: $L2(\tau) = \int_{-\infty}^{+\infty} [S_R(t) - S_T(t-\tau)]^2dt$.

There are already many well-developed methods available for TOF measurement (Ensminger and Bond, 2011) based on the aforementioned theory. The interferometer method for accurate sound velocity measurement in liquids and solids, based on constructive and destructive interference between reflected and transmitted waves, is the preferred method. For a single frequency signal, the velocity of sound can be obtained by wavelength multiplied by frequency. The resonance method is based on finding two successive resonant frequencies (f_1 and f_2) for the media at a distance l from the incident transducer to the receiving transducer. The velocity can be expressed as $c = 2l\Delta f$. The so-called "Sing-around" method can be used for accurate velocity measurement; it is based on the principle that by triggering the single N times and recording the total TOF T, a single TOF t can be expressed as $t = T/N$. The Pulse-Superposition method is based on the superposition of two pulses by controlling the pulse repetition rate. The velocity can be obtained by considering combined pulse travel distance and repetition. These methods can be used for velocity measurement (both phase velocity and group velocity), but usually for non-dispersion signals.

For dispersive waves, especially for the dispersion curve description, the time-frequency method is usually applied. It is a method that can combine analysis time with frequency, a very helpful property for dispersion relationship analysis. There are many methods for time/frequency analysis, including short-time Fourier Transform (STFT), wavelet transform, the smoothed Wigner-Ville distribution, and others. The STFT method is highlighted in this study: STFT divides the time domain signal into a series of small fragments and applies FFT to each; an expression for STFT can be written as (Niethammer et al., 2001):

$$S_1(\omega, t) = \frac{1}{2\pi} \int_{-\infty}^{+\infty} e^{-i\omega\tau} x(\tau) s(\tau - t) d\tau \tag{6.4}$$

Where $s(t)$ is a window function (Hanning window or Gaussian window), and $x(\tau)$ is the signal needing to be transformed. $S_1(\omega, t)$ is the Fourier Transform of $x(\tau)s(\tau - t)$. Typically the time index t can influence the resolution of the results.

6.2.2 The STFT method for TOF measurement

The use of the STFT method has been previously demonstrated as an effective method for dispersion curve analysis (Hamada and Shibuya, 1995; Wang and Yuan, 2007). The theory and physical meaning

of the STFT method have been previously described in the literature (Hamada and Shibuya, 1995; Wang and Yuan, 2007) and it has also been reported that the arrival time for group velocity at specific frequencies can be obtained by determining the magnitude of the coefficients.

The group velocity for different modes can be obtained by varying the wedge angle based on Snell's law. When a range of different group velocity data are obtained for various modes at different frequencies, the Lamb wave group velocity dispersion curve can be obtained.

In using this approach the steps involved in identifying arriving time by STFT are:

(1) Apply the STFT algorithm, identify the time slice (Wang and Yuan, 2007) corresponding to the amplitude at the center frequency;

(2) Record the time constant to find the arrival time t_1 of the Lamb with the largest amplitude in the time slice. Change the transducer separation d and again record the arrival time t_2. The group velocity of the Lamb wave at the center frequency can then be obtained by dividing the distance d by the time difference$t = t_2 - t_1$;

(3) The Lamb wave group velocity at different frequencies can then be obtained, by adjusting the applied center frequency for the incident signal.

The STFT algorithm is used for time-frequency analysis. An example of the data obtained corresponding to the S_1 Lamb mode is shown in Fig. 6.7. It gives a representation for the time domain and frequency information at the same time. The energy is seen to be concentrated near 1.9 MHz.

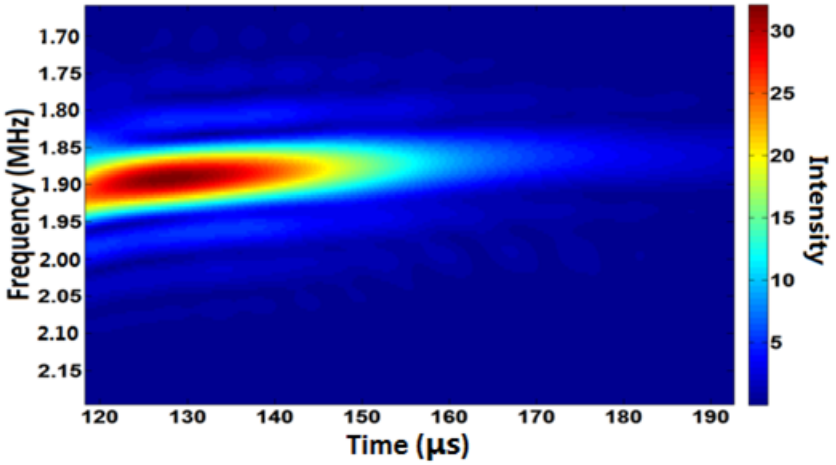

Figure 6.7: Time-frequency analysis of S_1 mode, for the sample aluminum plate.

For a particular frequency, the relationship between time and amplitude can be obtained from Fig. 6.7. Fig. 6.8 shows an example of the time and amplitude relationship for the frequency f_0=1.9 MHz. As is shown in the figure, the maximum amplitude of the curve corresponds to t, meaning that for the frequency f_0=1.9 MHz its arriving time is t.

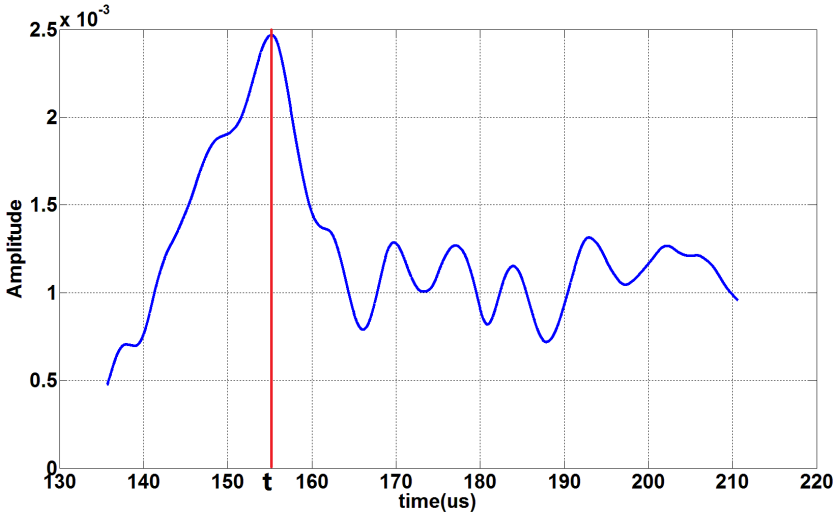

Figure 6.8: Time-frequency analysis for frequency f_0=1.9 MHz.

6.2.3 Measurement of TOF with the STFT method

Following characterization of the S_1 Lamb mode, the effects of applying a load to the aluminum plate were investigated. For a pair of transducers at a set separation d in the assembly the arrival time t_1 was measured with by the STFT method for a certain frequency of the S_1 mode. The load was then applied and the arrival time t_1' recorded. The transducer separation was increased by a pre-selected increment d' and the new arrival time t_2 recorded, and the load was then applied and the arrival time recorded as t_2'. The group velocity could then be calculated using the expression: $V_g = d'/(t_2 - t_1)$. The group velocity with loading can also be expressed as: $V_{gL} = d'/(t_2' - t_1')$. Time domain data were recorded with loads from 0 to 600 $\mu\varepsilon$, at intervals of 100 $\mu\varepsilon$.

Fig. 6.9 shows an example of TOF data for the perpendicular case; the TOF increases as the load increases, meaning that the velocity decreases, in general agreement with the numerical results shown in the last chapter for the perpendicular case.

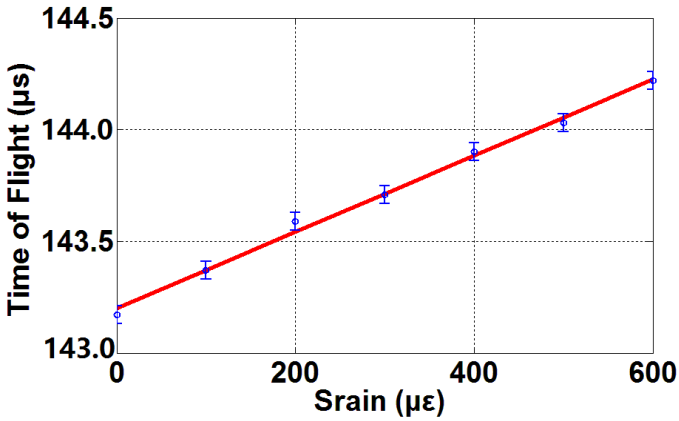

Figure 6.9: TOF at various strains for the S_1 mode for the perpendicular case.

Fig. 6.10 shows an example of TOF data for the parallel case in which TOF goes down as load goes up. This means the velocity increases, in general agreement with the numerical results shown in the last chapter for the parallel case.

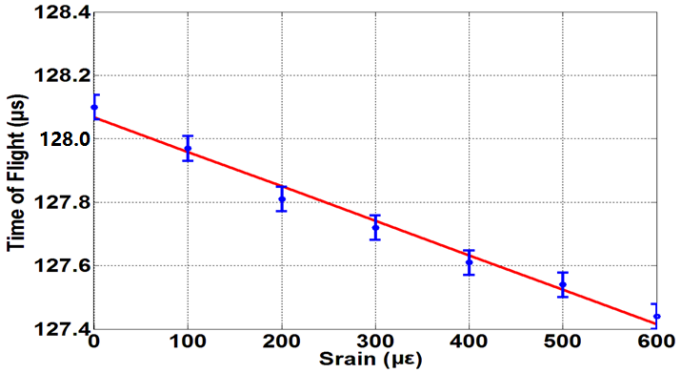

Figure 6.10: TOF at various strains for the S_1 mode for the parallel case.

From Fig. 6.9 and 6.10, a TOF difference can be seen for 0 strain location for both perpendicular and parallel cases, this is because pre-loading was added to make sure the plate was flat. The experiment for the perpendicular and parallel configurations were performed separately on different dates, when the plate was regarded flat after a suitable pre-loading was added, the strain gauge indicator was then corrected to zero. The TOF difference is a result of the pre-loading difference that has no influence on the final results where only the relative change in velocity is of concern.

6.2.4 The possible influence of locations

Four measurements were made for both perpendicular (A_1, A_2, A_3 and A_4) and parallel (B_1, B_2, B_3 and B_4) configurations at intervals $5cm$ for different locations (black dots), as shown in Fig. 6.11.

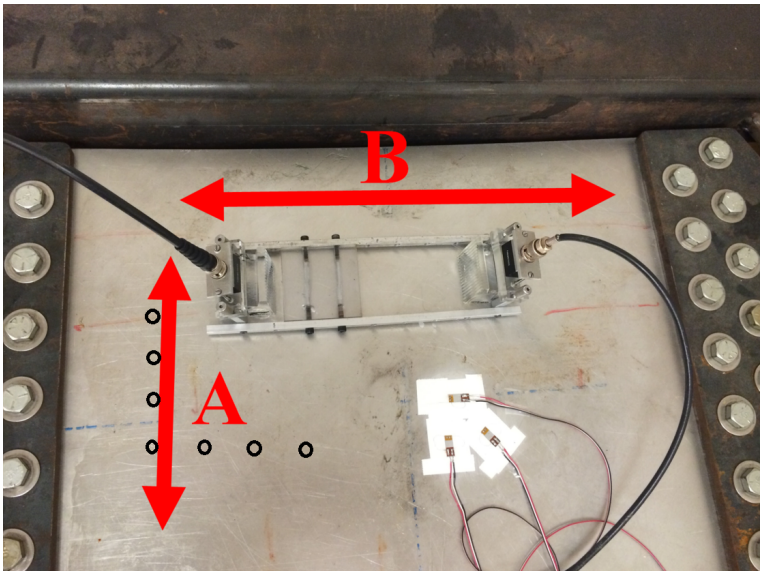

Figure 6.11: Schematic showing measuring directions and locations.

The results for perpendicular and parallel configurations are shown in Fig. 6.12 and Fig. 6.13, respectively. These figures reveal no obvious differences, meaning that there are no other factors such as variations in thickness, grain size or texture that significantly influence the results in these experiments.

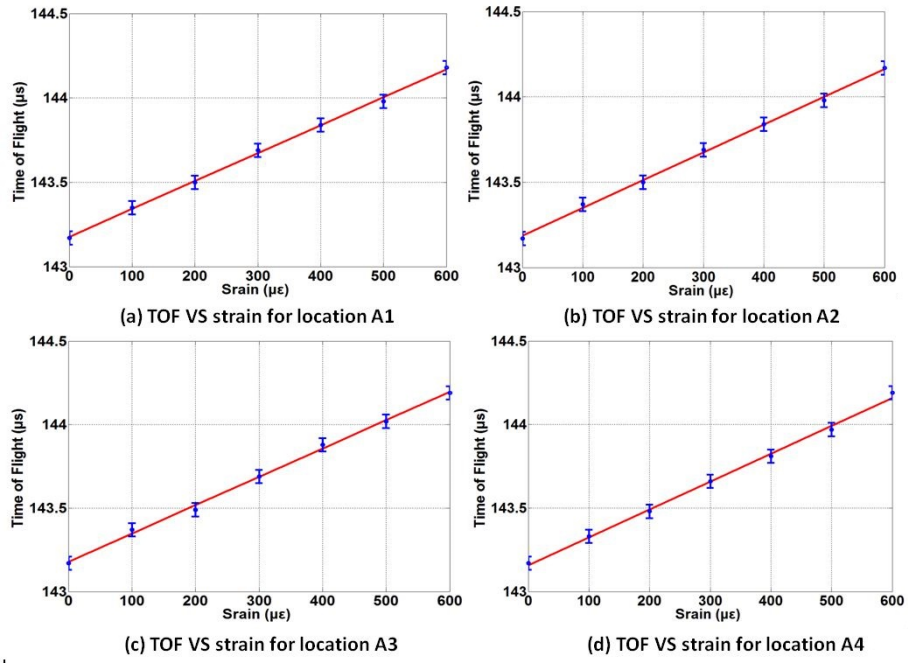

Figure 6.12: TOF at various locations and strains for the S_1 mode for the perpendicular case.

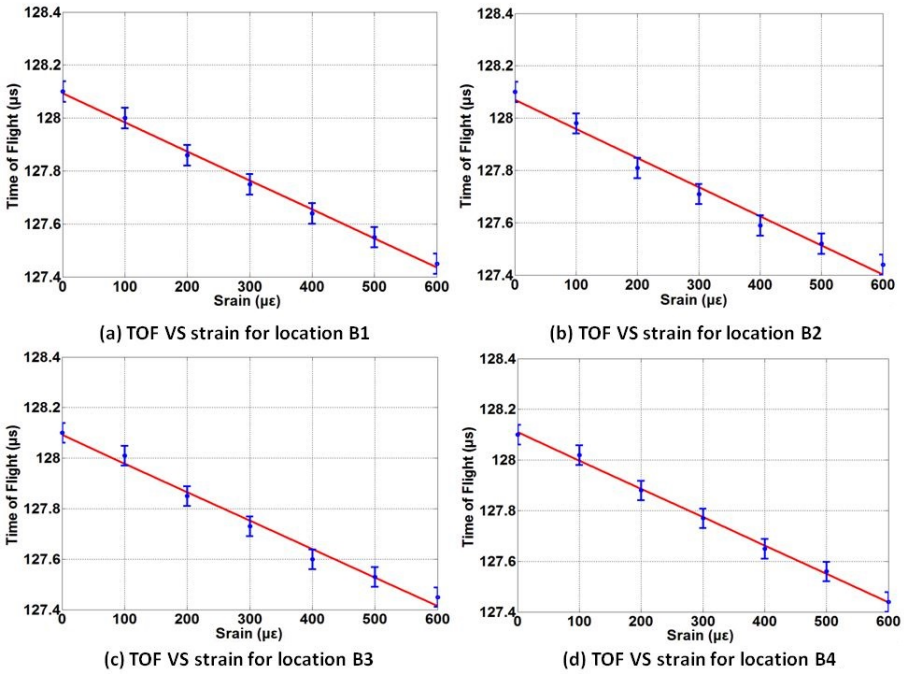

Figure 6.13: TOF at various locations and strains for the S_1 mode for the parallel case.

6.2.5 Plate thickness monitored by ultrasonic thickness gauge

As discussed in Chapter 5, the S_1 mode near the cut-off frequency is much more sensitive to stress. The problem for the "cut-off frequency" region is that it is highly dispersive and both the thickness of the plate and the frequency of the incident signal should be constant to obtain reliable results. The thickness of the plate was monitored by an ultrasonic thickness gauge to ensure that it was near constant. Fig. 6.14 shows the ultrasonic thickness gauge (Model 25MULTIPLUS, GE Panametrics) used for plate thickness monitor. The gauge was calibrated by a 7075 Aluminum stepped (1mm, 2mm, 3mm, 4mm, and 5mm) thickness gauge which is shown in Fig. 6.15. A 10 MHz contact transducer with a maximum resolution 0.001 mm was used for the measurement.

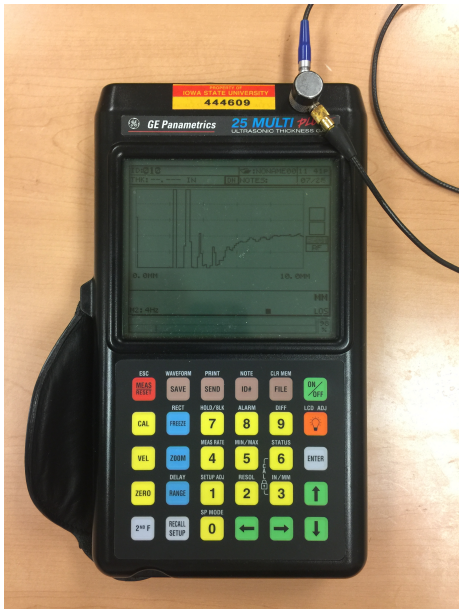

Figure 6.14: Ultrasonic thickness gauge used for plate thickness measurement.

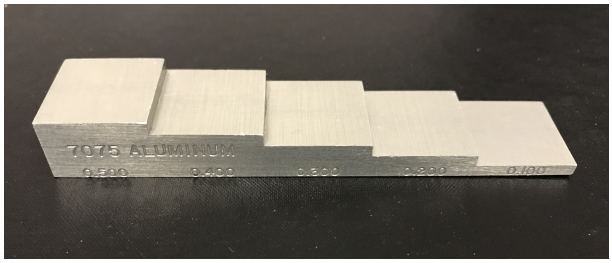

Figure 6.15: The 7075 Aluminum stepped thickness gauge used in the experiment.

The ultrasonic thickness gauge measurement was calibrated by the isotropic 7075 Aluminum stepped thickness gauge and the measurement result was based on the ultrasound velocity. The measurement was carried out for both perpendicular and parallel configurations. For each configuration, the measurement was made at ten different points along a line on the plate with the results shown in Table 6.1. Observing Table 6.1, it can be seen that there are only small difference in the measured thickness d. The mean value for the perpendicular configuration can be calculated as: $d = 1.602mm$, while for the parallel case it can be calculated as: $d = 1.602mm$.

Table 6.1: Thickness measurement results using ultrasonic thickness gauge (unit: mm)

cases	1	2	3	4	5	6	7	8	9	10
perpendicular	1.601	1.600	1.603	1.602	1.605	1.600	1.602	1.601	1.602	1.604
parallel	1.602	1.603	1.601	1.600	1.602	1.604	1.601	1.603	1.604	1.602

The thickness of the plate was measured again for both perpendicular and parallel configurations with the same locations using micrometer. The results are shown in Table 6.2. When comparing Table 6.1 and Table 6.2, it is seen that the thickness results measured by the ultrasonic thickness gauge and by the micrometer are very similar. Considering that the Ultrasonic thickness gauge measurement was based on the ultrasound velocity, it means the aluminum plate used in the experiment is isotropic and the TOF measurement results have no influence by texture, grain size and etc.

Table 6.2: Thickness measurement results using micrometer (unit: mm)

cases	1	2	3	4	5	6	7	8	9	10
perpendicular	1.600	1.600	1.603	1.601	1.605	1.600	1.602	1.601	1.602	1.603
parallel	1.602	1.603	1.600	1.600	1.602	1.603	1.601	1.603	1.603	1.602

6.3 Chapter summary

This chapter describes the experimental system set-up process for both the perpendicular (A) and parallel (B) cases. The received signal was analyzed to distinguish among different modes (A_0, A_1, S_0 and S_1 modes). The STFT method was used for data analysis to obtain the group velocity. The thickness of the plate was monitored by an ultrasonic thickness gauge to ensure that its was constant to ensure a stable plate thickness that did not influence the measurement results.

CHAPTER 7. COMPARING EXPERIMENTAL RESULTS WITH NUMERICAL RESULTS

This chapter presents and discusses the experimental results, presented in Chapter 6,including analysis of accuracy, and compares them with numerical results reported in Chapter 5 for both perpendicular and parallel cases. The results show that numerical results and experiment results are in good agreement.

7.1 Errors, accuracy and precision

For obtaining reasonable measurement results it is necessary to consider error, accuracy, and precision. The exact value of a physical quantity can not be obtained directly by experiments, but it can be effectively evaluated by repeating measurement and considering possible errors.

7.1.1 Accuracy and precision

”Accuracy” and ”precision” (or ”repeatability”) (Dieck, 2007) are two standard metrics used to describe values obtained as experimental results.

Measurement of accuracy describes how close experiment results are to the ”true” value. Usually the true value is not available so is necessary to determine the accuracy and, with respect to the experimental measurements, usually obtained as the mean of several measurements, is regarded as the best estimate of measurement.

Precision refers to how closely the measurement results agree with those of others, and a small range of difference usually indicates that the data are highly reproducible. For experimental measurements, the standard deviation of the set of measured values is commonly used to define the measurement range.

7.1.2 Systematic errors and random errors

Systematic errors (Rabinovich and Rabinovich, 2010), representing the limitations of measurement theory or measurement methods, are caused by inherent errors of the measurement tools. Within the same measurement environment, the values of measurement results are always either all larger or all smaller than the true values, so these errors are also called ”one-sided” errors. While systematic errors can not be eliminated by repeating the experiment, they can be reduced by improving a measurement method and its implementation.

Random errors are another type of error (Rabinovich and Rabinovich, 2010). They can be caused by instability of the experiment device, negative influences in the measurement environment (like noise), and the personal actions of the operator. A set of measurement results subject to random errors can obtain larger or smaller values than the true value, so they are also called ”two-sided” errors. Random errors can be described by observations from repeating the measurement.

7.1.3 Mean and standard deviation

The definition of mean, standard deviation, and standard error can be expressed as follows (González and Herrador, 2007):

For an experimental measurement repeated N times producing values of x_i $(i = 1, 2, 3..., N)$, the mean $\bar{x}$ can be expressed as:

$$\bar{x} = \frac{1}{N}\sum_{i=1}^{N} x_i = \frac{1}{N}(x_1 + x_2 + x_3 + ... + x_{N-1} + x_N) \tag{7.1}$$

The standard deviation σ_x of the measured values x_i $(i = 1, 2, 3..., N)$ can be expressed as:

$$\sigma_x = \sqrt{\frac{1}{N-1}\sum_{i=1}^{N}(x_i - \bar{x})^2} \tag{7.2}$$

The standard error S can be expressed as:

$$S_x = \sqrt{\frac{1}{N(N-1)}\sum_{i=1}^{N}(x_i - \bar{x})^2} = \frac{\sigma_x}{\sqrt{N}} \tag{7.3}$$

7.1.4 Uncertainty of the measurement results

For obtaining accuracy in measuring Lamb wave velocity, TOF and the gauge length measurement should be sufficiently accurate. Fig. 7.1 shows the transducer locations.

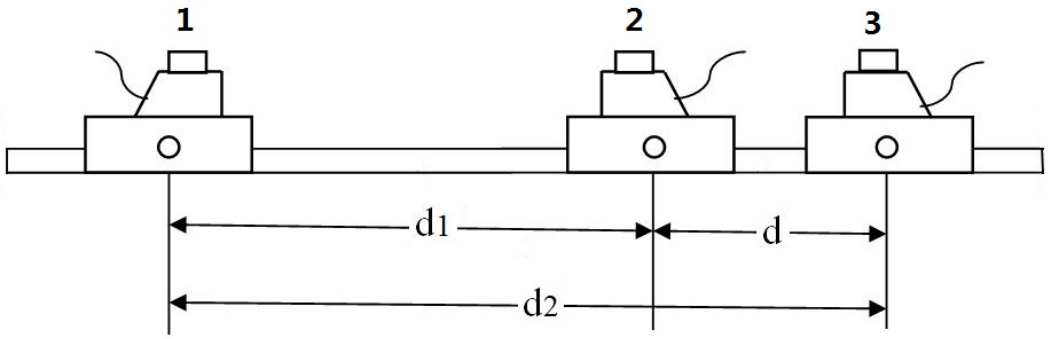

Figure 7.1: Diagram showing transducer measurement configuration.

Table 7.1 shows the resolution for TOF and the gauge distance d in the experiment, obtained from the measurement results.

Table 7.1: Resolution of parameters for velocity measurement

Parameter	**Resolution**
ΔTOF	2 ns
d	0.02mm

The propagation of uncertainty can be written as shown in Table 7.2 (Baird, 1962; Bevington et al., 1993) :

Table 7.2: The propagation of uncertainty

Operation	**Expression**	**Uncertainty**
Addition/Subtraction	$z = x \pm y$	$\delta z = \sqrt{\delta x^2 + \delta y^2}$
Multiplication	$z = xy$	$\delta z = \lvert xy \rvert \sqrt{(\frac{\delta x}{x})^2 + (\frac{\delta y}{y})^2}$
Division	$z = \frac{x}{y}$	$\delta z = \lvert \frac{x}{y} \rvert \sqrt{(\frac{\delta x}{x})^2 + (\frac{\delta y}{y})^2}$
Power	$z = x^n$	$\delta z = \lvert n \rvert x^{n-1} \delta x$
Multiplication by a Constant	$z = cx$	$\delta z = \lvert c \rvert \delta x$
Function	$z = f(x, y)$	$\delta z = \sqrt{(\frac{\partial f}{\partial x})^2 (\delta x)^2 + \frac{\partial f}{\partial y})^2 (\delta y)^2}$

7.2 Relative change in the group velocity

For the pair of transducers at a given separation (d_1), as shown in Fig. 7.1, the arrival time (t_1) was measured using the STFT method for a certain frequency of the S_1 mode. The load was then applied and the new arrival time ($t_1^{'}$) was recorded. The transducer separation was then increased to a new position (d_2) and the new arrival time recorded (t_2). Once again the load was applied and the arrival time recorded ($t_2^{'}$). The group velocity can then be calculated using the expression:

$$V_g = \frac{d_2 - d_1}{t_2 - t_1} = \frac{d}{t_2 - t_1} \tag{7.4}$$

The group velocity with loading is calculated as:

$$V_{gL} = \frac{d_2 - d_1}{t_2^{'} - t_1^{'}} = \frac{d}{t_2^{'} - t_1^{'}} \tag{7.5}$$

The time domain data were recorded with loads ranging from 0 to 600 $\mu\varepsilon$ at time intervals of 100 $\mu\varepsilon$. The measurements were each performed six times and the results averaged to enhance measurement accuracy. Strain and TOF were recorded, and their mean ($\bar{x}$) was regarded as a good estimate of the true value. Error bars are expressed in term of standard error ($S = \sigma/\sqrt{N}$, where σ is the standard deviation and N is the number of the measurement).

7.2.1 For the perpendicular case

The velocity for the S_1 mode was first measured without applied stress and was approximately 1700 m/s. This result can be compared with the group dispersion relationship shown in Fig. 7.2 to evaluate the excitation position on the dispersion curve for the S_1 mode. As shown in Fig. 7.2, the excitation area is near the "cut-off" frequency (about 3.01 $MHz - mm$).

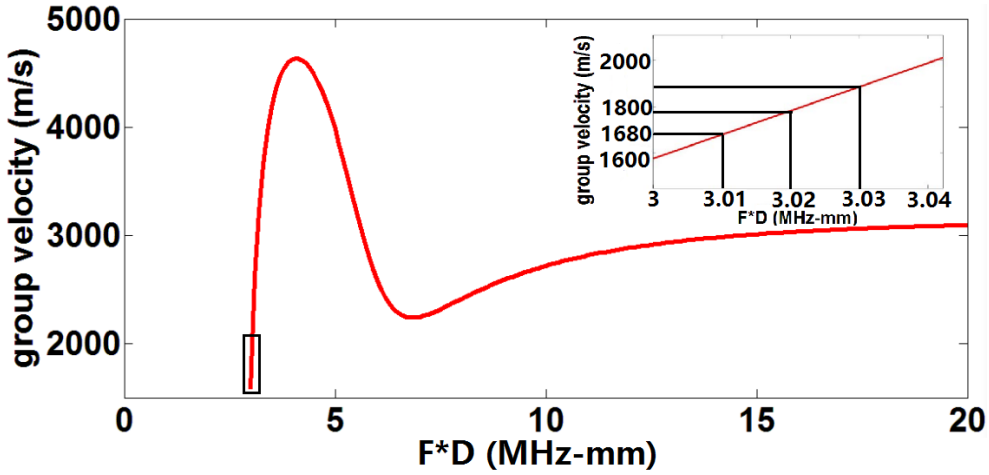

Figure 7.2: Group velocity dispersion relationship.

The relative change of velocity can be written as the change time t:

$$\frac{v_{gL} - v_g}{v_g} = \frac{\frac{d}{t_2 - t_1} - \frac{d}{t_2 - t_1}}{\frac{d}{t_2 - t_1}} = \frac{\frac{d}{t_{gL}} - \frac{d}{t_g}}{\frac{d}{t_g}} = \frac{t_g - t_{gL}}{t_{gL}} \tag{7.6}$$

Experimental results for the relative change of velocity for both with load and without load can be calculated by Eq. 7.6. The model (at 3.0 MHz-mm) and experimental data (red color) with error bars are plotted against strain as shown as Fig. 7.3 where it can be seen that the absolute value of slope for the experiment data is $2.72e^{-5}\mu\varepsilon^{-1}$, a little less than that for the model result data ($3.25e^{-5}\mu\varepsilon^{-1}$).

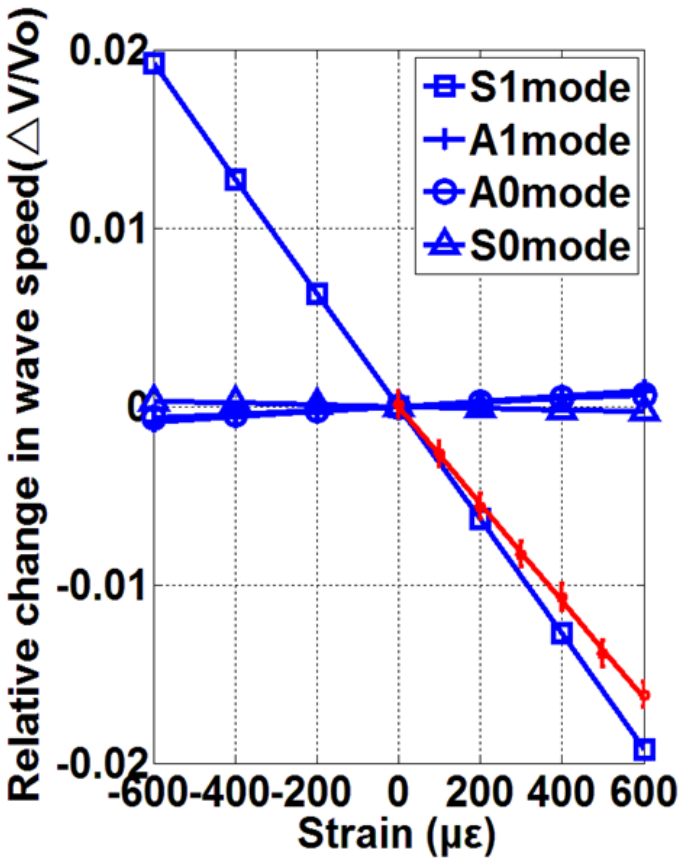

Figure 7.3: Comparison of experimental (red color) and model data for velocity change against strain for various Lamb modes.

When the S_1 mode velocity was investigated, it was found to be less sensitive than predicted for the cut-off at 3.0 MHz-mm. Upon review of the data in Fig. 7.2, the S_1 dispersion curve, the results showed that the actual wave generated experimentally was closer to 3.01 MHz-mm than to the value "3.00 MHz-mm" used for numerical calculation. The model data for the S_1 mode at 3.00 and 3.01 MHz-mm at various loads, along with the experimental data, are shown in Fig. 7.4, showing that the numerical results at 3.01 MHz-mm and the experiment results are in good agreement.

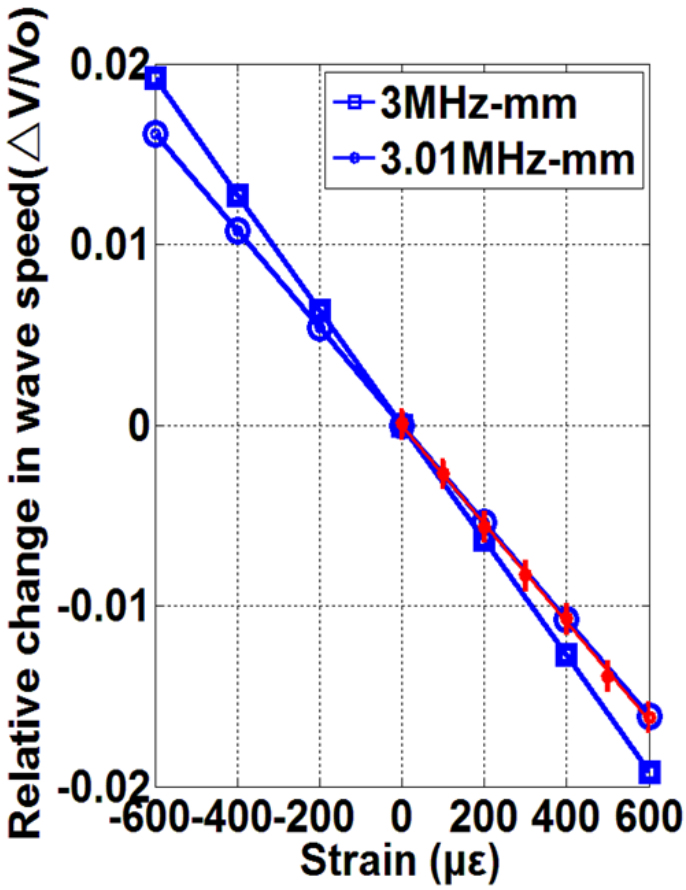

Figure 7.4: Comparison of experimental S_1 Lamb mode velocity change against load (red color) and numerical model results for cases at 3.00 and 3.01 MHz-mm.

Fig. 7.5 shows the relative change in group velocity for different locations (A_1, A_2, A_3 and A_4, as discussed in chapter 6) for the perpendicular configuration. The red bars represent error bars with "frequency-thickness" changes of 1 percent. As can be seen in the figure, a change of measurement locations produced no significant change in the results, indicating that there are no major factors, such as variations in thickness, grain size, texture, etc., influencing the results. Also, observation of the red error bar shows a relatively large variation associated with a 1 percent change of the frequency-thickness combination, because there is a steep slope in the dispersion curve near the cut-off frequency, meaning that the frequency-thickness combination should remain constant during the measurement.

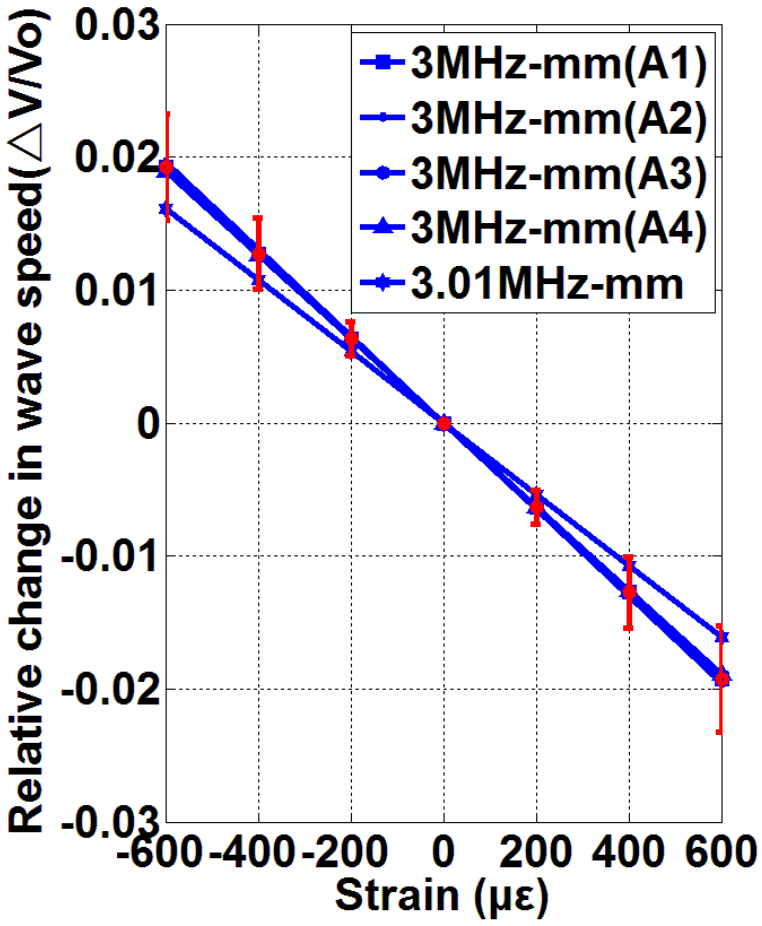

Figure 7.5: Comparison of experimental S_1 Lamb mode velocity change against load (red color) and numerical model results for cases at 3.00 and 3.01 MHz-mm.

7.2.2 For the parallel case

The velocity was measured without stress and found to be approximately $1750\ m/s$. This result can be compared with the group dispersion relationship shown in Fig. 7.2 to evaluate the excitation position on the dispersion curve for the S_1 mode, showing that the excitation area is near the "cut-off" frequency (between $3.01 MHz-mm$ and $3.015\ MHz-mm$).

The experimental results for the relative change of velocity with load and without load can also be calculated using Eq. 7.6. The model data (at 3.0 MHz-mm) and experimental data (red color) with error bars are plotted against strain as shown as Fig. 7.6.

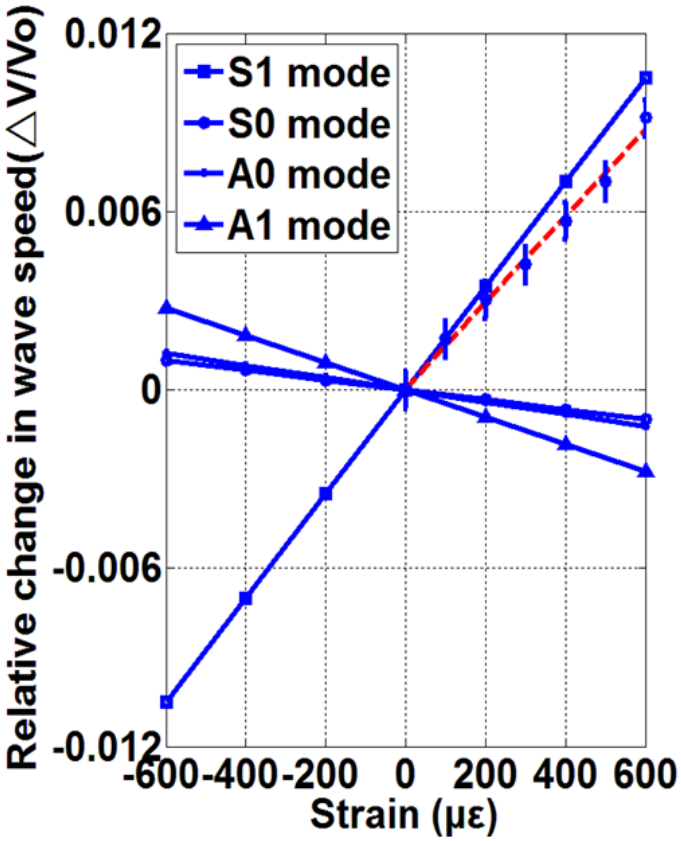

Figure 7.6: Comparison of experimental (dash line) and model data for velocity change against strain for various Lamb modes.

From Fig. 7.6, it can be seen that the absolute value of slope of the experimental data is $1.44e^{-5}\mu\varepsilon^{-1}$, less than that for the model result data ($1.67e^{-5}\mu\varepsilon^{-1}$). The reason for this discrepancy is that the experimental mode was not exactly located at the cut-off frequency. Fig. 7.7 shows a comparison between the numerical results and experiment results for the case of a 3.015 MHz-mm S_1 mode. As can be seen in the figure, the numerical results and the experiment results are in good agreement.

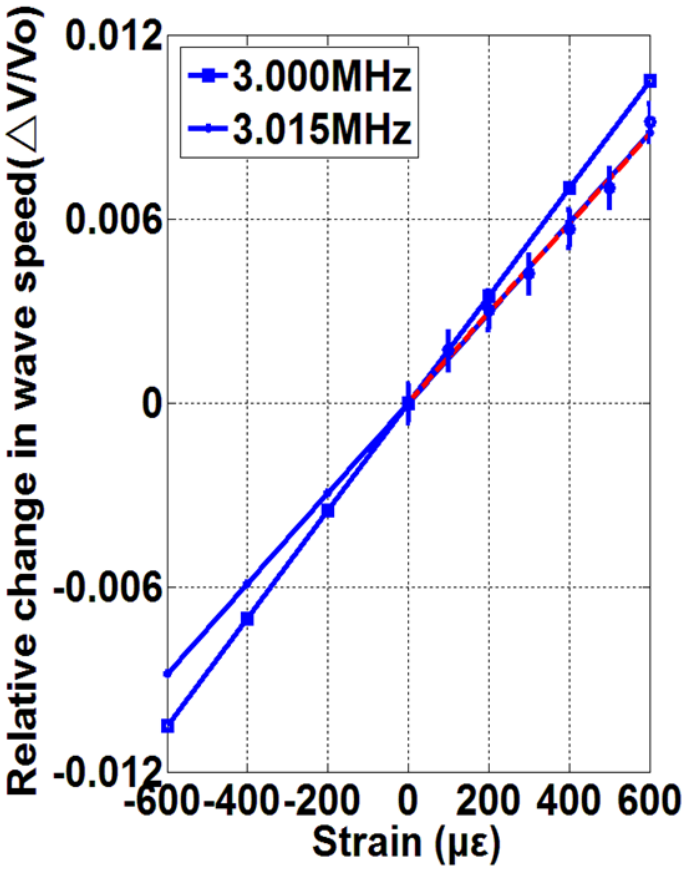

Figure 7.7: Comparison of experimental S_1 Lamb mode velocity change against load (dash line) and numerical model results for cases at 3.0 and 3.015MHz-mm.

Fig. 7.8 shows the relative change in group velocity for different locations (B_1, B_2, B_3 and B_4, as discussed in Chapter 6) for the parallel configuration. Again the red bars represent error bars with frequency thickness combined changes of 1 percent. As shown in the figure, with a change of measurement locations there is no significant change for the results, meaning there are no significant effect due to factors such as variation in thickness, grain size, texture, etc., that obviously influence the results. Also, the red error bars reflect a relatively large variation for a 1 percent change of in the frequency-thickness combination, again because it there is high slope region of the dispersion curve near the cut-off frequency.

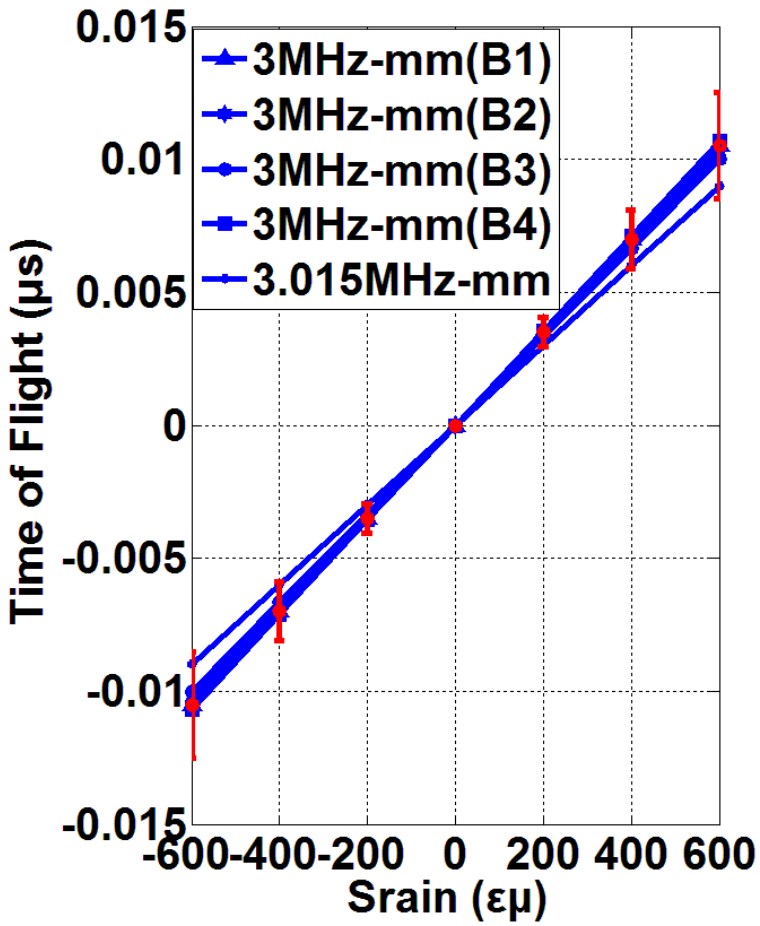

Figure 7.8: Comparison of experimental S_1 Lamb mode velocity change against load (red color) and numerical model results for cases at 3.00 and 3.015 MHz-mm.

7.2.3 Comparison of the parallel and perpendicular case

A comparison between the velocity changes under load for parallel and perpendicular cases is shown in Fig. 7.9. The data obtained for these two cases are in good agreement with the model data at the corresponding frequency-thickness value, as discussed above. From Fig. 7.9 it can be seen that, for the perpendicular configuration the load decreases the velocity, while for the parallel configuration the load increases the velocity. Also, for the perpendicular configuration the relationship between ultrasound velocity and stress are more sensitive than for the parallel configuration.

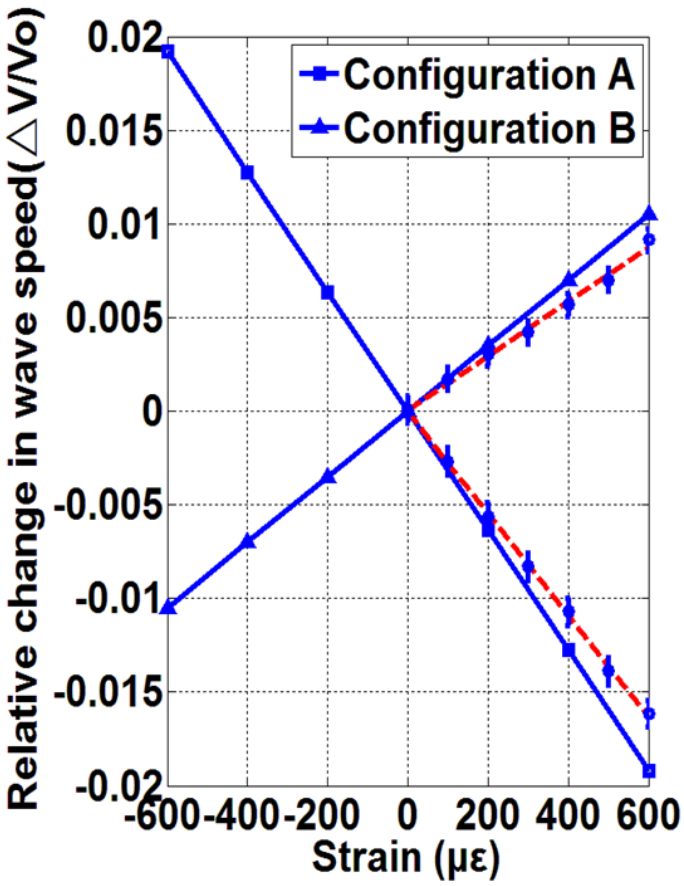

Figure 7.9: Comparison of experimental S_1 Lamb mode velocity change against load (dash line, with frequency-thickness combination 3.01 MHz-mm for configuration A and 3.015 MHz-mm for configuration B) and numerical model results (with frequency-thickness combination 3.00 MHz-mm) for parallel and perpendicular case.

7.3 Estimation of the resolution for the stress measurement system

The S_1 Lamb wave near the "cut-off frequency" region is a good choice for stress measurement, considering its high sensitivity to the stress. For stress measurement, there are a lot of factors that can influence the measurement resolution: the distance between the transmitting and receiving transducers, the resolution of the TOF measurement method, the character of the measured samples, including the surface roughness, the texture, the grain variation, and other factors that can influence the ultrasound velocity.

For the experimental system used in this project, the distance between the transmitting and receiving transducer is 180.390 $\pm$ 0.003 mm, the distance between two receiving transducers (with number 2 and 3, shown in Fig. 7.1) is 25.770 $\pm$ 0.001 mm. The TOF measurement uncertainty is 2 ns with the applied STFT signal processing method. The aluminium plate used in this project is regarded as isotropic with constant thickness.

7.3.1 For the perpendicular case

Observing Fig. 7.4 (last section), it is shown that the simulating point in the experiment is 3.01 MHz-mm for the perpendicular configuration. The relationship between the velocity and the stress (range: 0 to 20 MPa) obtained from the numerical model is shown in Fig. 7.10. As shown in the figure, it is a linear relationship between the stress and the group velocity, the slope of the curve is 0.7 (m/s)·MPa.

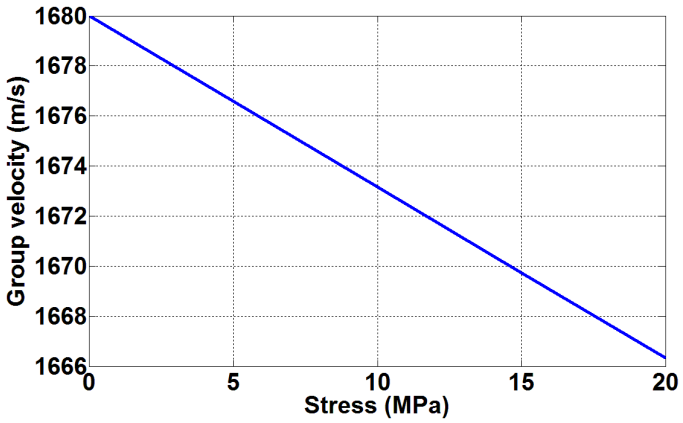

Figure 7.10: The relationship between the stress and the group velocity for the perpendicular configuration with frequency thickness combination 3.01 MHz-mm.

Considering the distance between the two receiving transducers, the TOF measurement resolution, the propagation of the resolution shown in Table 7.2, and the relationship between the stress and the group velocity shown in Fig. 7.10, the stress value should larger than 3 MPa to obtain a reasonable TOF value. In other words, the resolution of the experiment system for stress measurement is estimated to be $\pm$ 3 MPa.

7.3.2 For the parallel case

Observing Fig. 7.8 (last section), the simulating point in the experiment is 3.015 MHz-mm for the parallel configuration. The relationship between the velocity and the stress (range: 0 to 20 MPa) obtained from the numerical model is shown in Fig. 7.11. Again it is a linear relationship as for the parallel configuration, the slope of the curve is 0.375 (m/s)·MPa.

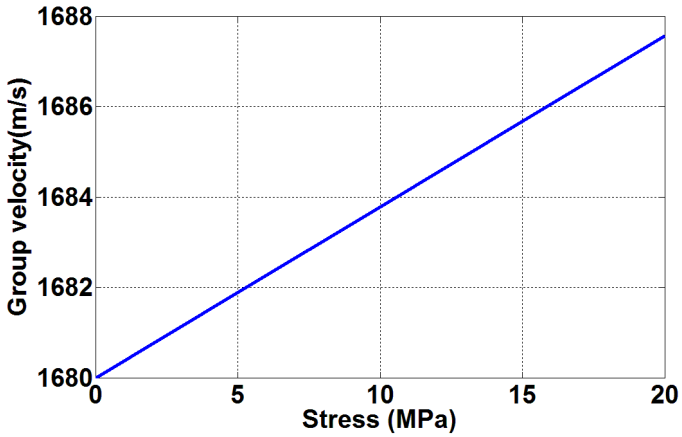

Figure 7.11: The relationship between stress and group velocity for the parallel configuration with frequency thickness combination 3.015 MHz-mm.

Considering all the factors stated for the perpendicular configuration, the stress value should larger than 6 MPa to obtain a reasonable TOF value, which means the resolution of the experiment system for stress measurement is less than the perpendicular case and is $\pm$ 6 MPa.

7.4 Chapter summary

This chapter describes in detail the methodology for calculating the S_1 mode group velocity with and without load for both configuration A and configuration B. The experimental results show good agreement with the numerical results.

CHAPTER 8. DISCUSSION

This chapter reviews and discusses the major results of the thesis, whose topic is enhancing the sensitivity of ultrasonic velocity measurement of stress. Two aspects, LCR waves and guided waves, are discussed to provide guidance with respect to enhancing stress measurement methods, recognizing that there are still natural limitations to using ultrasonic methods.

8.1 The LCR wave method for stress characterization

While the LCR method has been widely used for possible residual stress characterization (Buenos et al., 2012). there are additional possibilities for enhancing the sensitivity between stress and an LCR wave. When the ultrasound velocity and the stress occur in the same direction, the sensitivity reaches a maximum. There is usually an angle θ between the bulk wave and in plate stress (Fig. 8.1, as described in Chapter 3), and the goal of this work has been to use models to investigate parameters that could reduce the angle θ.

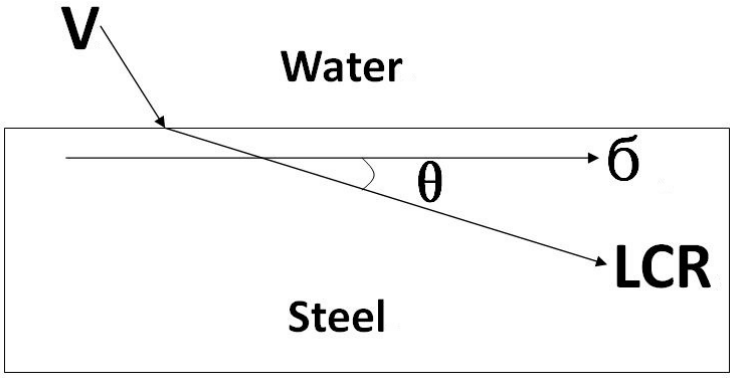

Figure 8.1: Direction difference between the LCR wave and the possible stress σ.

A 2D "water-steel" model has been used to investigate LCR wave properties. The Orthogonal Experiment Method was used to analyze the parameters (the incident angle, the center frequency, the aperture of the transducer, and the receiving locations) that can influence the directivity of the LCR wave, that in turn determines sensitivity between the LCR wave and the stress. The results show that the incident angle, the center frequency, and the aperture of the transducer are the main factors contributing to the directivity of the LCR wave, and in determine the sensitivity of the LCR wave.

The effect of the incident angle is easy to understand based on Snell's law, since the wave will change its propagation direction with a change in the incident angle. An increase in frequency will result in an increase in the wave attenuation, meaning the LCR wave would propagate towards the surface. With respect to the aperture of the transducer, it also makes a significant contribution to the directivity of the LCR wave. As the transducer's aperture increases, the LCR wave trends toward 90 degree (parallel to the interface between water and steel). So, to increase the directivity of the LCR wave, the choices are among selecting an optimized incident angle (an angle lager than the first cirtical incident angle, based on Snell's law), increasing the transducer center frequency, and increasing the transducer aperture.

As mentioned in chapter 4, the LCR wave is most sensitive when its propagation direction is the same as that of the stress. To achieve maximum sensitivity, the possible stress field (or at least its direction) of the sample should be known. For a known stress axis, such as for the stress generated by rolling and welding, this is possible, but under most circumstance it is difficult to evaluate the direction of the stress in advance.

Also, since a LCR wave propagates near the surface of the sample, it is very difficult to detect possible stresses deeper in the sample. On the hand, if the sample is in the form of a plate-like sample, Lamb wave are generated rather than LCR waves. Lamb waves will be discussed in the next section.

8.2 Lamb waves for stress measurement

The ultrasonic method for stress characterization in the plate-like material is the Lamb wave, not bulk waves, that generates in the sample. The ultrasonic method for stress characterization is based on the change of TOF for ultrasonic velocity. As shown in Eq. 1.1 (Chapter 1), the measured TOF includes

the contribution from applied stress, residual stress, texture, and temperature. In this project, only the applied load was considered in the numerical model; for the experiments, an isotropic aluminum plate without residual stress was used. The applied load was added to the sample plate to consider the relationship between load and ultrasound velocity. The experiment was performed at room temperature. In this project, TOF change is only influenced by applied loads, which assures that all the results about the relationships between load and ultrasound velocity are reliable.

It is shown that the S_1 Lamb wave near the cut-off frequency (Fig. 8.2) is more sensitive than the effects of stress on velocity by 6 times more than the traditional bulk waves when the wave velocity and the load are the same direction, and about 10 times more sensitive than the traditional bulk wave when the wave velocity and loads are perpendicular. That means the influence of other factors, such as texture and grain size of the measured sample, would be decreased and the measurement resolution will increase.

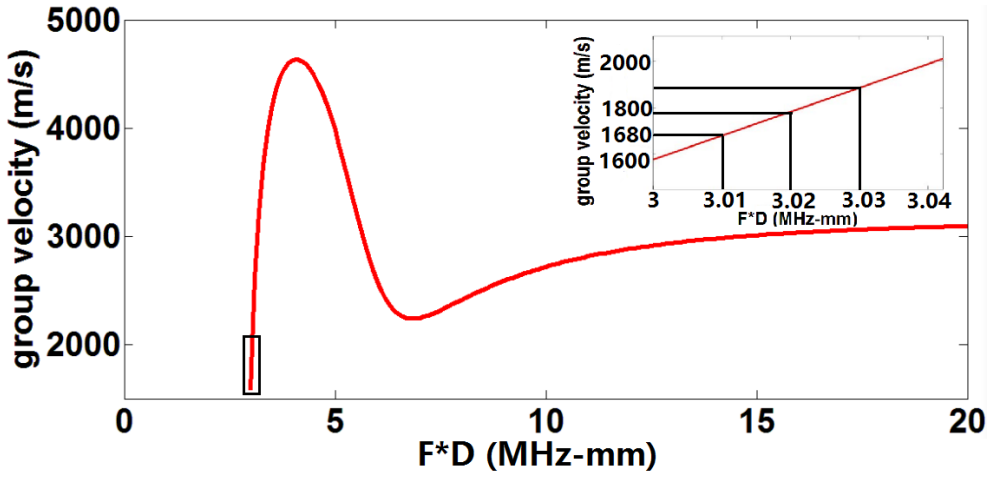

Figure 8.2: Diagram showing operating frequency on dispersion curve.

Theoretically, the resolution for the S_1 Lamb wave is about 10 times more sensitive than the traditional bulk waves by using the same experimental system. The resolution of an experimental system by using the ultrasonic method for characterizing stress is determined by many factors, such as the size of the sample, the distance between incident transducer and receiving transducer, the roughness of the sample surface, the signal processing method, etc. For the experimental system used in this project, the

resolution for stress characterization can reach $\pm$ 3 MPa for the perpendicular configuration and $\pm$ 6 MPa for the parallel configuration.

However, there remain challenges for the higher order Lamb wave method. For example, it is not easy to generate higher order Lamb waves near the cut-off frequency (Fig. 8.2). It is usually a very narrow and highly-dispersive frequency region where the dispersion curve changes sharply. Because of this dispersion characteristic, it is challenging to keep the S_1 Lamb wave near the cut-off frequency. For example if the plate thickness is not sufficiently stable, the Lamb wave velocity can change because of thickness variation rather than because of a change in stress.

Generally speaking, the thickness of the sample should keep as constant as possible, the thickness resolution is determined by both the sample size and the transducer used in the experiment. In real applications, using the S_1 Lamb wave method for stress characterization, it is necessary to monitor the thickness of the sample. If the thickness varies significantly, its influence should be considered when calculating the estimated stress based on the dispersion curve and frequency relationships.

CHAPTER 9. CONCLUSION AND FURTHER WORK

This thesis is focused on enhancing the sensitivity between ultrasound velocity and the stress, using both LCR waves and Lamb waves for stress/load characterization. It is concluded that the sensitivity between the LCR wave and the stress/loads can be enhanced with optimized parameters, and that the sensitivity between the S_1 Lamb wave and stress/load is much greater than for bulk waves.

For the LCR wave method, different parameters have been considered, including the center frequency (F), the aperture (D), the incident angle (α) of the transmitting transducer, and the location of the receiving transducer (L). A detailed directivity analysis for the LCR wave was carried out using both a numerical model and the Orthogonal Experiment method, with results showing that the center frequency (F), the aperture (D), and the incident angle (α) of the transducer all can significantly influence the directivity for the LCR wave.

However, there are other factors that should be considered when using the LCR wave method for stress characterization, including the possible depth of the stress in the sample, because the deeper the stress, the lower the center frequency of the transducer needed to make sure that the wave propagates deep into the sample. For industrial application, all these parameters should be considered and optimized as a group.

Higher order Lamb waves near the cut-off frequency were found to exhibit enhanced sensitive to the stress when compared to bulk waves. Further calculations showed that the S_1 Lamb mode near the cut-off frequency is much more sensitive to stress when compared to the bulk waves, being about 10 times more sensitive when the velocity and the stress are perpendicular, and about 6 times more sensitive when the velocity and the stress are parallel. This suggests a new ultrasonic method for stress characterization.

To verify the numerical results, experiments using a tone burst system were carried out. One challenge for the experiment was to stimulate the stable S_1 mode near the cut-off frequency when the

sample's thickness was not exactly constant, since a change in thickness can lead to an ultrasonic velocity change because of a dispersion relationship, so a thickness monitor is necessary when using the S_1 mode for stress characterization, thickness compensation is needed when the thickness is not stable. In the samples considered no significant effects due to micro-structure variation were observed.

9.1 Further work

So based on the above discussion, further work is suggested as follows:

1. For the LCR wave method, while methods for increasing the sensitivity of the LCR wave have been shown, in industrial applications other factors such as the real depth of the stress must be considered. Therefore, for specific applications a more detailed analysis is needed.

2. With respect to the Lamb wave method for stress characterization, this experimental work has been restricted to applied loads. For residual stress characterization, more experiments should be designed to study residual stress, a much more complex topic.

3. In using the S_1 mode for stress characterization, the thickness of the sample can vary, and monitoring the thickness of the sample is required, and compensation to account for thickness variation is necessary.

4. While currently-used methods are contact methods, non-contact methods, like using air-coupled transducers and Electro Magnetic Acoustic Transducer (EMAT) to enhance detection efficiency, could be considered.

5. The methods described in the thesis for enhancing sensitivity between stress and ultrasound velocity are based on parameter optimizing (for the LCR wave method) and applying new higher order Lamb modes (the S_1 Lamb mode); the acoustoelasticity is not changed. If research could be focused on the physics involved in enhancement of acoustoelasticity relating the stress to ultrasound velocity, a big step in using ultrasonic methods for stress characterization might be possible.

In summary, although methods for enhancing the sensitivity between ultrasound velocity and stress have been described, there are still many remaining challenges for industrial application.

REFERENCES

Allen, D., Cooper, W., Sayers, C., and Silk, M. (1982). *The use of ultrasonics to measure residual stresses. Research Techniques in Nondestructive Testing*. Vol.6, Ed. R.S. Sharpe, Academic Press (Orlando)., pp:151-209.

Altan, T. and Tekkaya, A. E. (2012). *Sheet metal forming: fundamentals*. ASM International.

Anderson, R. and Barkan, C. (2004). Railroad accident rates for use in transportation risk analysis. *Transportation Research Record: Journal of the Transportation Research Board 1863*, pages 88–98.

Association, W. S. (2016). World steel short-rang outlook 2016-2017.

Baird, D. C. (1962). *Experimentation: an introduction to measurement theory and experiment design*. Prentice Hall (New Jersey).

Basatskaya, L. and Ermolov, I. (1981). Theoretical analysis of ultrasonic longitudinal undersurface waves in solid medium. *Sov. J. Nondestruct. Test*, 16(7):524–530.

Belahcene, F. and Lu, J. (2002). Determination of residual stress using critically refracted longitudinal waves and immersion mode. *The Journal of Strain Analysis for Engineering Design*, 37(1):13–20.

Belgroune, D., de Belleval, J. F., and Djelouah, H. (2008). A theoretical study of ultrasonic wave transmission through a fluid–solid interface. *Ultrasonics*, 48(3):220–230.

Benson, R. and Raelson, V. (1959). Acoustoelasticity. *Product Engineering*, 30(29):56–9.

Bevington, P. R., Robinson, D. K., Blair, J. M., Mallinckrodt, A. J., and McKay, S. (1993). Data reduction and error analysis for the physical sciences. *Computers in Physics*, 7(4):415–416.

Björklund, S. (2003). *A survey and comparison of time-delay estimation methods in linear systems*. PhD thesis, Linköping University.

Bray, D. E. (2002). Ultrasonic stress measurement and material characterization in pressure vessels, piping, and welds. *Journal of Pressure Vessel Technology*, 124(3):326–335.

Bray, D. E., Egle, D. M., and Reiter, L. (1978). Rayleigh wave dispersion in the cold-worked layer of used railroad rail. *The Journal of the Acoustical Society of America*, 64(3):845–851.

Bray, D. E. and Junghans, P. (1995). Application of the lcr ultrasonic technique for evaluation of post-weld heat treatment in steel plates. *NDT & E International*, 28(4):235–242.

Bray, D. E. and Stanley, R. K. (1996). *Nondestructive evaluation: a tool in design, manufacturing and service*. CRC Press (Boca Raton).

Bray, D. E. and Tang, W. (2001). Subsurface stress evaluation in steel plates and bars using the lcr ultrasonic wave. *Nuclear Engineering and Design*, 207(2):231–240.

Breazeale, M., Cantrell, J. H., and Heyman, J. S. (1981). Ultrasonic wave velocity and attenuation measurements. *Methods in experimental physics*, 19:67–135.

Buenos, A. A., dos Santos, A. A., Pereira, P., and Santos, C. S. (2012). Effect of mean grain size in the time of flight for lcr waves. In *Proceedings ASME 2012 International Mechanical Engineering Congress and Exposition*, pages 63–69. American Society of Mechanical Engineers.

Buenos, A. A., dos Santos Junior, A. A., Rodrigues, A. R., and Tokimatsu, R. C. (2013). Application of acoustoelasticity to measure the stress generated by milling in astm a36 steel plates. *Journal of the Brazilian Society of Mechanical Sciences and Engineering*, 35(4):525–536.

Bulckaen, V. and Gucci, N. (1975). Device for the determination of biaxial-symmetrical residual stresses in metallic, disk-shaped specimens. *Review of Scientific Instruments*, 46(10):1402–1408.

Chaki, S., Ke, W., and Demouveau, H. (2013). Numerical and experimental analysis of the critically refracted longitudinal beam. *Ultrasonics*, 53(1):65–69.

Chen, F. and Wilcox, P. D. (2007). The effect of load on guided wave propagation. *Ultrasonics*, 47(1):111–122.

Chen, Y., Zhang, J., Yang, C., and Niu, B. (2007). The workspace mapping with deficient-dof space for the puma 560 robot and its exoskeleton arm by using orthogonal experiment design method. *Robotics and Computer-Integrated Manufacturing*, 23(4):478–487.

Chern, E. and Heyman, J. (1982). Ultrasonic measurement of axial stress. *Journal of Testing and Evaluation*, 10(5):202–211.

Clark, A. and Moulder, J. (1985). Residual stress determination in aluminium using electromagnetic acoustic transducers. *Ultrasonics*, 23(6):253–259.

Clark, A. V., Schramm, R. E., Schaps, S. R., and Filla, B. (1995). Safety assessment of railroad wheels through roll-by detection of tread cracks. In *Proceedings-SPIE the international society for optical engineering, Vol. 2458*, pages 109–119. SPIE international society for optical.

Crecraft, D. (1967). The measurement of applied and residual stresses in metals using ultrasonic waves. *Journal of Sound and Vibration*, 5(1):173–192.

Crecraft, D. (1968). Ultrasonic measurement of stresses. *Ultrasonics*, 6(2):117–121.

Cui, W., Li, X., Zhou, S., and Weng, J. (2007). Investigation on process parameters of electrospinning system through orthogonal experimental design. *Journal of Applied Polymer Science*, 103(5):3105–3112.

Delsanto, P. and Clark, A. (1987). Rayleigh wave propagation in deformed orthotropic materials. *The Journal of the Acoustical Society of America*, 81(4):952–960.

Deputat, J., Szelazek, J., and Kwaszczyhska-Klimek, A. M. (1992). Experiences in ultrasonic measurement of rail residual stresses. *Residual Stress in Rails, Vol.1, Ed. O. Orringer, J. Orkisz and Z. Swiderski, Kluwer Academic Publishers (The Netherlands)*, pages pp:169–183.

Dieck, R. H. (2007). *Measurement uncertainty: methods and applications*. ISA, (NC).

Dowell, E., Gorman, G., and Smith, D. (1977). Acoustoelasticity: general theory, acoustic natural modes and forced response to sinusoidal excitation, including comparisons with experiment. *Journal of Sound and vibration*, 52(4):519–542.

Duqennoy, M., Ouaftouh, M., and Ourak, M. (1999). Determination of stresses in aluminium alloy using optical detection of rayleigh waves. *Ultrasonics*, 37(5):365–372.

Duquennoy, M., Ouaftouh, M., Ourak, M., and Jenot, F. (2002). Theoretical determination of rayleigh wave acoustoelastic coefficients: comparison with experimental values. *Ultrasonics*, 39(8):575–583.

Duquennoy, M., Ouaftouh, M., Qian, M., Jenot, F., and Ourak, M. (2001). Ultrasonic characterization of residual stresses in steel rods using a laser line source and piezoelectric transducers. *NDT & E International*, 34(5):355–362.

Egle, D. (1980). Application of the acoustoelastic effect to rail stress measurement. In *Ultrasonic Materials Characterization: Proceedings of the First International Symposium on Ultrasonic Materials Characterization Held at the National Bureau of Standards, Gaithersburg, Md., June 7-9, 1978*, volume 596, pages 213–225. US Department of Commerce, National Bureau of Standards.

Egle, D. and Bray, D. (1976). Measurement of acoustoelastic and third-order elastic constants for rail steel. *The Journal of the Acoustical Society of America*, 60(3):741–744.

Ensminger, D. and Bond, L. J. (2011). *Ultrasonics: fundamentals, technologies, and applications*. CRC Press (Boca Raton).

Etter, T., Papakyriacou, M., Schulz, P., and Uggowitzer, P. (2003). Physical properties of graphite/aluminium composites produced by gas pressure infiltration method. *Carbon*, 41(5):1017–1024.

Fraga, R., Santos, A., and Andrino, M. (2008). Temperature effect on the measurement of stresses in pipelines using ultrasonic lcr waves. In *Proceedings ASME 2008 International Mechanical Engineering Congress and Exposition*, pages 361–367. American Society of Mechanical Engineers.

Gachi, S., Belahcene, F., and Boubenider, F. (2009). Residual stresses in 7108 aluminium alloy sheets joined by friction stir welding. *Nondestructive Testing and Evaluation*, 24(3):301–309.

Gandhi, N. (2010). *Determination of dispersion curves for acoustoelastic Lamb wave propagation*. PhD thesis, Georgia Institute of Technology.

Gandhi, N., Michaels, J. E., and Lee, S. J. (2012). Acoustoelastic lamb wave propagation in biaxially stressed plates. *The Journal of the Acoustical Society of America*, 132(3):1284–1293.

Gauthier, J., Krause, T., and Atherton, D. (1998). Measurement of residual stress in steel using the magnetic barkhausen noise technique. *NDT & E International*, 31(1):23–31.

González, A. G. and Herrador, M. Á. (2007). A practical guide to analytical method validation, including measurement uncertainty and accuracy profiles. *Trends in Analytical Chemistry, TrAC*, 26(3):227–238.

Greving, D., Rybicki, E., and Shadley, J. (1994). Through-thickness residual stress evaluations for several industrial thermal spray coatings using a modified layer-removal method. *Journal of Thermal Spray Technology*, 3(4):379.

Hamada, M. and Shibuya, T. (1995). Time frequency analysis of dispersive waves by means of wavelet transform. *Journal of Applied Mechanics*, 62:841.

Hayes, M. and Rivlin, R. S. (1961). Surface waves in deformed elastic materials. *Archive for Rational Mechanics and Analysis*, 8(1):358–380.

Hirao, M., Aoki, K., and Fukuoka, H. (1987). Texture of polycrystalline metals characterized by ultrasonic velocity measurements. *The Journal of the Acoustical Society of America*, 81(5):1434–1440.

Hirao, M., Fukuoka, H., and Hori, K. (1981). Acoustoelastic effect of rayleigh surface wave in isotropic material. *Journal of Applied Mechanics*, 48(1):119–124.

Hirao, M., Ogi, H., and Fukuoka, H. (1993). Resonance emat system for acoustoelastic stress measurement in sheet metals. *Review of Scientific Instruments*, 64(11):3198–3205.

Hsu, N. N. (1974). Acoustical birefringence and the use of ultrasonic waves for experimental stress analysis. *Experimental Mechanics*, 14(5):169–176.

Huang, K., Chen, S., Yuan, X., and Zhou, Z. (2004). Neural network optimal design based on orthogonal experiment method. *Systems Engineering-Theory Methodology Application*, 13(3):272–275.

Hughes, D. S. and Kelly, J. (1953). Second-order elastic deformation of solids. *Physical Review*, 92(5):1145–1149.

Hung, Y. (1982). Shearography: a new optical method for strain measurement and nondestructive testing. *Optical Engineering*, 21(3):391–395.

Husson, D. (1985). A perturbation theory for the acoustoelastic effect of surface waves. *Journal of Applied Physics*, 57(5):1562–1568.

Iwashimizu, Y. and Kobori, O. (1978). The rayleigh wave in a finitely deformed isotropic elastic material. *The Journal of the Acoustical Society of America*, 64(3):910–916.

Javadi, Y., Akhlaghi, M., and Najafabadi, M. A. (2013). Using finite element and ultrasonic method to evaluate welding longitudinal residual stress through the thickness in austenitic stainless steel plates. *Materials & Design*, 45:628–642.

Kandil, F., Lord, J., Fry, A., and Grant, P. (2001). A review of residual stress measurement methods. *A Guide to Technique Selection, National Physical Laboratory (UK), Report MATC (A)*, 4.

Karabutov, A., Devichensky, A., Ivochkin, A., Lyamshev, M., Pelivanov, I., Rohadgi, U., Solomatin, V., and Subudhi, M. (2008). Laser ultrasonic diagnostics of residual stress. *Ultrasonics*, 48(6):631–635.

Keil, S. (1992). Experimental determination of residual stresses with the ring-core method and an on-line measuring system. *Experimental Techniques*, 16(5):17–24.

Kino, G., Barnett, D., Grayeli, N., Herrmann, G., Hunter, J., Ilić, D., Johnson, G., King, R., Scott, M., Shyne, J., et al. (1980). Acoustic measurements of stress fields and microstructure. *Journal of Nondestructive Evaluation*, 1(1):67–77.

Langenberg, K., Fellinger, P., and Marklein, R. (1990). On the nature of the so-called subsurface longitudinal wave and/or the surface longitudinal creeping wave. *Research in Nondestructive Evaluation*, 2(2):59–81.

Lanza di Scalea, F., Rizzo, P., and Seible, F. (2003). Stress measurement and defect detection in steel strands by guided stress waves. *Journal of Materials in Civil Engineering*, 15(3):219–227.

Lee, S., Coan, B., and Bouxsein, M. (1997). Tibial ultrasound velocity measured in-situ predicts the material properties of tibial cortical bone. *Bone*, 21(1):119–125.

Lematre, M., Feuillard, G., Delaunay, T., and Lethiecq, M. (2006). Modeling of ultrasonic wave propagation in integrated piezoelectric structures under residual stress. *IEEE Transactions on Ultrasonics, Ferroelectrics, and Frequency Control*, 53(4):685–696.

Leon-Salamanca, T. and Bray, D. (1996). Residual stress measurement in steel plates and welds using critically refracted longitudinal (lcr) waves. *Journal of Research in Nondestructive Evaluation*, 7(4):169–184.

Lu, H., Liu, X., Yang, J., Zhang, S., and Fang, H. (2008). Ultrasonic stress evaluation on welded plates with lcr wave. *Science and Technology of Welding and Joining*, 13(1):70–74.

Ma, C.-H., Huang, J.-H., and Chen, H. (2002). Residual stress measurement in textured thin film by grazing-incidence x-ray diffraction. *Thin Solid Films*, 418(2):73–78.

Matsushima, K. and Shimobaba, T. (2009). Band-limited angular spectrum method for numerical simulation of free-space propagation in far and near fields. *Optics Express*, 17(22):19662–19673.

Murayam, R. and Misumi, K. (2006). Development of a non-contact stress measurement system during tensile testing using the electromagnetic acoustic transducer for a lamb wave. *NDT & E International*, 39(4):299–303.

Murnaghan, F. D. (1937). Finite deformations of an elastic solid. *American Journal of Mathematics*, 59(2):235–260.

Musgrave, M. (1954). On the propagation of elastic waves in aeolotropic media. ii. media of hexagonal symmetry. In *Proceedings of the Royal Society of London A: Mathematical, Physical and Engineering Sciences*, volume 226, pages 356–366.

Musgrave, M. J. (1970). *Crystal acoustics: Introduction to the study of elastic waves and vibrations in crystals*. Holden-Day (San Fransisco).

Nayfeh, A. H. and Chimenti, D. E. (1989). Free wave propagation in plates of general anisotropic media. In *Review of Progress in Quantitative Nondestructive Evaluation (QNDE). Vol.8A, Eds. D. O. Thompson and D. E. Chimenti*, pages 181–188, Plenum (New York).

Niethammer, M., Jacobs, L. J., Qu, J., and Jarzynski, J. (2001). Time-frequency representations of lamb waves. *The Journal of the Acoustical Society of America*, 109(5):1841–1847.

Noronha, P., Chapman, J., and Wert, J. (1973). Residual stress measurement and analysis using ultrasonic techniques. *Journal of Testing and Evaluation*, 1(3):209–214.

Palanichamy, P., Joseph, A., Jayakumar, T., and Raj, B. (1995). Ultrasonic velocity measurements for estimation of grain size in austenitic stainless steel. *NDT & E International*, 28(3):179–185.

Palanichamy, P., Vasudevan, M., and Jayakumar, T. (2009). Measurement of residual stresses in austenitic stainless steel weld joints using ultrasonic technique. *Science and Technology of Welding and Joining*, 14(2):166–171.

Pao, Y.-H. and Gamer, U. (1985). Acoustoelastic waves in orthotropic media. *The Journal of the Acoustical Society of America*, 77(3):806–812.

Pao, Y.-H., Sachse, W., and Fukuoka, H. (1984). *Acoustoelasticity and ultrasonic measurement of residual stress, Physical Acoustics, vol. 17*. Ed. Mason, W and Thurston. R, Academic Press (Orlando).

Parrilla, M., Anaya, J., and Fritsch, C. (1991). Digital signal processing techniques for high accuracy ultrasonic range measurements. *IEEE Transactions on Instrumentation and Measurement*, 40(4):759–763.

Pau, A. and di Scalea, F. L. (2015). Nonlinear guided wave propagation in prestressed plates. *The Journal of the Acoustical Society of America*, 137(3):1529–1540.

Pei, C. and Demachi, K. (2010). Numerical simulation of residual stress measurement with acoustic wave. *E-Journal of Advanced Maintenance*, 2011(2):160–167.

Pei, N. and Bond, L. J. (2015). Acoustoelastic lamb wave analysis in thin plates. In *Proceedings 2015 IEEE Far East NDT New Technology & Application Forum (FENDT)*, pages 149–153.

Pei, N. and Bond, L. J. (2016). Higher order acoustoelastic lamb wave propagation in stressed plates. *The Journal of the Acoustical Society of America*, 140(5):3834–3843.

Prevéy, P. S. and Cammett, J. (2001). Low cost corrosion damage mitigation and improved fatigue performance of low plasticity burnished 7075-t6. *Journal of Materials Engineering and Performance*, 10(5):548–555.

Qozam, H., Chaki, S., Bourse, G., Robin, C., Walaszek, H., and Bouteille, P. (2010). Microstructure effect on the lcr elastic wave for welding residual stress measurement. *Experimental Mechanics*, 50(2):179–185.

Qu, J. and Liu, G. (1998). Effects of residual stress on guided waves in layered media. In *Review of Progress in Quantitative Nondestructive Evaluation (QNDE). Eds. D. O. Thompson and D. E. Chimenti*, volume 17, pages 1635–1642, Plenum Press.

Rabinovich, S. G. and Rabinovich, M. (2010). *Evaluating measurement accuracy*. Springer.

Reimers, W., Pyzalla, A., Broda, M., Brusch, G., Dantz, D., Schmackers, T., Liss, K.-D., and Tschentscher, T. (1999). The use of high-energy synchrotron diffraction for residual stress analyses. *Journal of Materials Science Letters*, 18(7):581–583.

Robinson, A., Dulieu-Barton, J., Quinn, S., and Burguete, R. (2009). A review of residual stress analysis using thermoelastic techniques. In *Journal of Physics: Conference Series*, volume 181. Paper 012029. IOP Publishing.

Rose, J. L. (2004). *Ultrasonic waves in solid media*. Cambridge University Press (Cambridge).

Rossini, N., Dassisti, M., Benyounis, K., and Olabi, A. (2012). Methods of measuring residual stresses in components. *Materials & Design*, 35:572–588.

Roylance, D. (2001). Stress-strain curves. *Massachusetts Institute of Technology study, Cambridge*.

Salama, K. and Ling, C. (1980). The effect of stress on the temperature dependence of ultrasonic velocity. *Journal of Applied Physics*, 51(3):1505–1509.

Santos, A. A., Haddad Andrino, M., Bray, D. E., and Trevisan, R. E. (2008). Evaluation of stresses generated by welding in api 5l x65 steel using acoustoelasticity. *Materials Evaluation*, 66(8):858–864.

Schajer, G. (1988). Measurement of non-uniform residual stresses using the hole-drilling method. part istress calculation procedures. *Journal of Engineering Materials and Technology*, 110(4):338–343.

Schajer, G. S. (2013). *Practical residual stress measurement methods*. John Wiley & Sons (Chichester).

Shadley, J., Rybicki, E., and Shealy, W. (1987). Application guidelines for the parting out step in a through thickness residual stress measurement procedure. *Strain*, 23(4):157–166.

Shi, F., Michaels, J. E., and Lee, S. J. (2013). In situ estimation of applied biaxial loads with lamb waves. *The Journal of the Acoustical Society of America*, 133(2):677–687.

Song, W., Pan, Q., Xu, C., Li, X., and Liu, H. (2013). Benchmark of residual stress for ultrasonic nondestructive testing. In *Proceddings 2013 IEEE Far East NDT New Technology & Application Forum (FENDT)*, pages 73–76.

Svilainis, L. (2012). Review of high resolution time of flight estimation techniques for ultrasonic signals. In *2013 International Conference NDT, Telford, UK*, pages 1–12.

Svilainis, L. and Dumbrava, V. (2008). Analysis of the interpolation techniques for time-of-flight estimation. *Ultragarsas [Ultrasound]*, 63(4):25–29.

Takahashi, S. and Motegi, R. (2015). Measurement of third-order elastic constants and applications to loaded structural materials. *SpringerPlus*, 4(1):325.

Tanala, E., Bourse, G., Fremiot, M., and De Belleval, J. (1995). Determination of near surface residual stresses on welded joints using ultrasonic methods. *NDT & E International*, 28(2):83–88.

Thurston, R. and Brugger, K. (1964). Third-order elastic constants and the velocity of small amplitude elastic waves in homogeneously stressed media. *Physical Review*, 133(6A):A1604.

Toupin, R. and Bernstein, B. (1961). Sound waves in deformed perfectly elastic materials. acoustoelastic effect. *The Journal of the Acoustical Society of America*, 33(2):216–225.

Treuting, R. and Read Jr, W. (1951). A mechanical determination of biaxial residual stress in sheet materials. *Journal of Applied Physics*, 22(2):130–134.

Tsai, Y.-T. and Zhu, J. (2012). Simulation and experiments of airborne zero-group-velocity lamb waves in concrete plate. *Journal of Nondestructive Evaluation*, 31(4):373–382.

Wang, L. and Yuan, F. (2007). Group velocity and characteristic wave curves of lamb waves in composites: Modeling and experiments. *Composites Science and Technology*, 67(7):1370–1384.

Welzel, U., Ligot, J., Lamparter, P., Vermeulen, A., and Mittemeijer, E. (2005). Stress analysis of polycrystalline thin films and surface regions by x-ray diffraction. *Journal of Applied Crystallography*, 38(1):1–29.

Wert, J. and Noronha, P. (1975). An ultrasonic technique for the measurement of residual stress. *Journal of Testing and Evaluation*, 3(2):147–152.

Withers, P. and Bhadeshia, H. (2001). Residual stress. part 1–measurement techniques. *Materials Science and Technology*, 17(4):355–365.

Wormley, S., Forouraghi, K., Li, Y., Thompson, R., and Papadakis, E. (1990). Application of a fourier transform-phase-slope technique to the design of an instrument for the ultrasonic measurement of texture and stress. In *Review of Progress in Quantitative Nondestructive Evaluation (QNDE). Eds. D. O. Thompson and D. E. Chimenti, Plenun Press*, volume 9A, pages 951–958.

Wormley, S. and Thompson, R. B. (1989). Development of a breadboard instrument for the ultrasonic measurement of stress. In *Review of Progress in Quantitative Nondestructive Evaluation (QNDE). Eds. D. O. Thompson and D. E. Chimenti, Plenun Press*, volume 8A, pages 1119–1125.

Yelbay, H. I., Cam, I., and Gür, C. H. (2010). Non-destructive determination of residual stress state in steel weldments by magnetic barkhausen noise technique. *NDT & E International*, 43(1):29–33.

Zhang, L. and Wu, X. (2006). On the application of cross correlation function to subsample discrete time delay estimation. *Digital Signal Processing*, 16(6):682–694.

APPENDIX A. ULTRASOUND VELOCITY AND STRESS RELATIONSHIP

In order to establish the relationship between wave velocity and higher order elastic constants, the wave governing equations in prestressed media are needed. Toupin and Berstein (Toupin and Bernstein 1961) defined three states (natural state: the natural state without stress; initial state: the deformed state with stress; final state: wave motion added to the initial state) for determining the acoustoelasitc constants. The following contents are following their definition.

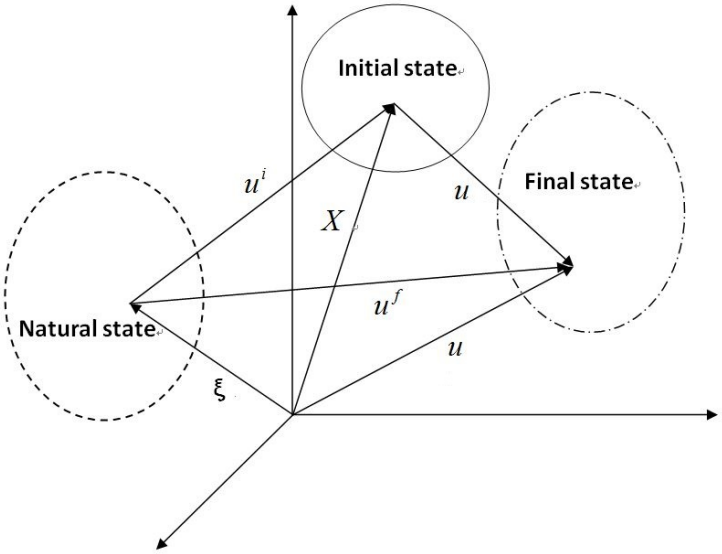

Figure A.1: Coordinates describing a material point at the natural ($\boldsymbol{\xi}$), initial ($\boldsymbol{X}$), and final ($\boldsymbol{x}$) configuration of a predeformed body.

As is shown in Fig. A.1, a physical particle in the natural, initial and final state is expressed by a superscript label 0, i , and f respectively. The position of a particle in the body at natural, initial and final states are expressed by the vector $\boldsymbol{\xi}$, $\boldsymbol{X}$and $\boldsymbol{x}$ respectively. The components of $\boldsymbol{\xi}$ in different directions refer to natural coordinate denoted by Greek subscripts; the components of $\boldsymbol{X}$ refer to initial coordinate denoted by upper case Roman subscripts; the components of $\boldsymbol{x}$ refer to the final coordinate

denoted by lower case Roman subscripts. Then in these three different configurations the vectors can be expressed as: $\boldsymbol{\xi_\alpha}$, $\boldsymbol{X_J}$ and $\boldsymbol{x_j}$ $(\alpha, J, j = 1, 2, 3)$.

From the natural to the initial states, the deformation is static and it can be expressed as $\mathbf{u}^i$; from the initial to the final states the displacement is written as $\mathbf{u}^f$. These vectors related to the position vectors can be written as:

$$\begin{aligned} \mathbf{u}^i(\boldsymbol{\xi}) &= \mathbf{X} - \boldsymbol{\xi} \\ \mathbf{u}^f(\boldsymbol{\xi}, t) &= \mathbf{x} - \boldsymbol{\xi} \end{aligned} \tag{A.1}$$

Then the displacement from initial to final state can be written as:

$$\mathbf{u}(\boldsymbol{\xi}, t) = \mathbf{x} - \mathbf{X} = \mathbf{u}^f - \mathbf{u}^i \tag{A.2}$$

The deformation gradient tensor $\mathbf{F}$ can be written as:

$$\mathbf{F} = \frac{\partial \mathbf{x}}{\partial \boldsymbol{\xi}} = \mathbf{I} + \frac{\partial \mathbf{u}^f}{\partial \boldsymbol{\xi}} \tag{A.3}$$

Where $\mathbf{I}$ is the unit tensor.

The form of component of $\mathbf{F}$ can be written as:

$$F_{ij} = \frac{\partial x_i}{\partial \xi_j} = \delta_{ij} + \frac{\partial u_i^f}{\partial \xi_j} \tag{A.4}$$

Where δ_{ij} is Kronecker unit tensor, $\delta_{ij} = 1\ (i = j), \delta_{ij} = 0\ (i \neq j)$.

For a infinitesimal element $d\boldsymbol{\xi}$, after transformation is shown as $d\mathbf{x}$. The difference of these two squares can describe the absolute value change of the length:

$$d\mathbf{x}^2 - d\boldsymbol{\xi}^2 = d\mathbf{x}d\mathbf{x} - d\boldsymbol{\xi}d\boldsymbol{\xi} = 2d\boldsymbol{\xi}Ed\mathbf{a} \tag{A.5}$$

Where $\mathbf{E}$ is Lagrangian strain tensor.

The relationship between Lagrangian strain tensor $\mathbf{E}$ and deformation gradient tensor $\mathbf{F}$ can be written as:

$$\mathbf{E} = \frac{1}{2}(\mathbf{F}^T\mathbf{F} - \mathbf{I}) \tag{A.6}$$

Where $\mathbf{F}^T$ is the transfposed tensor of $\mathbf{F}$.

The total strain (E_{ij}) comprises the strain in the deformed status (E^i_{ij}) plus the strain from wave motion ($\bar{E_{ij}}$), the total strain can be written as:

$$E_{ij} = \frac{1}{2}(\frac{\partial x_\alpha}{\partial a_i}\frac{\partial x_\alpha}{\partial a_j} - \delta_{ij}) \tag{A.7}$$

Where

$$E_{ij} = E^i_{ij} + \bar{E_{ij}}; \tag{A.8}$$

Considering Eq. A.1 and Eq. A.2, Eq. A.7 can be rewritten as:

$$\begin{aligned} E_{ij} &= \frac{1}{2}(\frac{\partial x_\alpha}{\partial \xi_i}\frac{\partial x_\alpha}{\partial \xi_j} - \delta_{ij}) \\ &= \frac{1}{2}((\frac{\partial(\xi_\alpha + u^i_\alpha)}{\partial \xi_i} + \frac{\partial u_\alpha}{\partial \xi_i})(\frac{\partial(\xi_\alpha + u^i_\alpha)}{\partial \xi_j} + \frac{\partial u_\alpha}{\partial \xi_j}) - \delta_{ij}) \\ &= \frac{1}{2}(\frac{\partial(\xi_\alpha + u^i_\alpha)}{\partial \xi_i}\frac{\partial(\xi_\alpha + u^i_\alpha)}{\partial \xi_j} - \delta_{ij}) + \frac{1}{2}(\frac{\partial(\xi_\alpha + u^i_\alpha)}{\partial \xi_i}\frac{\partial u_\alpha}{\partial \xi_j} + \frac{\partial(\xi_\alpha + u^i_\alpha)}{\partial \xi_j}\frac{\partial u_\alpha}{\partial \xi_i} + (\frac{\partial u_\alpha}{\partial \xi_i})(\frac{\partial u_\alpha}{\partial \xi_j})) \end{aligned} \tag{A.9}$$

The first part in Eq. A.9 refers to E^i_{ij} (the strain in the deformed status) while the second part refers to $\bar{E_{ij}}$ (wave motion).

Omitting the higher order term $(\frac{\partial u_\alpha}{\partial \xi_i})(\frac{\partial u_\alpha}{\partial \xi_j})$, the $\bar{E_{ij}}$ can be written as:

$$\begin{aligned} \bar{E_{ij}} &\approx \frac{1}{2}[(\delta_{\alpha i} + \frac{\partial u^i_\alpha}{\partial \xi_i})\frac{\partial u_\alpha}{\partial X_\beta}\frac{\partial X_\beta}{\partial \xi_j} + (\delta_{\alpha j} + \frac{\partial u^i_\alpha}{\partial \xi_j})\frac{\partial u_\alpha}{\partial X_\beta}\frac{\partial X_\beta}{\partial \xi_i}] \\ &= \frac{1}{2}[(\delta_{\alpha i} + \frac{\partial u^i_\alpha}{\partial \xi_i})(\delta_{\beta j} + \frac{\partial u^i_\beta}{\partial \xi_j}) + (\delta_{\alpha i} + \frac{\partial u^i_\alpha}{\partial \xi_j})(\delta_{\beta i} + \frac{\partial u^i_\beta}{\partial \xi_i})]\frac{\partial u_\alpha}{\partial X_\beta} \end{aligned} \tag{A.10}$$

Considering the symmetry of Eq. A.10, it can be simplified as:

$$\bar{E_{ij}} = \frac{1}{2}(\delta_{\alpha i} + \frac{\partial u^i_\alpha}{\partial a_i})(\delta_{\beta j} + \frac{\partial u^i_\beta}{\partial a_j})(\frac{\partial u_\alpha}{\partial X_\beta} + \frac{\partial u_\beta}{\partial X_\alpha}) \tag{A.11}$$

Following Eq. A.11, $\bar{E_{11}}$, $\bar{E_{22}}$, $\bar{E_{33}}$, $\bar{E_{12}}$, $\bar{E_{13}}$, $\bar{E_{23}}$ can be obtained.

For stress expression, it should begin with strain energy:

$$\rho\phi = A_0 I_1 + \frac{(\lambda + 2\mu)}{2}I_1^2 - 2\mu I_2 + \frac{(l+m)}{3}I_1^3 - 2mI_1I_2 + nI_3 \tag{A.12}$$

Where $\rho\phi$ is the unit energy for the deformed isotropic solid, A_0 is the parameter; λ and μ are second order elastic constants (Lame constants), l, m and n are third order elastic constants (Murnaghan's third-order elastic constants). Three invariants I_1, I_2 and I_3 are defined as:

$$\begin{aligned} I_1 &= E^i_{11} + E^i_{22} + E^i_{33} \\ I_2 &= \begin{vmatrix} E^i_{22} & E^i_{23} \\ E^i_{32} & E^i_{33} \end{vmatrix} + \begin{vmatrix} E^i_{33} & E^i_{31} \\ E^i_{13} & E^i_{11} \end{vmatrix} + \begin{vmatrix} E^i_{11} & E^i_{12} \\ E^i_{21} & E^i_{22} \end{vmatrix} \\ I_3 &= \begin{vmatrix} E^i_{11} & E^i_{12} & E^i_{13} \\ E^i_{21} & E^i_{22} & E^i_{23} \\ E^i_{31} & E^i_{32} & E^i_{33} \end{vmatrix} \end{aligned} \tag{A.13}$$

The relationship between stress and the unit energy can be shown as:

$$T_{ij} = J_{i\alpha} \frac{\partial(\rho_0 \phi)}{\partial E^i_{\alpha j}} \tag{A.14}$$

Where $J_{i\alpha}$ is the Jacobian matrix.

Following Eq. A.14,

$$\begin{aligned} \frac{\partial(\rho_0\phi)}{\partial E^i_{ij}} =& ((\lambda + 2\mu) I_1 + (l + 2m) I_1^2 - 2m I_2) \frac{\partial I_1}{\partial E^i_{ij}} \\ & - 2(\mu + m I_1) \frac{\partial I_2}{\partial E^i_{ij}} + n \frac{\partial I_3}{\partial E^i_{ij}} \end{aligned} \tag{A.15}$$

Where

$$\begin{aligned} \frac{\partial I_1}{\partial E^i_{11}} &= 1 \\ \frac{\partial I_1}{\partial E^i_{23}} &= 0 \\ \frac{\partial I_2}{\partial E^i_{11}} &= E^i_{22} + E^i_{33} = I_1 - E^i_{11} \\ \frac{\partial I_2}{\partial E^i_{23}} &= -E^i_{32} \\ \frac{\partial I_3}{\partial E^i_{11}} &= E^i_{22} E^i_{33} - E^i_{23} E^i_{32} \\ \frac{\partial I_3}{\partial E^i_{23}} &= E^i_{12} E^i_{31} - E^i_{11} E^i_{32} = \begin{vmatrix} E^i_{11} & E^i_{12} \\ E^i_{31} & E^i_{32} \end{vmatrix} \end{aligned} \tag{A.16}$$

Following Eq. A.15, $\frac{\partial(\rho\phi)}{\partial E^i_{11}}$, $\frac{\partial(\rho\phi)}{\partial E^i_{22}}$, $\frac{\partial(\rho\phi)}{\partial E^i_{33}}$, $\frac{\partial(\rho\phi)}{\partial E^i_{23}}$, $\frac{\partial(\rho\phi)}{\partial E^i_{31}}$, $\frac{\partial(\rho\phi)}{\partial E^i_{12}}$ can be obtained.

The total stress (T_{ij}) comprises the stress in the deformed status (T^i_{ij}) plus the stress from wave motion ($\bar{T_{ij}}$), the total stress can be written as:

$$T_{ij} = T^i_{ij} + \bar{T_{ij}} \tag{A.17}$$

Considering Eq. A.14,

$$\begin{aligned} T_{ij} &= J_{i\alpha}\frac{\partial(\rho_0\phi)}{\partial E^i_{\alpha j}} \\ &= (J^i_{i\alpha} + \bar{J_{i\alpha}})(\frac{\partial(\rho\phi)^i}{\partial E^i_{\alpha j}} + \frac{\partial(\bar{\rho\phi})}{\partial E^i_{\alpha j}}) \\ &= J^i_{i\alpha}\frac{\partial(\rho_0\phi)^i}{\partial E^i_{\alpha j}} + \bar{J_{i\alpha}}\frac{\partial(\rho_0\phi)^i}{\partial E^i_{\alpha j}} + J^i_{\alpha}\frac{\partial(\bar{\rho_0\phi})}{\partial E^i_{\alpha j}} + \bar{J_{i\alpha}}\frac{\partial(\bar{\rho_0\phi})}{\partial E^i_{\alpha j}} \end{aligned} \tag{A.18}$$

The elements of the Jacobian matrix can be written as:

$$\begin{aligned} J_{i\alpha} &= \frac{\partial x_i}{\partial \xi_i} \\ J^i_{i\alpha} &= \frac{\partial X_i}{\partial \xi_\alpha} = \frac{\partial(\xi_i + u^i_i)}{\partial \xi_\alpha} \\ \bar{J^i_{i\alpha}} &= J_{i\alpha} - J^i_{i\alpha} = \frac{\partial x_i}{\partial \xi_\alpha} - \frac{\partial X_i}{\partial \xi_\alpha} = \frac{\partial u_i}{\partial \xi_\alpha} \end{aligned} \tag{A.19}$$

Considering Eq. A.18 and omitting higher order term $\bar{J_{i\alpha}}\frac{\partial(\bar{\rho_0\phi})}{\partial E^i_{\alpha j}}$, the expression for T^i_{ij} can be written as:

$$T^i_{ij} \approx \bar{J_{i\alpha}}\frac{\partial(\rho_0\phi)^i}{\partial E^i_{\alpha j}} + J^i_{\alpha}\frac{\partial(\bar{\rho_0\phi})}{\partial E^i_{\alpha j}} \tag{A.20}$$

Considering Eq. A.20, T^i_{11}, T^i_{22}, T^i_{33}, T^i_{23}, T^i_{12} and T^i_{31} can be obtained.

Considering the equation of motion for the elastic wave:

$$\rho\frac{\partial^2 u_i}{\partial t^2} = \frac{\partial T^i_{i\alpha}}{\partial \xi_\alpha} = \frac{\partial T^i_{i\alpha}}{\partial X_\beta}\frac{\partial X_\beta}{\partial \xi_\alpha} \tag{A.21}$$

The possible solution can be written as:

$$u_i = Aexpi(\omega t - kX_i) \tag{A.22}$$

Where A is the amplitude, ω is the angular frequency, k is the wave number.

For the longitudinal wave, the equation of motion can be written as:

$$\rho\frac{\partial^2 u_1}{\partial t^2} = \frac{\partial T^i_{1\alpha}}{\partial X_\beta}\frac{\partial X_\beta}{\partial \xi_\alpha} = \frac{\partial T^i_{11}}{\partial X_\beta}\frac{\partial X_\beta}{\partial \xi_1} + \frac{\partial T^i_{12}}{\partial X_\beta}\frac{\partial X_\beta}{\partial \xi_2} + \frac{\partial T^i_{13}}{\partial X_\beta}\frac{\partial X_\beta}{\partial \xi_3} \tag{A.23}$$

Expanding Eq. A.23:

$$\rho\frac{\partial^2 u_1}{\partial t^2} = \frac{\partial T^i_{11}}{\partial X_1}(1+\frac{\partial u^i_1}{\partial \xi_1}) + \frac{\partial T^i_{12}}{\partial X_\beta}(1+\frac{\partial u^i_2}{\partial \xi_2}) + \frac{\partial T^i_{13}}{\partial X_\beta}(1+\frac{\partial u^i_3}{\partial \xi_3}) \tag{A.24}$$

Considering Eq. A.10, Eq. A.15 and Eq. A.21, Eq. A.23 can be rewritten as:

$$\begin{aligned}\rho_0 V^2_{11} &= (1+E^i_1)(\lambda+2\mu+(\lambda+2l)I_1+(3\lambda+8\mu+4m)E^i_1) \\ &\approx \lambda+2\mu+(2l+\lambda)E^i+(4m+4\lambda+10\mu)E^i_1\end{aligned} \tag{A.25}$$

Where $E^i = E^i_1 + E^i_2 + E^i_3$

For more details and the expression for velocities in more directions, please following the work by Takahashi and Motegi (2015).

APPENDIX B. THE ORTHOGONAL EXPERIMENT TABLE L_3^{27} USED FOR THE DATA ANALYSIS

The L_3^{27} table is used for the data analysis.

Table B.1: Orthogonal Experiment Table of L_3^{27}

	F	D	F*D_1	F*D_2	α	L	Error	8	9	10	11	12	13
Num	**1**	**2**	**3**	**4**	**5**	**6**	**7**	**8**	**9**	**10**	**11**	**12**	**13**
1	1	1	1	1	1	1	1	1	1	1	1	1	1
2	1	1	1	1	2	2	2	2	2	2	2	2	2
3	1	1	1	1	3	3	3	3	3	3	3	3	3
4	1	2	2	2	1	1	1	2	2	2	3	3	3
5	1	2	2	2	2	2	2	3	3	3	1	1	1
6	1	2	2	2	3	3	3	1	1	1	2	2	2
7	1	3	3	3	1	1	1	3	3	3	2	2	2
8	1	3	3	3	2	2	2	1	1	1	3	3	3
9	1	3	3	3	3	3	3	2	2	2	1	1	1
10	2	1	2	3	1	2	3	1	2	3	1	2	3
11	2	1	2	3	2	3	1	2	3	1	2	3	1
12	2	1	2	3	3	1	2	3	1	2	3	1	2
13	2	2	3	1	1	2	3	2	3	1	3	1	1
14	2	2	3	1	2	3	1	3	1	2	1	2	2
15	2	2	3	1	3	1	2	1	2	3	2	3	3
16	2	2	2	2	1	1	1	2	2	2	3	3	3
17	2	3	1	2	2	3	1	1	2	3	3	1	3
18	2	3	1	2	3	1	2	2	3	1	1	2	1
19	3	1	3	2	1	3	2	1	3	2	1	3	1
20	3	1	3	2	2	1	3	2	1	3	2	1	2
21	3	1	3	2	3	2	1	3	2	1	3	2	3
22	3	2	1	3	1	3	2	2	1	3	3	2	2
23	3	2	1	3	2	1	3	3	2	1	1	3	3
24	3	2	1	3	3	2	1	1	3	2	2	1	1
25	3	3	2	1	1	3	2	3	2	1	2	3	1
26	3	3	2	1	2	1	3	1	3	2	3	2	2
27	3	3	2	1	3	2	1	2	1	3	1	3	3

APPENDIX C. WAVES PROPAGATING IN ISOTROPIC AND ANISOTROPIC PLATES

C.1 Waves propagate in isotropic plates

The governing wave equations can govern different kinds of waves for different shape samples with different boundary conditions. For Lamb waves it can be generated in a plate shape samples with two free boundaries, it is also called Rayleigh-Lamb waves. One useful method used for solving Lamb wave governing equations is the partial wave technique (Rose 2004), the advantage of the partial wave technique is that it can solve the governing wave equation straightly with obviously physical feature.

A schematic for plates is shown in Fig. C.1. Considering an infinite plate with thickness d, its normal vectors aligned with the x_3 axis. Supposing the solution of the plate wave in the form:

$$u_j = U_j e^{i\xi(x_1+\alpha x_3-ct)} \tag{C.1}$$

Where $\vec{u}$ is the displacement vector and $\vec{U}$ is the amplitude of displacement; ξ is the wave-number along x_1 direction; $\xi\alpha$ stands for the wave-number along x_3 direction; c is the velocity along x_1 direction.

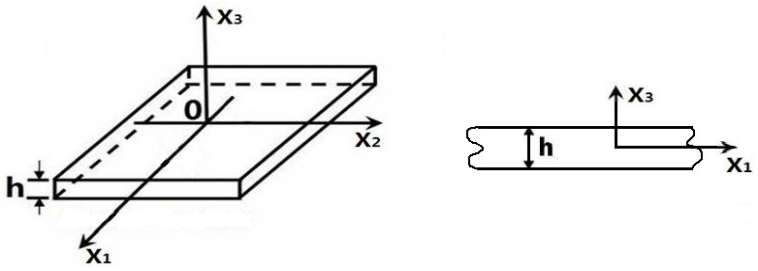

Figure C.1: Schematic showing coordinates for plates.

Substituting the solution form of Eq. C.1 to Eq. 4.4, yields:

$$\begin{bmatrix} -\lambda-(2+\alpha^2)\mu+c^2\rho & 0 & -\alpha(\lambda+\mu) \\ 0 & -(1+\alpha^2)\mu+c^2\rho & 0 \\ -\alpha(\lambda+\mu) & 0 & -\mu-\alpha^2(\lambda+2\mu)+c^2\rho \end{bmatrix} \begin{bmatrix} U_1 \\ U_2 \\ U_3 \end{bmatrix} = 0 \tag{C.2}$$

The above Eq. C.2 shows the amplitude displacement in different directions, the displacement in the x_2 direction, which stands for the shear horizontal (SH) wave, is independent from that in the x_1 and x_3 direction which stand for the mix of the shear vertical (SV) wave and the longitudinal (L) wave.

In order to get non-zero displacement amplitude, the determinant of the matrix on the left in Eq. C.2 should go to zero. Then the following two equations can obtained, for the SH waves:

$$(1+\alpha^2)\mu - c^2\rho = 0 \tag{C.3}$$

For mixed SV and L waves:

$$((1+\alpha^2)\mu - c^2\rho)((1+\alpha^2)(\lambda+2\mu) - c^2\rho) = 0 \tag{C.4}$$

For the SH wave, Eq. C.3 with the order of two, it should have two possible solutions (α_1 and α_2) while for the mixed SV and L waves, Eq. C.4, it has four possible solutions ($\alpha_3,\ \alpha_4,\ \alpha_5,\ \alpha_6$).

Based on the strain-displacement relation and the constitutive equation, the displacement and stress in different directions can be expressed as (Gandhi, 2010):

For SH waves:

$$\begin{aligned} \{u_1, u_2, u_3\} &= \sum_{q=1}^{2} \{0,1,0\} U_{2q} e^{i\xi(x_1+\alpha_q x_3 - ct)}, \\ \{\sigma_{13}, \sigma_{23}, \sigma_{33}\} &= \sum_{q=1}^{2} i\xi \{0, \mu\alpha_q, 0\} U_{2q} e^{i\xi(x_1+\alpha_q x_3 - ct)} \end{aligned} \tag{C.5}$$

and for SV and L waves:

$$\begin{aligned} \{u_1, u_2, u_3\} &= \sum_{q=3}^{6} \{1,0,R(\alpha_q)\} U_{1q} e^{i\xi(x_1+\alpha_q x_3 - ct)}, \\ \{\sigma_{13}, \sigma_{23}, \sigma_{33}\} &= \sum_{q=3}^{6} i\xi \{D_{1q}, D_{2q}, D_{3q}\} U_{1q} e^{i\xi(x_1+\alpha_q x_3 - ct)} \end{aligned} \tag{C.6}$$

Where

$$\{D_{1q}, D_{2q}, D_{3q}\} = \{\mu(R(\alpha_q) + \alpha_q), 0, \lambda + (\lambda + 2\mu)R(\alpha_q)\alpha_q\};$$
$$R(\alpha_q) = -\frac{\lambda + (2 + \alpha_q^2)\mu - c^2\rho}{\alpha_q(\lambda + \mu)} \tag{C.7}$$

Applying free boundary conditions $\sigma_{13} = \sigma_{23} = \sigma_{33} = 0$ to the expression of $\sigma_{13},\ \sigma_{23},\ \sigma_{33}$ at the boundaries $x_3 = \pm\frac{d}{2}$, for SH waves:

$$\begin{bmatrix} e^{\frac{1}{2}id\xi\alpha_1}\mu\alpha_1 & e^{\frac{1}{2}id\xi\alpha_2}\mu\alpha_2 \\ e^{-\frac{1}{2}id\xi\alpha_1}\mu\alpha_1 & e^{-\frac{1}{2}id\xi\alpha_2}\mu\alpha_2 \end{bmatrix} \begin{bmatrix} U_{21} \\ U_{22} \end{bmatrix} = 0 \tag{C.8}$$

and for SV and L waves:

$$\begin{bmatrix} D_{13}E_3 & D_{14}E_4 & D_{15}E_5 & D_{16}E_6 \\ D_{33}E_3 & D_{34}E_4 & D_{35}E_5 & D_{36}E_6 \\ D_{13}\tilde{E_3} & D_{14}\tilde{E_4} & D_{15}\tilde{E_5} & D_{16}\tilde{E_6} \\ D_{33}\tilde{E_3} & D_{34}\tilde{E_4} & D_{35}\tilde{E_5} & D_{36}\tilde{E_6} \end{bmatrix} \begin{bmatrix} U_{13} \\ U_{14} \\ U_{15} \\ U_{16} \end{bmatrix} = 0 \tag{C.9}$$

Where $E_q = e^{i\xi\alpha_q d/2}$ and $\tilde{E_q} = e^{-i\xi\alpha_q d/2}$.

For non-zero solution of the displacement amplitude, the determinants of Eq. C.8 and Eq. C.9 should go to zero, which can lead to the dispersion relationship for SH waves, and mixed SV and L waves.

For SH waves:

$$sin(d\xi\alpha_3) = 0 \tag{C.10}$$

and for SV and L waves:

$$\frac{tan(qh)}{tan(ph)} = -[\frac{4k^2pq}{(q^2 - k^2)^2}]^{\pm} \tag{C.11}$$

Where"+" refers to symmetric modes and "-" refers to anti-symmetric modes.

C.2 Waves propagate in anisotropic plates

This section is followed by the work done by Nayfeh and Chimenti (1989). Considering an infinite triclinic symmetry anisotropic plate with thickness h, where normal axis is coincident with the $x_3^{'}$-axis

of a reference Cartesian system $x_i^{'} = (x_1^{'}, x_2^{'}, x_3^{'})$. The mid-plane of the plate is chosen to accordant with the $x_1^{'}$-$x_2^{'}$ axis. For plane waves propagating in a direction that make an arbitrary angle ϕ with the $x_1^{'}$ axis, these waves can be calculated in a transformed coordinate system x_i by rotating the reference axes $x_1^{'}, x_2^{'}$ about the $x_3^{'}$ through the angle ϕ, as is shown in Fig. C.2.

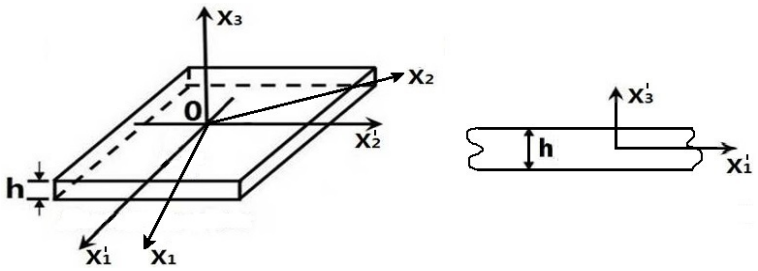

Figure C.2: Schematic showing coordinates for anisotropic plates.

Considering the case of waves in the transformed system, the general solution for the waves in anisotropic plates can be written as (same as the wave in isotropic plates):

$$u_j = U_j e^{i\xi(x_1 + \alpha x_3 - ct)} \tag{C.12}$$

Substituting the Eq. C.12 to the Christoffel Eq. 4.15:

$$(\lambda_{mn}(\alpha) - \delta_{mn})U_n = 0 \tag{C.13}$$

For λ_{11} it can be written as :

$$\begin{aligned} \lambda_{11} = {} & C_{1111}n_1n_1 + C_{1211}n_2n_1 + C_{1311}n_3n_1 \\ & + C_{1121}n_1n_2 + C_{1221}n_2n_2 + C_{1321}n_3n_2 \\ & + C_{1131}n_1n_3 + C_{1231}n_2n_3 + C_{1331}n_3n_3 \end{aligned} \tag{C.14}$$

Using the standard contracted subscript notations for C_{ikjl}, it can be written as C_{nm}: when $i = k$, then $n = i$; when $j = l$, then $m = j$; on the other side, when $i \neq k$, then $n = 9 - (i + k)$; when $j \neq l$, then $m = 9 - (j + l)$. n_1, n_2 and n_3 stand for normal cosine of the wave front. Following the above rule, the Eq. C.14 can be written as:

$$\lambda_{11} = C_{11} + 2C_{15}\alpha + C_{55}\alpha^2 \tag{C.15}$$

Supposing $K_{mn}(\alpha) = \lambda_{mn}(\alpha) - \delta_{mn}$, the elements of the matrix **K** are shown in the following form:

$$\begin{aligned}
K_{11} &= C_{11} + 2C_{15}\alpha + C_{55}\alpha^2 - \rho c^2, \\
K_{12} &= C_{16} + (C_{14} + C_{56})\alpha + C_{45}\alpha^2, \\
K_{13} &= C_{15} + (C_{13} + C_{55})\alpha + C_{35}\alpha^2, \\
K_{22} &= C_{66} + 2C_{46}\alpha + C_{44}\alpha^2 - \rho c^2, \\
K_{23} &= C_{56} + (C_{36} + C_{45})\alpha + C_{34}\alpha^2, \\
K_{33} &= C_{55} + 2C_{35}\alpha + C_{33}\alpha^2 - \rho c^2,
\end{aligned} \tag{C.16}$$

For the existance of non-trivial solutions, the determinant of **K** must go to zero. This produces a 6^{th} order equation with six possible solutions α_q, $q = 1, 2, 3, 4, 5, 6$. Different α refers to different guided wave velocity.

Also based on the strain-displacement relation and the constitutive equation, the displace and stress can be expressed as:

$$\begin{aligned}
\{u_1, u_2, u_3\} &= \sum_{q=1}^{6} \{1, V(\alpha_q), W(\alpha_q)\} U_{1q} e^{i\xi(x_1 + \alpha_q x_3 - ct)}, \\
\{\sigma_{33}, \sigma_{23}, \sigma_{13}\} &= \sum_{q=1}^{6} i\xi \{D_{1q}, D_{2q}, D_{3q}\} U_{1q} e^{i\xi(x_1 + \alpha_q x_3 - ct)}
\end{aligned} \tag{C.17}$$

Where

$$\begin{aligned}
V_q(\alpha_q) &= \frac{K_{11}(\alpha_q)K_{23}(\alpha_q) - K_{13}(\alpha_q)K_{12}(\alpha_q)}{K_{13}(\alpha_q)K_{22}(\alpha_q) - K_{12}(\alpha_q)K_{23}(\alpha_q)} \\
W_q(\alpha_q) &= \frac{K_{11}(\alpha_q)K_{23}(\alpha_q) - K_{13}(\alpha_q)K_{12}(\alpha_q)}{K_{33}(\alpha_q)K_{23}(\alpha_q) - K_{13}(\alpha_q)K_{23}(\alpha_q)}
\end{aligned} \tag{C.18}$$

and

$$
\begin{aligned}
D_{1q} &= [C_{13} + \alpha C_{35} + (C_{36} + \alpha_q C_{34})V_q + (C_{35} + \alpha C_{33})W_q] \\
D_{2q} &= [C_{15} + \alpha C_{55} + (C_{56} + \alpha_q C_{45})V_q + (C_{55} + \alpha C_{35})W_q] \\
D_{3q} &= [C_{14} + \alpha C_{45} + (C_{46} + \alpha_q C_{44})V_q + (C_{45} + \alpha C_{34})W_q]
\end{aligned} \tag{C.19}
$$

Then applying free boundary conditions $\sigma_{13} = \sigma_{23} = \sigma_{33} = 0$ to the expression of $\sigma_{13},\ \sigma_{23},\ \sigma_{33}$ at the boundaries $x_3 = \pm\frac{d}{2}$, which can result in six equations about displacement amplitudes U_{11}, U_{12}, $\cdots$, U_{16}. For the exist of nontrivial solutions, the determination of coefficients should go to zero:

$$
\begin{bmatrix}
D_{11}E_1 & D_{12}E_2 & D_{13}E_3 & D_{14}E_4 & D_{15}E_5 & D_{16}E_6 \\
D_{21}E_1 & D_{22}E_2 & D_{23}E_3 & D_{24}E_4 & D_{25}E_5 & D_{26}E_6 \\
D_{31}E_1 & D_{32}E_2 & D_{33}E_3 & D_{34}E_4 & D_{35}E_5 & D_{36}E_6 \\
D_{11}\tilde{E}_1 & D_{12}\tilde{E}_2 & D_{13}\tilde{E}_3 & D_{14}\tilde{E}_4 & D_{15}\tilde{E}_5 & D_{16}\tilde{E}_6 \\
D_{21}\tilde{E}_1 & D_{22}\tilde{E}_2 & D_{23}\tilde{E}_3 & D_{24}\tilde{E}_4 & D_{25}\tilde{E}_5 & D_{26}\tilde{E}_6 \\
D_{31}\tilde{E}_1 & D_{32}\tilde{E}_2 & D_{33}\tilde{E}_3 & D_{34}\tilde{E}_4 & D_{35}\tilde{E}_5 & D_{36}\tilde{E}_6
\end{bmatrix} = 0 \tag{C.20}
$$

Where $E_q = e^{i\xi\alpha_q d/2}$ and $\tilde{E}_q = e^{-i\xi\alpha_q d/2}$.

Solving Eq. C.20 will generate the dispersion relationship for waves in anisotropic plates.